FACULDADE DE ENGENHARIA DA UNIVERSIDADE DO PORTO

Advanced Image Analysis for the Assessment of Retinal Vascular Changes

Behdad Dashtbozorg

Doctoral Program in Electrical and Computer Engineering

Supervisor: Prof. Ana Maria Mendonça

Co-supervisor: Prof. Aurélio Campilho

May 2015

This work was supported by FEDER funds through the Programa Operacional Factores de Competitividade-COMPETE and by Portuguese funds through FCT-Fundação para a Ciência e a Tecnologia in the framework of the projects PEst-C/SAU/LA0002/2011, PEst-C/SAU/LA0002/2013 and the research grant SFRH/BD/73376/2010.

Advanced Image Analysis for the Assessment of Retinal Vascular Changes

Behdad Dashtbozorg

Doctoral Program in Electrical and Computer Engineering

To my loving wife Bahareh

Abstract

In the last decade, one of the major advances in retinal vascular imaging research has been the clear demonstration that physiological and pathological alterations in the retinal vascular network are associated with a variety of worldwide major diseases such as diabetes, hypertension and atherosclerosis. However, the clinical assessment of the retinal vascular condition is most of the times tiresome, and prone to errors, particularly if occurs in a screening environment.

Recent advances in image analysis can avoid this workload and provide the ophthalmologist with objective and reproducible results useful in daily clinical practice. The retinal image analysis systems have therefore become a prominent and powerful diagnostic tools in the field of ophthalmology by detecting the changes in retinal images.

It has been widely demonstrated that in diabetic retinopathy, the blood vessels often show abnormalities at early stages, as well as vessel diameter alterations. Changes in retinal blood vessels, such as significant dilatation and elongation of main arteries, veins, and their branches, are also frequently associated with hypertension and other cardiovascular pathologies. Among several characteristic signs associated with vascular changes, the Central Retinal Arteriolar Equivalent (CRAE), the Central Retinal Venular Equivalent (CRVE) and the Arteriolar-to-Venular Ratio (AVR) have been frequently used as indicators for the early detection, diagnosis, staging and follow-up of diabetes and hypertension, since they can reflect the narrowing or dilation of the retinal blood vessels.

The main goal of this work is the development of an automatic system for the measurement of CRAE, CRVE, AVR and several bifurcation geometrical features. Among other image processing operations, the estimation of these features requires vessel segmentation, vessel caliber measurement, artery/vein (A/V) classification and optic disc (OD) segmentation.

The CRAE, CRVE and AVR values are calculated from the calibers of the vessels inside a specific region of interest (ROI), defined as the standard ring area around the OD. As a consequence, both the localization of the optic disc center (ODC) and its diameter are required for automating the AVR calculation. For this reason, a fully automatic method based on sliding band filter is proposed; this method is able to produce useful results even in the presence of severe pathological conditions and showing a great independence from image acquisition settings.

In this work, a graph-based method is proposed for the classification of retinal vessels as arteries or veins using a combination of structural information taken from the vasculature graph with intensity features from the original color image. Supervised and unsupervised techniques are introduced for the final assignment of A/V classes; the supervised approach uses linear discriminant analysis and a set of intensity features, while the unsupervised approach assigns the A/V classes using a *k*-means clustering algorithm and red intensity of vessel pixels.

Finally, the developed approaches are integrated in RetinaCAD, Retinal Computer Aided Diagnosis system which includes vessel segmentation, vessel width estimation, optic disc segmentation and A/V classification. This system is designed to facilitate the application of retinal image analysis tools and the automated estimation of some indexes, in particular CRAE, CRVE, AVR and bifurcation geometrical features with high potential for clinical applications.

Resumo

Na última década, um dos maiores avanços na investigação em imagens vasculares da retina foi a clara demonstração de que alterações fisiológicas e patológicas na rede vascular estão relacionadas com uma variedade de doenças prevalentes em todo o mundo tais como diabetes, hipertensão e aterosclerose. Contudo, a avaliação clínica da condição vascular retiniana é na maioria das vezes uma tarefa cansativa e suscetível à ocorrência de erros, particularmente se a avaliação for feita num ambiente de rastreio.

Avanços recentes em Análise de Imagem permitem evitar esta sobrecarga de trabalho e fornecerao oftalmologista resultados objetivos e reprodutíveis que são úteis na prática clínica diária. Os sistemas de análise de imagens da retina tornaram-se assim ferramentas de diagnóstico importantes para a deteção de alterações em imagens da retina.

Na retinopatia diabética tem sido amplamente demonstrado que os vasos sanguíneos podem apresentar alterações em fases precoces, nomeadamente alterações no seu diâmetro. Alterações nos vasos sanguíneos da retina, tais como a dilatação significativa e o alongamento das principais artérias, veias e seus ramos, são também frequentemente associadas à hipertensão e outras patologias cardiovasculares. Entre vários sinais característicos associados a alterações vasculares, o Diâmatro Arterial Equivalente (CRAE), o Diâmetro Venoso Equivalente (CRVE) e o Índice Arterio-Venoso (AVR) têm sido frequentemente utilizados como indicadores para a detecção precoce, diagnóstico, avaliação do estado e seguimento de diabetes e hipertensão, uma vez que os seus valores podem refletir o estreitamento ou dilatação dos vasos sanguíneos da retina.

O objetivo principal deste trabalho é o desenvolvimento de um sistema automático para a medição do CRAE, CRVE, AVR e várias características geométricas das bifurcações vasculares. Entre outras operações de processamento de imagem, a estimação destas características requer a segmentação e medição do calibre dos vasos sanguíneos, classificação dos vasos em artérias ou veias e segmentação do disco óptico.

Os valores de CRAE, CRVE e AVR são calculados a partir dos calibres dos vasos dentro de uma região de interesse específica, definida como a área anelar padrão em volta do disco óptico. Como consequência, tanto a localização do centro do disco óptico como o seu diâmetro são necessários para automatizar o cálculo de AVR. Por este motivo, é proposto um método completamente automático baseado num filtro de convergência que tem como região de suporte uma banda deslizante; este método é capaz de obter resultados úteis, mesmo na presença de condições patológicas graves e mostra uma grande independência das configurações de aquisição de imagem.

Neste trabalho, é proposto um método de classificação dos vasos da retina como artérias ou veias que representa a rede vascular usando um grafo e combina esta informação estrutural com características de intensidade da imagem de cor original. Técnicas supervisionadas e não supervisionadas são usadas para a atribuição final das classes artéria/veia; a abordagem supervisionada utiliza análise discriminante linear e um conjunto de características de intensidade, enquanto que a abordagem não supervisionada atribui as classes artéria/veia utilizando um algoritmo de agrupamento de k-médias e a intensidade dos pixels dos vasos no canal vermelho (R) da imagem colorida (RGB).

Finalmente, as abordagens desenvolvidas estão integradas no sistema RetinaCAD, *Retinal Computer Aided Diagnosis*. Este sistema é projetado para facilitar a aplicação de ferramentas de análise de imagens da retina tendo alto potencial para aplicações clínicas.

Acknowledgments

The work presented in this thesis was accomplished between 2010 and 2014. This period of time was thoroughly different form the rest of my life both personally and professionally. I am writing these lines to express my gratitude to those whose support was undeniably holding my back to resist the hard challenging path throughout the last four years.

First of all, I would like to thank Professor Ana Maria Mendonça and Professor Aurélio Campilho, my supervisors, who helped me to start my career form the very beginning and provided me a great scientific supervision during the whole period. Their interesting ideas always encouraged me to keep looking for solutions and whenever I felt down their efforts to keep me motivated were truly effective. Their deep knowledge in biomedical image analysis has been shedding light on the dark parts of the path.

I would also like to thank Dr. Susana Penas form Centro Hospitalar São João and Professor Jorge Polónia from Faculdade de Medicina, Universidade do Porto for making the clinical data available for this work.

The financial support from the FCT-Fundação para a Ciência e a Tecnologia, Portugal with the grant Ref. SFRH /BD/73376/2010 is also greatly acknowledged.

I was lucky to enter to a very strong research group at Instituto de Engenharia Biomédica (INEB). I had very constructive discussions with my colleagues and they were kindly helpful to me to resolve the issues I confronted during the accomplishment of my work.

During my stay at Porto, my friends' company helped me not to be emotionally affected by being so far from homeland. I would like to thank them all for their friendship, especially Ali, Mohammad and Mohsen who have been there for me through thick and thin.

Last, but not least, I express my deepest thanks to my parents and my brother for their unconditional support through the last years in so many ways. I cannot thank enough my wife for her love and support, without which I would never have completed this work.

"The soul, fortunately, has an interpreter - often an unconscious,

but still a truthful interpreter - in the eye."

Charlotte Bronte

Contents

List of Figures

List of Tables

Abbreviations and Symbols

A/V	Artery/Vein
ACC	Accuracy
AUC	Area Under Curve
AVR	Arteriolar-to-Venular Ratio
BP	Blood Pressure
CAD	Computer-Aided Diagnosis
CRAE	Central Retinal Artery Equivalent
CRVE	Central Retinal Venular Equivalent
DC	Dice's coefficient
DR	Diabetic Retinopathy
FOV	Field of View
FPF	False Positive Fraction
LDA	Linear Discriminant Analysis
MAD	Mean Absolute Distance
MCC	Matthews Correlation Coefficient
ME	Macular Edema
OD	Optic Disc
ODC	Optic Disc Center
RetinaCAD	Retinal Computer-Aided Diagnosis
ROI	Region of Interest
ROC	Receiver Operating Characteristic
SBF	Sliding Band Filter
TPF	True Positive Fraction

Chapter 1

Introduction

The retina is the only part of the human body where the blood circulation can be observed directly. Several systemic diseases can affect the retinal blood vessels, which makes the retinal image analysis a potential diagnostic tool, as it allows assessing vascular changes in an easy and non-invasive way. Retinal image analysis is one of the active research areas with the goal of providing computer-aided methods to help the quantification, measurement and visualization of retinal landmarks and biomarkers.

In diabetic retinopathy (DR), the blood vessels often show abnormalities at early stages [1], as well as vessel diameter alterations [2]. Changes in retinal blood vessels, such as significant dilatation and elongation of main arteries, veins, and their branches [2, 3], are also frequently associated with hypertension and other cardiovascular pathologies.

The greatest emphasis in automated diagnosis has been given to the detection of diabetic retinopathy. Diabetes is reaching epidemic proportions worldwide, due to the growth of population, urbanization and increasing adult obesity prevalence and physical inactivity. The recent report by the International Diabetes federation (IDF) [4] indicates that 8.3% of adults (387 million people) have diabetes, and the number of people with the disease is set to rise beyond 592 million by 2035. Yet, with 175 million of cases currently undiagnosed, a vast amount of people with diabetes are progressing towards complications unawares. People with diabetes have an increased risk of developing a number of serious health problems. Consistently high blood glucose levels can lead to serious diseases affecting the heart, the blood vessels, eyes, kidneys and nerves. In addition, people with diabetes also have a higher risk of developing infections, which can cause blindness, kidney failure, lower limb amputation, stroke and sudden death. In 2014 diabetes was the direct cause of 4.9 million deaths.

Diabetic retinopathy is divided into various stages based on severity. The early signs like microaneurysms, hemorrhages and cotton wool spots are known as non-proliferative diabetic retinopathy [1]. Proliferative diabetic retinopathy develops from occluded capillaries that lead to retinal ischemia and formation of new vessels on the surface of the retina near the optic disc (OD). Certain lesions, such as the number of microaneurysms and dot hemorrhages correlate with severity and progression of the diseases [5]. Retinal vessel dilatation is a well-known phenomenon in diabetes and significant dilatation and elongation of arterioles, venules, and their macular branches occur in the development of diabetic macular edema that can be linked to hydrostatic pressure changes [6].

The World Health Organization (WHO) [7] rates hypertension as one of the most important causes of premature death worldwide and the problem is growing. There are at least 970 million people worldwide who have elevated blood pressure (hypertension) and in 2025 it is estimated there will be 1.56 billion adults living with high blood pressure. Hypertension is a major risk factor for coronary heart disease and ischemic as well as hemorrhagic stroke. Blood pressure levels have shown to be positively and continuously related to the risk for stroke and coronary heart disease. High blood pressure is called the “silent killer" since it often has no warning signs or symptoms, and many people do not realize they have it. Hypertension can cause changes to the retina, such as localized or generalized narrowing of vessels, copper wiring and silver wiring, arteriovenous nicking, hemorrhages, nerve fiber layer losses, increased vascular tortuosity, cotton wool spots and exudates [1].

For both diseases, the early diagnosis of diabetes and hypertension are crucial to prevent and reduce the pathological damages, which can be achieved through the use of retinal image analysis. Detection of lesions or vessel changes and measurement of useful objective and reproducible health indicators can improve the capability of early diagnosis.

1.1 Motivation

Current techniques for the assessment of vascular changes in retinal images are mostly semi-automated or manual which require trained experts to help the process by searching large numbers of retinal images. The application of digital imaging to ophthalmology has now provided the possibility of automated analysis of retinal images to assist clinical diagnosis and treatment.

Automated retinal image analysis has huge potential benefits. It offers the capability to examine a large number of images with time and cost savings and offers more objective measurements

than current observation techniques. Advantages in a clinical context include the potential to perform automated screening for conditions such as diabetic retinopathy, and hence to reduce the workload required from manual trained graders.

However, even in healthy retinal images, the automatic detection of retinal landmarks and features requires varied and innovative image processing, image analysis and machine learning techniques. In retinal images with pathology, there is wider field of patterns and features to target, and it is also a challenging task to develop robust and reliable algorithms in the presence of pathological conditions. Researchers and experts in pattern recognition and image analysis find retinal images exciting, challenging, and rewarding to work with. There are quite a number of problems in automated retinal analysis that need to be solved before the computer-aided diagnosis systems can be used for general clinical applications.

This work is mostly focused on the development of retinal image analysis techniques for the automatic assessment of vascular changes caused by systemic diseases. Within this context, some of the challenges are being able to accurately segment the vessels, measure the vessel caliber, extract the OD boundary and classify the blood vessels as arteries or veins. The location and radius of OD and the artery/vein (A/V) classification are required as prerequisite stages for calculating important vascular signs, which can provide clinically valuable information to aid prevention and management of diseases namely diabetes and hypertension.

1.2 Contributions

The aims of the work presented in this thesis are the development of algorithms and tools for the retinal image analysis allowing an automatic and reproducible assessment of retinal vascular changes. The starting point of this work is based on a vessel segmentation method previously developed by our research group [8]. The main contributions of this thesis can be summarized as follows:

• A fully automatic method which segments the optic disc independently of image characteristics such as size, quality and camera field of view. It was demonstrated that this approach is robust to variations of contrast and illumination, and also that it is quite insensitive to the presence of pathological conditions that can disturb the segmentation of the OD, such as the presence of exudates and peripapillary atrophy. The results of the proposed method are compared with manually extracted boundaries from three public databases. These results demonstrate that the proposed solution outperforms recent approaches for OD segmentation [9].

• A fully automatic method which classifies the vessels as arteries or veins based on a graph extracted from a vascular tree. This method is able to classify the whole vascular tree and does not restrict the classification to specific regions of interest. While most of the recent methods mainly use intensity features for discriminating between arteries and veins, the proposed method uses additional information extracted from a graph which represents the vascular network. The promising results of the proposed graph-based A/V classification method on the images of three different datasets demonstrate the independence of this method with various properties, such as differences in size, quality, and camera field of view [10].

• Automatic approaches for calculating the Central Retinal Artery Equivalent (CRAE), Central Retinal Venular Equivalent (CRVE) and Arteriolar-to-Venular Ratio (AVR) in retinal images which are supported by a new approach for optic disc segmentation and by new supervised and unsupervised techniques for A/V classification. These methods are evaluated on a public dataset, where the mean error of the measured AVR values with respect to the reference was identical to the one achieved by a medical expert using a semi-automated system, thus demonstrating the reliability of the proposed methods for AVR estimation [11, 12].

• RetinaCAD, a user-friendly retinal computer-aided diagnosis system, that is able to automatically detect, measure and classify two main retinal landmarks, the optic disc and the vessels. RetinaCAD can measure several vascular features that are recognized as indicators for some prevalent systemic diseases, namely CRAE, CRVE and AVR, as well as various geometrical features associated with vessel bifurcations. This application was assessed in the images of a new dataset from a local hospital, where it showed an association between AVR values and clinical information. The lower AVR values in the subjects with pathological conditions in contrast to the non-pathological ones demonstrates the potential of the system as a CAD tool for early detection and follow-up of diabetes, hypertension or cardiovascular pathologies [13].

• Publications in peer-reviewed journals and presentations in the different conferences. The list of related publications are included in Appendix B. RetinaCAD has been awarded in RecPad 2014, 20th edition of the Portuguese Conference on Pattern Recognition with the Best Poster Award and also has been selected as one of 10 finalists in iUP25k - University of Porto Business Ideas Competition.

1.3 Organizational Overview

Together with this chapter, the research reported in this Ph.D. thesis is organized in the following chapters.

Chapter 2 provides a general literature review on retinal image analysis methods useful for the assessment of vascular changes, namely vessel segmentation, optic disc detection, A/V classification and assessment of vascular changes.

Chapter 3 introduces an automatic approach for optic disc segmentation using a multiresolution sliding band filter (SBF).

Chapter 4 presents an automatic artery/vein classification method based on the analysis of a graph extracted from the retinal vasculature. Final classification of a vessel segment as A/V is performed by means of supervised and unsupervised approaches.

Chapter 5 is devoted to the presentation of approaches for the automated assessment of vascular changes, particularly the measurement of CRAE, CRVE and AVR indexes.

Chapter 6 presents RetinaCAD (Retinal Computer-aided Diagnosis System) and shows the results of the proposed system evaluation as well as the clinical validation.

Finally, Chapter 7 concludes this thesis by providing a summary of the presented research contributions and future directions.

Chapter 2

Retinal Image Analysis for the Assessment of Vascular Changes. Overview

Retina is a light-sensitive tissue lining the inner surface of the eye (Figure 2.1(a)). When an ophthalmologist uses an ophthalmoscope to look into the eye he sees a retinal image like the one in Figure 2.1(b). In the center of the retina is the optic disc which is the beginning of the optic nerve and the entry point for the major blood vessels that supply the retina. Fovea can be seen in Figure 2.1(b) as the blood vessel-free reddish spot, in the center of the area known as the macula. The blood vessels of the retina radiate from the center of the optic disc. The walls of the retinal blood vessels are transparent and therefore the column of blood flowing in these vessels can be directly observed. The arteries appear lighter and narrower when compared to the veins. Retina is the only part of blood circulation system that can be observed directly, so any vascular changes or abnormality can be detected and can be used for screening.

Some of the pathologies that affect the retina are age-related macular degeneration, glaucoma, retinopathy of prematurity, diabetic retinopathy and hypertension [14]. Some of these diseases are now amenable to automated identification and assessment. In addition, retinal blood vessel pattern can also provide information on the presence or risk of developing hypertension, diabetes, cardiovascular or cerebrovascular diseases [14].

The retinal vasculature can be observed directly and it is easily accessible to study the health of the human microcirculation in vivo. Pathological changes of the retinal vasculature, such as the appearance of microaneurysms, focal areas of arteriolar narrowing, arteriovenous nicking, and

retinal hemorrhages are common fundus findings in older people, even in those without hypertension or diabetes. Recent advances in retinal image analysis have allowed reliable and precise assessment of these retinal vascular changes, as well as objective measurement of other topographic vascular characteristics such as retinal vascular widths, geometrical attributes at vessel bifurcations and vessel tracking.

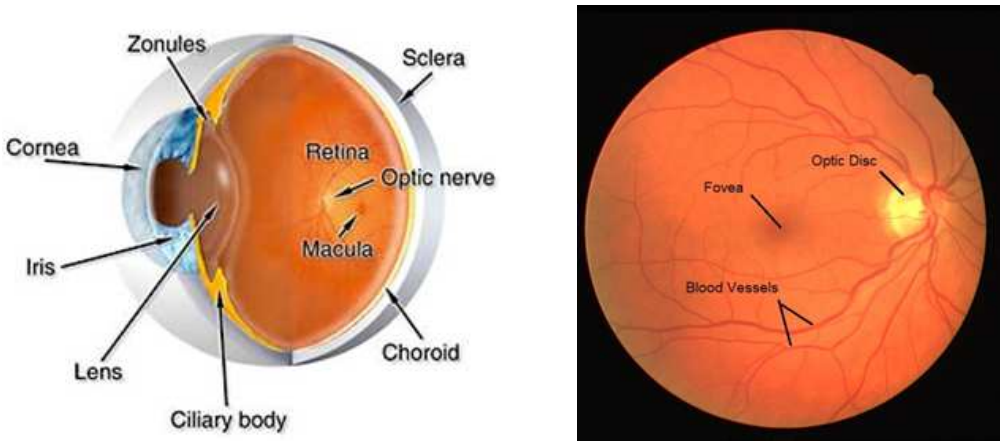

(a) (b)

Figure 2.1: The retina (a) Eye anatomy; (b) Retinal image.

In this chapter, the principles of retinal digital image analysis and the techniques for extracting the signs related to the retinal vascular changes are discussed. The methods for detecting and classifying the main retinal landmarks are critical components of circulatory blood vessel analysis systems, so it would be valuable to start with reviewing the methods for retinal vessel segmentation, optic disc segmentation and artery/vein (A/V) classification (in Sections 2.1, 2.2 and 2.3). After that the methods for extracting the signs related to the retinal vascular changes are described in Section 2.4. Finally, Section 2.5 summarizes the concluding remarks.

2.1 Vessel Segmentation

All retinal blood vessels originate from the optic disc and they have lower reflectance when compared to other retinal surfaces, so they appear darker than the background. Retinal vessel segmentation is one of the fundamental components of automatic retinal disease screening systems. Retinal blood vessel and their attributes, such as length, width, tortuosity and branching pattern and angles are useful for diagnosis, screening, treatment, and evaluation of various systemic diseases.

Most of the vessel segmentation methods utilise the contrast existing between the retinal blood vessel and surrounding background. However, there are several challenges in retinal vessel segmentation that makes it a non-trivial task. There are other structures in the image such as the retina boundary, the optic disc, and bright or dark spots (caused by pathologies) which can negatively influence the process of vessel segmentation. On the other hand, the narrow vessels have a very low contrast in comparison with the background which makes the discrimination even harder. In addition, the effect of central reflex in wider vessels makes it complex to distinguish one vessel from two side-by-side vessels.

Vessel segmentation algorithms and methods can be divided into three main categories [15,16]: image analysis approaches, tracking-based approaches and classification-based approaches.

2.1.1 Image Analysis Approaches

Image analysis approaches extract meaningful information from images and use that information for segmenting the vessels. These image analysis approaches can be organized into four categories: multi-scale approaches, centerline detection methods, region growing approaches and matched filters approaches [15, 16].

Multi-scale approaches perform segmentation on different image resolutions. Thick vessels are extracted at low resolution images and then thinner structures, such as deriving branches of already segmented structures, can be segmented at higher resolution. The main advantages of this technique are the increased processing speed and the increased robustness. Qin Li *et al.* [17] proposed a vessel segmentation method which includes a multi-scale analytical scheme using Gabor filters and scales multiplication. Scale multiplication, which is defined as the product of Gabor filter responses at two adjacent scales, enhances the edges and filters noise. After that they use a threshold probing technique utilizing the features of the retinal vessel network which uses a line tracking algorithm to guide the selection of the threshold. Lathen *et al.* [18] accomplish vessel segmentation using multi-scale quadrature filtering. They combine both line and edge detection using quadrature filters across multiple scales. The filter result gives well defined vessels as linear structures, while distinct edges facilitate a robust segmentation. For quadrature filtering of 2D and 3D images, the filter kernel is applied in at least three and six uniformly distributed directions, respectively. For segmentation, the authors combine the multi-scale filtering result in a global phase map by a weighted summation, favoring scales of high strength.

Moghimirad *et al.* [19] present a multi-scale approach based on a weighted 2D medialness function. The result of the medialness function is first multiplied by the eigenvalues of the Hessian matrix in every pixel of the image in order to extract vessel's medial-lines. After that, by extracting the centerlines of vessels and estimation of radius of vessels, the retinal vessels are segmented. Li *et al.* [20] used the multi-scale production of multi-scale matched filters for vessel segmentation. The scale production is used to enhance the edges and decrease noise so that some small weak vessels with low local contrast are detected with good width estimation. Saffarzadeh *et al.* [21] proposed a vessel segmentation technique based on a multi-scale line detection. This method uses a perceptive transform based on Weber's law, and then reduces the impact of bright lesions by k-means clustering. Afterwards, a line operator is used in three scales for the vessels detection and the segmentation is finalized by thresholding to ignore some of the dark lesions.

Centerline detection approaches extract blood vessel centerline segments then create the vessel tree by connecting these centerline segments. Different approaches are used to extract the centerline structure. Mendonça *et al.* [8] proposed an algorithm which starts with the extraction of vessel centerlines by using directional information from a set of four directional Difference-of-Offset-Gaussians filters. After that, a region growing process guided by some image statistics connects the candidate points. The final segmentation is obtained using an iterative region growing that integrates the contents of several binary images resulting from vessel width dependent morphological filters. Recently, Mendonça *et al.* extended their method for segmenting high resolution images [22]. Wu *et al.* [23] describe a segmentation approach for vessel centerlines based on ridge descriptors. The proposed ridge descriptor contains the normalized largest curvature and the orientations of gradients in the local neighborhood. For vessels of a certain scale, the distribution of the descriptors is assumed to have a normal distribution estimated from a training set with known ground truth. Then vessel center line segmentation can be performed based on the distance between the ridge descriptor at candidate pixels and the learned model.

Region growing approaches select a set of seed points based on some predefined criteria. The initial region begins at the exact location of these seeds. The regions are then grown from these seed points to adjacent points depending on a region membership criterion like same intensity characteristics. Martinez-Perez *et al.* [24] presented a method based on the scale-space analysis of the first and second derivative of the intensity image which gives information about its topology and overcomes the problem of variations in contrast inherent to retinal images. The local maxima over scales of the magnitude of the gradient and the maximum principal curvature are used as

features for a region growing procedure. The growth is constrained to regions of low gradient magnitude and then the borders between regions will be defined by growing vessel and background classes without gradient restriction.

Grag *et al.* [25] described an unsupervised, curvature-based method for segmenting the complete vessel tree from color retinal images. The vessels are modelled as trenches and the medial lines of the trenches are extracted using the curvature information derived from a curvature estimate. After that, the vessel structure is extracted using a modified region growing method, where the medial points detected by the trench detection algorithm serve as seed points. The region is grown only around a selected neighborhood of the seed point, whose size is based on the width of the largest vessel.

Matched filters approaches convolve the image with multiple matched filters for extracting objects of interest, as in Sofka *et al.* [26] for extracting vessels in retinal images. The core of the technique is a new likelihood ratio test that combines matched filter responses, confidence and vessel boundary measures. Matched filter responses are derived in scale-space to extract vessels of widely varying widths. Vessel boundary measures and associated confidences are computed at potential vessel boundaries. The combination of these responses forms a six-dimensional measurement vector at each pixel. A training technique is used to develop a mapping of this vector to a likelihood ratio that measures the vesselness at each pixel. Finally, the new vesselness likelihood ratio is embedded into a vessel tracing framework for vessel centerline extraction.

The method proposed by Ramlugun *et al.* [27] segments the blood vessels using an 2-D Gabor filter on a histogram-equalized image followed by hysteresis thresholding. Fathi *et al.* [28] presents a method based on complex continuous wavelet analysis to enhance blood vessels and to remove noise. The segmented vessels are obtained by an adaptive histogram-based thresholding procedure along with proper length filtering process. Krause *et al.* [29] porposed a vessel segmentation method based on the local Radon transform for the vessel smoothing. This method first enhances the contrast of blood vessels using a second-order differential operator, and then the vessels are detected by the combination of smoothing along vessel directions with contrast enhancement across them.

2.1.2 Tracking-based Approaches

Tracking-based approaches apply local operators on sites known a priori to belong to a vessel and track it. These methods start from an initial point, detect vessel centerlines or boundaries

by analyzing the pixels orthogonal to the tracking direction. Different methods are employed for determining vessel contours or centerlines. An advantage of tracking based methods is the connectedness of vessel segments, which is not guaranteed in pixel processing based methods.

Vlachos *et al.* [30] proposed an algorithm for vessel segmentation and network extraction in retinal images. In this method, a new multi-scale line-tracking procedure starts from a small group of pixels, derived from a brightness selection rule, and terminates when a cross-sectional profile condition becomes invalid. The multi-scale image map is derived after combining the individual image maps along scales, containing the pixels confidence to belong to a vessel. The initial vessel network is derived after map quantization of the multi-scale confidence matrix. Median filtering is applied in the initial vessel network, restoring disconnected vessel lines and eliminating noisy lines. In the final step, post-processing removes erroneous areas using directional attributes of vessels and morphological reconstruction. Niemeijer *et al.* [31] proposed an automated vessel linking framework that connects together separate pieces of the retinal vasculature into a connected vascular tree. To determine which vessel sections should be linked together they use a supervised cost function.

Yin *et al.* [32] presented a probabilistic tracking method for the blood vessel detection. In the tracking process, vessel edge points are detected iteratively using local gray-level statistics and vessel continuity properties. A Gaussian-shaped curve is used for estimating the local vessel sectional intensity profiles. Local vessel structure and the edge points are obtained by means of a Bayesian method with the maximum a posteriori probability criterion. Bekkers *et al.* [33] proposed two vessel edge tracking algorithms which are based on an orientation score. These algorithms use invertible and non-invertible orientation scores by means of cake wavelets and Gabor wavelets. They also presented a fast method for vessel centerline tracking through a multi-scale set of non-invertible orientation scores where the multi-scale approach makes the algorithm less stable at crossings and bifurcation points.

2.1.3 Classification-based Approaches

Classification-based approaches aim at finding hypotheses that explain the training data and use these hypotheses for classifying each pixel as vessel or non-vessel. Niemeijer *et al.* [34] extract a simple feature vector for each pixel from the green component, and then, use a k-nearest neighbor (kNN) algorithm to estimate the probability of the pixel belong to a vessel. Another supervised method, called primitive-based method, was proposed by Staal *et al.* [35]. This algorithm is

based on the extraction of image ridges (expected to coincide with vessel centerlines) used as primitives for describing linear segments, named line elements. Each pixel is assigned to the nearest line element to form image patches, and then classified using a set of features from the corresponding line and image patch. The feature vectors are classified using a kNN classifier. The feature selection is based on sequential forward feature selection which, in each step, selects the best feature that satisfies some criterion function and includes it in the current feature set. The set that gives the best performance is chosen.

The method presented in [36] by Soares *et al.* also adopts supervised classification. Each image pixel is classified as vessel or non-vessel based on the pixel feature vector, which is composed of the pixel intensity and 2-D Gabor wavelet transform responses taken at multiple scales. A Gaussian-mixture model classifier (a Bayesian classifier in which each class-conditional probability density function is described as a linear combination of Gaussian functions) is then applied to obtain the final segmentation. Lupascu *et al.* [37] proposed a method for automated vessel segmentation in retinal images. For each pixel in the field of view of the image, a 41-D feature vector is constructed. The feature vector consists of the output of filters, vesselness, and ridgeness measures based on eigen decomposition of the Hessian computed at each image pixel, and the output of a 2-D Gabor wavelet transform taken at multiple scales. Moreover, the feature vector includes the principal curvatures, the mean curvature, and the values of principal directions of the intensity surface computed at each pixel of the green component image. The value of the root mean square gradient and the intensity within the green component at each pixel are also included in the feature vector. After that an AdaBoost classifier is trained on gold standard examples of vessel and nonvessel pixels, and then used for classifying previously unseen images.

Neural networks (NN) are used for simulating biological learning and are widely used in pattern recognition mainly for classification. One of the advantages that make neural networks attractive in medical image segmentation is their ability to use nonlinear classification boundaries obtained during the training of the network. Another attractive feature of the neural nets is the ability to learn. In this regard, Marin *et al.* [38] presented a supervised method for blood vessel detection in digital retinal images. This method in based on a feature vector with gray-level and moment invariants-based features and uses a neural network scheme for pixel classification. Two classification stages are considered: a design stage, in which the NN configuration is decided and the NN is trained, and an application stage, in which the trained NN is used to classify each pixel as vessel or non-vessel to obtain a vessel binary image. At the end the classifier performance is

enhanced by the inclusion of a two-step post processing stage: the first step fills pixel gaps in detected blood vessels, while the second step removes isolated vessel pixels.

Franklin *et al.* [39] proposed a retinal vessel segmentation technique using neural networks. In the first stage, a Gaussian filter is used to smooth the gray-scale image, then the Gabor features at different orientations and moment invariants-based features are measured. In the next phase, some samples are taken from vessel and nonvessel regions to train the NN. Afterwards each pixel of a retinal image is classified as vessel or nonvessel using a multi-layer perceptron neural network and a back propagation algorithm, which changes the weights in the feed forward network.

Perfetti *et al.* [40] exploited the geometrical properties of blood vessels by calculating the line strength of the blood vessels in the green plane of the retinal image. The line strength image was obtained with simple cellular neural network (CNN) templates in a multistep operation with virtual template expansion. The proposed CNN algorithm requires only linear space-invariant 3×3 templates, so it could be implemented using one of the existing very-large-scale integration chips.

Wang *et al.* [41] presented a hybrid approach using a convolutional neural network and ensemble random forests (RFs) for blood vessel segmentation. This method starts by a set of prepossessing steps to normalize nonuniform illumination and to enhance the vessels contrast. Then a convolutional neural network is used for extracting a set of hierarchical features including multiscale information about the geometric structure. The convolutional neural network is a supervised feature learner, which is invariant to image translation, scaling and skewing. Afterwards, ensemble RFs is trained to obtain a vessel classifier. These ensemble RFs employ multiple classifiers to obtain better performance by combining the decisions from multiple weak learners.

2.1.4 Vessel Segmentation Evaluation

Most of the retinal vessel segmentation methodologies are evaluated on two publicly available databases, the DRIVE dataset and the STARE dataset, which are introduced in Appendix A. The manual segmentation is provided by two experts for the images of these datasets.

Table 2.1 shows the performance of some of the mentioned segmentation methods. The segmentation performance can be evaluated based on accuracy (ACC), sensitivity (SN) and specificity (SP). According to equation (2.1), accuracy is measured by the ratio of the total number of correctly classified pixels (sum of true positives and true negatives) to the number of pixels in the image field of view. Sensitivity reflects the ability of the algorithm to detect the vessel pixels

based on equation (2.2). Specificity is the ability to detect non-vessel pixels using equation (2.3).

$$ACC = \frac{(TP+TN)}{(TP+TN+FP+FN)} \tag{2.1}$$

$$SN = \frac{TP}{(TP+FN)} \tag{2.2}$$

$$SP = \frac{TN}{(FP+TN)} \tag{2.3}$$

where the true positive (TP) is the number of pixels identified as vessel in both the ground truth and segmented image, and the true negative (TN) is the number of pixels classified as a non-vessel in the ground truth and the segmented image. False negative (FN) is the number of pixels classified as non-vessel in the segmented image but as a vessel pixel in the ground truth image, and the false positive (FP) is number of pixels marked as vessel in the segmented image but non-vessel in the ground truth image.

In addition, the performance of the algorithm can also be measured with the area under the receiver operating characteristic (ROC) curve. The ROC curve is a plot of the true-positive fraction versus the false-positive fraction for different cut-off points of a parameter.

During the literature review, it was observed that some papers describe the performance in terms of accuracy and area under ROC whereas the other articles choose sensitivity and specificity for reporting the performance. As it is shown in Table 2.1, the performance of classification-based algorithms is better in general than their counterparts. Almost all the supervised methods report the area under ROC of higher than 0.95 and among them Marin *et al.* [38] reported the highest. However, these methods do not work very well on the images with non-uniform illumination as they produce false detection in some images on the border of the optic disc, hemorrhages and other types of pathologies that present strong contrast. Matched filters has been extensively used for automated retinal vessel segmentation [26–29]. Many improvements and modifications are proposed since the introduction of the Gaussian matched filter. The matched filters alone cannot handle vessel segmentation in pathological retinal images; therefore it is often employed in combination with other image processing techniques. The confidence measures and edge measures defined by Sofka *et al.* [26] deals with the problem of overlapping of the non-vessel structures like the retinal boundary and the optic disk in vasculature extraction.

The overall comparison of the segmentation categories presented in this section shows that image analysis approaches, especially the multi-scale approaches are mostly faster than others.

The main advantage of tracking approaches is the connectedness of vessel segments, which is not guaranteed in other approaches. The classification-based approaches can achieve more accuracy and quality but training these methods is usually computationally more expensive.

Table 2.1: The performance of vessel segmentation methods.

Methods	Dataset	Sensitivity	Specificity	Accuracy	Area under ROC
2nd-observer	DRIVE	0.7763	0.9723	0.9473	-
	STARE	0.8951	0.9384	0.9354	-
Moghimirad *et al.* (2012) [19]	DRIVE	0.7852	0.9935	0.9659	0.958
	STARE	0.7177	0.9753	0.9484	0.9678
Li *et al.* (2012) [20]	DRIVE	0.7154	0.9716	0.9343	-
	STARE	0.7191	0.9687	0.9407	
Saffarzadeh *et al.* (2014) [21]	DRIVE	-	-	0.9387	0.9303
	STARE			0.9483	0.9431
Mendonça *et al.* (2006) [8]	DRIVE	0.7344	0.9764	0.9463	-
	STARE	0.6996	0.973	0.9479	-
Mendonça *et al.* (2014) [22]	DRIVE	0.7467	0.9762	0.9466	-
	STARE	0.7194	0.9759	0.9487	-
Martinez-Perez *et al.* (1999) [24]	DRIVE	0.7246	0.9655	0.9344	-
	STARE	0.7506	0.9569	0.941	-
Ramlugun *et al.* (2012) [27]	DRIVE	0.6413	0.9767	0.934	-
Fathi *et al.* (2013) [28]	DRIVE	0.7768	0.9759	0.9581	-
	STARE	0.8061	0.9717	0.9591	
Krause *et al.* (2013) [29]	DRIVE	-	-	0.9468	-
Vlachos *et al.* (2010) [30]	DRIVE	0.747	0.955	0.9285	-
Niemeijer *et al.* (2009) [31]	DRIVE	0.7145	-	0.9416	-
Staal *et al.* (2004) [35]	DRIVE	-	-	0.9442	0.952
	STARE			0.9516	0.9614
Soares *et al.* (2006) [36]	DRIVE	-	-	0.9466	0.9614
	STARE	-	-	0.948	0.9671
Lupascu *et al.* (2010) [37]	DRIVE	0.72	-	0.9597	0.9561
Perfetti *et al.* (2007) [40]	DRIVE	-	-	0.9563	0.9558
	STARE	-	-	0.9584	0.9602
Marin *et al.* (2011) [38]	DRIVE	-	-	0.9452	0.9588
	STARE	-	-	0.9526	0.9769
Wang *et al.* (2014) [41]	DRIVE	0.8173	0.9733	0.9767	0.9475
	STARE	0.8104	0.9791	0.9813	0.9751

2.2 Optic Disc Segmentation

Optic disc is a bright circular shape and all major blood vessels and nerves originate from it. Localization and segmentation of the OD are important tasks in retinal image analysis. The OD shape is an important indicator of many ophthalmic pathologies and also its localization is a prerequisite stage in many retinal image analysis algorithms. Correct segmentation of the OD contour is a non-trivial problem, since the natural variation in the characteristics of the OD is a major difficulty for defining the contour. In addition, blood vessels crossing the OD boundary as well as pathological conditions can negatively influence the OD segmentation process.

There are several works on the automatic segmentation of OD in retinal images which can mainly be grouped into four categories, namely template-based methods [42–45], deformable model methods [46–51], morphological-based approaches [52–54], and pixel classification methods [55, 56].

2.2.1 Template-based Methods

Template-based methods obtain the OD boundary approximations by defining a template for OD and using an algorithm which matches the template with different parts of the input image and finds the similarity between them. The matching process moves the template to all possible positions in the image and computes a numerical index that indicates how well the template matches the image in that position. Template-based techniques are flexible and relatively straightforward to use, which makes them one of the most popular approaches for OD detection. Their applicability is limited mostly by the available computational power, as identification of big and complex templates can be time-consuming.

In this category, Aquino *et al.* [42] follow a voting-type algorithm among three independent detection methods to locate a pixel within the OD as initial information to define a starting sub-image. Then morphological and edge detection algorithms are applied on the sub-image to segment the OD in the red and green channels separately. In both channels, the OD boundaries are approximated using the Circular Hough Transform (CHT) and finally the one with higher score in the CHT is selected. The method proposed by Wong *et al.* [43] uses a level-set approach to obtain the OD boundary, that is afterwards smoothed by fitting an ellipse.

A general energy function proposed by Zheng *et al.* [44], which integrates priors on the boundaries of the optic disc and optic cup, as well as on the minimum rim thickness. The optic cup and disc are segmented by using an energy function in a global optimization framework with a graph

cut technique. Recently, Giachetti *et al.* [45] proposed a multiresolution ellipse fitting method which combines a radial symmetry detector and a vessel density map to detect the OD in low-resolution image. Afterwards, the OD boundary is determined using refined elliptic contours on the mid-resolution and high-resolution images. The final segmented contour is improved with a snake-based refinement algorithm.

2.2.2 Deformable Model Methods

Deformable models methods try to delineate the optic disc as close as possible. These methods begin by estimating the OD boundary using *a priori* knowledge about the location, size and shape of OD, then this estimate is modified iteratively using optimization techniques for minimizing defined energy terms. Deformable models methods are autonomous and self-adapting in search for a minimal energy state and they are relatively insensitive to noise and other ambiguities in the images. As disadvantage, these methods can stuck in local minima states and their accuracies are dependent on the convergence criteria used in the energy minimization technique. These approaches can be classified into two categories: free-form deformable models, such as snakes, and parametrically deformable models, such as active shape models (ASMs).

Regarding the deformable model approaches, Lowell *et al.* [46] determine the OD location by finding the maximum of a correlation filter using a specialized template. Afterwards, the OD is segmented by means of a deformable contour based on a global elliptical model and on local deformation. In the snake model proposed by Xu *et al.* [47], after each snake deformation, an unsupervised approach labels the contour points as edge- or uncertain-points. Then the classification result is used to refine the OD boundary before repeating the contour deformation.

Li and Chutatape [48] proposed a method which extracts a point distribution model from the training set using several landmarks on OD boundaries and on main vessels inside the OD. Then a modified active shape model is used by an iterative matching algorithm to locate the OD and refine the disk boundary. Joshi *et al.* [49] modified a region-based active contour model. They improved the Chan–Vese model by using local red channel intensities and two texture feature spaces in the neighborhood of the pixels under analysis.

The method proposed in [50] uses template matching and a directional matched filter to localize the OD. For OD segmentation, the authors first remove the blood vessels and bright regions using alternating sequential filtering and morphological operations. Then a fast and hybrid level

set segmentation method with optimized parameters is used which combines the region information and local edge vector to drive the deformable contour converging to the true OD boundary. In the method proposed by Hsiao *et al.* [51], the Canny edge detector and the Hough transform are used for obtaining the edge map. Afterwards, the edge map is used as an initial contour in supervised gradient vector flow snake which consists of a snake deformation stage and a contour supervised classification stage.

2.2.3 Morphological-based Approaches

Morphological-based methods extract the OD boundary with a set of non-linear operators that act on images by using structuring elements. Mathematical morphology can extract important shape characteristics and also remove irrelevant information.

In the group of mathematical morphology algorithms for OD segmentation, Reza *et al.* [52] threshold the green component in order to obtain a binary image with isolated bright parts. Then, morphological opening is used to detect the connected components and to remove the small ones. Afterwards, extended maxima operator and minima imposition are used for extracting the OD and exudate boundaries. In [53], an adaptive mathematical morphology approach is used in two stages. In the first stage a coarse detection of OD boundary is obtained and in the second stage the results are improved. The method described in [54] uses principal component analysis in the first stage to obtain a grey image with an improved representation of the OD. After removing the vessels, a variant of watershed and stochastic watershed are applied. Finally, a geodesic transformation is used to discriminate the watershed regions as OD or non-OD regions.

2.2.4 Pixel Classification Methods

Pixel classification methods are machine learning techniques that can be used to assign a class to the pixels in an image as OD region or non-OD region. Pixel-based classification methods use various features such as intensity, texture from each pixel and its surroundings to find the optic disc. One of the advantages of a pixel classification method is that it avoids the potentially much larger bias in other categories where methods use only one or two feature detectors. On the other hand, one of the limitations in supervised pixel classification methods is that these methods require a training phase, in an always limited training set.

In the pixel-based classification category, Abràmoff *et al.* [55] proposed a method where 253 features for each pixel are extracted, such as pixel intensity, Gaussian steerable filter bank features

from hue, saturation, brightness space and also the variance in the red, green, and blue channels in a small region around the pixel. Then the most discriminant features (12 features) are selected using a sequential forward-floating search and finally each pixel is classified into rim, cup, or background using the set of selected features and a k-nearest neighbor classifier.

Recently, Cheng *et al.* [56] proposed a method which classifies each superpixel as disc or non-disc region using histograms with enhanced contrast and texture features. Superpixels are local and coherent regions that provide local image information. The authors used the simple linear iterative clustering (SLIC) algorithm to aggregate nearby pixels into superpixel. Afterwards, superpixel classification is used for initialization of the disc boundary followed by a deformable model for getting the final contour.

2.2.5 Optic Disc Segmentation Evaluation

Most of the optic disc segmentation methods are evaluated on two publicly available databases, the ONHSD and MESSIDOR datasets, which are described in Appendix A. The OD regions are manually delineated by experts for the images of these datasets. Table 2.2 shows the performance of some of mentioned OD segmentation methods. The OD segmentation performance on the MESSIDOR dataset is evaluated based on the average of overlapping score ($\bar{S}$) [42]. The overlapping score (S) measures the common area between the OD region obtained using the automatic method (A) and the region delimited by experts (E), being defined by

$$S = \frac{\text{Area}\,(A \cap E)}{\text{Area}\,(A \cup E)} \tag{2.4}$$

In ONHSD dataset four clinicians marked 24 OD boundary points and the methods are compared by the percentage of images in the excellent-fair category using a discrepancy value [46]. The discrepancy, δ_j on image j is defined by

$$\delta_j = \sum_i \frac{\left| m_i^j - \mu_i^j \right|}{\sigma_i^j + \varepsilon} \tag{2.5}$$

where μ_i^j and σ_i^j are, respectively, the mean and standard deviation of values obtained by four clinicians on spoke i of image j, m_i^j is the location of the boundary using the segmentation method on spoke i of image j, and ε is a small value to prevent division by zero when the clinicians are in exact agreement and was set equal to 0.5.

As shown in Table 2.2, the template-based method by Aquino *et al.* [42] reports the highest percentage of images in the Excellent-Fair subjective category, while both Cheng *et al.* [56] and Giachetti *et al.* (2014) [45] obtained the average of overlapping score equal to 0.88 on the images of MESSIDOR dataset.

Both the template-based and deformable model methods are based on the edge characteristics. The performance of these methods very much depends on the differentiation of edges from the disc and other structures. The template-based approaches are usually more robust to color, contrast and illumination variations and have better performance in the presence of severe pathological conditions when compared to the methods in other categories.

Table 2.2: The performance of optic disc segmentation methods.

Methods	Dataset	$\bar{S}$	Excellent-Fair subjective category
Aquino *et al.* (2010) [42]	ONHSD	-	97%
	MESSIDOR	-	86%
Giachetti *et al.* (2014) [45]	MESSIDOR	0.88	-
"Simple" Lowel *et al.* (2004) [46]	ONHSD	-	47%
"DV-Hough" Lowel *et al.* (2004) [46]	ONHSD	-	81%
"Temporal Lock" Lowel *et al.* (2004) [46]	ONHSD	-	83%
Yu *et al.* (2007) [50]	MESSIDOR	0.84	-
Morales *et al.* (2013) [54]	ONHSD	0.80	-
	MESSIDOR	0.82	-
Cheng *et al.* (2014) [56]	MESSIDOR	0.88	-

$\bar{S}$: Average of overlapping score

2.3 Artery/Vein Classification

Retinal blood vessel classification into arteries and veins is a necessary phase for the automatic detection of vascular changes, and for the calculation of characteristic signs associated with systemic diseases. Several methods have been proposed for the A/V classification [57–71] based on different visual and geometrical features which are used for the discrimination between veins and arteries. Arteries are bright red while veins are darker, and in general artery calibers are smaller than vein calibers. Vessel caliber can be affected by diseases, therefore this is not a reliable feature for A/V classification. Arteries also have thicker walls, which reflect the light as a shiny central reflex strip [72]. Another characteristic of the retinal vessel tree is that, at least in the region near the optic disc (OD), veins rarely cross veins and arteries rarely cross arteries, but both types can bifurcate to narrower vessels, and veins and arteries can cross each other [72]. For this reason, tracking of arteries and veins in the vascular tree is possible, and has been used in some methods to analyze the vessel tree and classify the vessels [57–60].

A semi-automatic method for analyzing retinal vascular trees was proposed by Martinez-Perez *et al.* in [57], using geometrical and topological properties of single vessel segments and subtrees. First, the skeleton is extracted from the segmentation result, and significant points are detected. For the labeling, the user should point to the root segment of the tree to be tracked, and the algorithm will search for its unique terminal points and in the end, decide if the segment is an artery or a vein. Another method similar to this was proposed by Rothaus *et al.* [58], which describes a rule-based algorithm to propagate the vessel labels as either artery or vein throughout the vascular tree. This method uses existing vessel segmentation results, and some manually-labeled starting vessel segments.

Lau *et al.* [59] constructed their graph over a restricted region of interest around the optic disc and then assigned the vessel labels by finding the optimal forest in the subgraphs. Joshi *et al.* [60] first separated their vascular graph using Dijkstra's shortest-path algorithm to find different subgraphs. They then labeled each subgraph as either artery or vein using a fuzzy C-mean clustering algorithm.

Grisan *et al.* [61] developed a tracking A/V classification technique that classifies the vessels only in a well-defined concentric zone around the optic disc. Then, by using the vessel structure reconstructed by tracking, the classification is propagated outside this zone, where little or no information is available to discriminate arteries from veins. This algorithm is not designed to consider the vessels in the zone all together, but rather partitions the zone into four quadrants, and

works separately and locally on each of them.

Vazquez *et al.* [62] described a method which combines a color-based clustering algorithm with a vessel tracking method. First the clustering approach divides the retinal image into four quadrants, then it classifies separately the vessels detected in each quadrant, and finally combines the results. Then, a tracking strategy based on a minimal path approach is applied to join the vessel segments located at different radii in order to support the classification by voting.

A piecewise Gaussian model to describe the intensity distribution of vessel profiles has been proposed by Li *et al.* [63]. In this model, the central reflex has been considered. A minimum distance classifier based on the Mahalanobis distance was used to differentiate between the vessel types using features derived from the estimated parameters.

Kondermann *et al.* [64] described two types of features and two classification methods, based on support vector machines and neural networks, to classify retinal vessels. One type of features is profile-based, while the other is based on the definition of a region of interest (ROI) around each centerline point. To reduce the dimensionality of the feature vectors, they used multiclass principal component analysis (PCA).

Niemeijer *et al.* [65] proposed an automatic method for classifying retinal vessels into arteries and veins using image features and a classifier. A set of centerline features is extracted and a soft label is assigned to each centerline, indicating the likelihood of being a vein centerline pixel. Then the average of the soft labels of connected centerline pixels is assigned to each centerline pixel. They tested different classifiers and found that the k-nearest neighbor (kNN) classifier provides the best overall performance. In [66], the classification was enhanced as a step in calculating the Arteriolar-to-Venular Ratio (AVR).

Zamperini *et al.* [67] focused on determining effective features for A/V classification. They compared color, spatial, and size features and concluded that a mix of color and position features provided the best results. By performing a greedy backward feature selection on a set of 86 features, a set of 16 features was selected. They use different linear and nonlinear classifiers where the Linear Bayes classifier has the best performance. Mirsharif *et al.* [68] use a three-step supervised classification method. They first enhance the retina image, then extract different pixel color features to separate major arteries from veins. Afterwards, the misclassifications at bifurcation points are corrected using information from structural characteristics of the retinal vascular tree.

Muramatsu *et al.* [69] used linear discriminant analysis and a set of six simple features to

classify main vessels in a ring area around the optic disc. The feature set includes color intensities for centerline pixels and their contrast differences in a 5×5 pixel region around them inside the vessel, and in a 10×10 pixel region outside the vessel. Relan *et al.* [70] used a Gaussian mixture model on small vessel patches to classify the main vessels in each optic disc-centred quadrant. Recently they improved their method using a least square-support vector machine classifier [71], which classifies the main vessels in a defined region of interest around the optic disc.

2.3.1 A/V Classification Evaluation

The performance of the described A/V classification methods is shown in Table 2.3 where the methods are compared based on the obtained accuracy and the area under the receiver operating characteristic (ROC) curve. Some of these methods classify the whole vascular tree while the other ones only classify the main vessels where the small vessels are removed using a threshold for the vessel calibers. It should be noted that the vessel caliber threshold for the selection of main vessels is not consistent for all methods. The mentioned A/V classification methods are evaluated on different sets of images, and on different region of interest (ROI). The ROI is defined as the ring area between the circumferences with various radii around the optic disc.

The results obtained by Grisan *et al.* [61] were compared with those provided by a manual classification on a validation set of 443 vessels on the concentric ring between the circles with radii $2 \times R_{OD}$ and $4 \times R_{OD}$, where R_{OD} is the optic disc radius. They reached an overall classification accuracy of 87.6%, which increases to 93.3% if only the diagnostically important retinal vessels are considered.

For evaluation,Vazquez *et al.* [62] used VICAVR dataset with 58 images and they reached a classification accuracy of 88.8% for the vessel segments in the region between circles with radii $2 \times R_{OD}$ and $3 \times R_{OD}$. The overall classification accuracy in the method proposed by Li *et al.* [63] was 85.5%, when evaluated in 505 vessel segments. Kondermann *et al.* [64] showed that the neural network classifier using ROI feature vector can classify 95.32% vessel pixels correctly, but when using the output of a segmentation algorithm instead of hand-segmented images as basis for the classification the results deteriorate by 10% on average.

The method proposed by Niemeijer *et al.* [65] was used on the 20 images of the DRIVE dataset, an area under the receiver operator characteristic curve of 0.88 for correctly assigning centerline pixels of main vessels was obtained. On the same dataset Mirsharif *et al.* [68] reported the accuracy values of 0.84 and 0.90 for the entire image and the ring area between to circles with

$2 \times R_{OD}$ and $3 \times R_{OD}$ radii, while Muramatsu *et al.* [69] achieved the accuracy of 0.93 for main vessels inside the same region.

Table 2.3: The performance of A/V classification methods.

Methodology	Dataset	Region	Vessel type	ACC	AUC
Grisan *et al.* (2003) [61]	24 images	Ring area ($2R_{OD} < d < 4R_{OD}$)	Main	0.933	-
			All	0.876	-
Li *et al.* (2003) [63]	505 segments	-	-	0.855	-
Kondermann *et al.* (2007) [64]	4 images	Entire retina area	Main	0.953	-
Niemeijer *et al.* (2009) [65]	DRIVE	Entire retina area	Main	-	0.88
Niemeijer *et al.* (2011) [66]	INSPIRE-AVR	Ring area ($2R_{OD} < d < 3R_{OD}$)	All	-	0.84
Vazquez *et al.* (2013) [62]	VICAVR	Ring area ($2R_{OD} < d < 3R_{OD}$)	All	0.8768	0.89
Joshi *et al.* (2014) [60]	50 images	Entire retina area	Main	0.9642	-
			All	0.9144	
Lau *et al.* (2013) [59]	2446 images	Ring area ($2R_{OD} < d < 5R_{OD}$)	All	0.989	-
Relan *et al.* (2013) [70]	35 images	Ring area ($2R_{OD} < d < 3R_{OD}$)	Main	0.92	-
Relan *et al.* (2014) [71]	70 images	Ring area ($2R_{OD} < d < 3R_{OD}$)	Main	0.9488	-
		Ring area ($2R_{OD} < d < 4.5R_{OD}$)		0.9396	
Mirsharif *et al.* (2013) [68]	DRIVE	Entire retina area	Main	0.8405	-
		Ring area ($2R_{OD} < d < 3R_{OD}$)		0.9016	
Muramatsu *et al.* (2011) [69]	DRIVE	Ring area ($2R_{OD} < d < 3R_{OD}$)	Main	0.93	-
Zamperini *et al.* (2012) [67]	42 images	Ring area ($2R_{OD} < d < 3R_{OD}$)	Main	0.931	-

R_{OD}: Radius of optic disc

d: distance from optic disc center

ACC: Accuracy

AUC: Area under curve

2.4 Vascular Changes Assessment

Vessel dilation is a well-known phenomenon in diabetes and significant dilation and elongation of retinal arterioles, venules, and their macular branches occur in the development of diabetic macular edema that can be linked to hydrostatic pressure changes. Retinal arteriolar narrowing and vessel color changes are known responses of hypertension. These vessel changes are not limited to diabetes and hypertension, and are also associated with other cardiovascular and cerebrovascular diseases as well [2].

Many methods have been proposed for retinal vessel segmentation and classification, but relatively few have been described for fully automatic detection and analysis of changes in the vasculature. Among several sings related to the vascular changes, the Arteriolar-to-Venular Ratio (AVR), which is a parameter derived from vessel caliber measurements in a specific region of retinal images, is generally used as a descriptor of generalized arteriolar narrowing. A decreased ratio between the width of retinal arteries and veins (AVR) is well established to be predictive of stroke and other cardiovascular events in adults, as well as an indicator of diabetes and hypertension.

Ruggeri *et al.* [73] proposed a method that starts with the detection of the vessel structure by highlighting the vessel network and then uses a tracking algorithm. After locating the optic disc (OD), the concentric zone around the optic disc is partitioned into four quadrants and in every quadrant a fuzzy C-mean classifier labels the vessel pixels as artery or vein. Then, the AVR value is obtained by estimating vessel calibers in the region around the optic disc. Tramontan *et al.* improved this algorithm by enhancing the vessel tracking phase and the structural artery/vein discrimination features [74].

Niemeijer *et al.* [66] proposed an automated method which combines tobogganing and vessel pixel classification for the measurement of vessel calibers and uses supervised position regression for the detection of the optic disc center. For classifying the vessels, the authors tested different classification approaches and found that the linear classifier has better performance. Finally AVR values are calculated using Knudtson's revised formula [75]. The method proposed by Muramatsu *et al.* [69] includes optic disc and vessel segmentation, vessel classification using a linear discriminant classifier and the selection of two pairs of major vessels in the upper and lower temporal regions for AVR calculation.

SIRIUS [76] (System for the Integration of Retinal Images Understanding Services) is a web application which has been developed to be used by specialists for computing the AVR value. In this semi-automatic application, the specialist selects the optic disc and three circles, concentric to

the optic disk. Then the retinal vessel tree is automatically segmented. Afterwards, the intersect points of the three concentric circles and the extracted retinal vessel tree are used for the estimation of vessel calibers. In the next step, the specialist manually labels each of those selected points into vein or artery, and finally the AVR value is calculated.

Schuster *et al.* [77] developed a semi-automated image recognition and analysis tool for the determination of the AVR value in retinal images. They use thresholding for vessel recognition and vessel width is calculated in a semi-automated procedure. Bhuiyan *et al.* [78] presented a semi-automated evaluation tool which assists physicians in measuring vessel caliber from poor quality images. The system uses texture and edge information to measure vessel caliber. The graders have the ability to remove the parts of measured widths which are incorrect. The obtained vessel widths were used for calculating the Central Retinal Arterial Equivalent (CRAE) and Central Retinal Venular Equivalent (CRVE).

More recently, a semi-automated system, the Singapore Eye Vessel Assessment (SIVA) system has been proposed for quantifying the retinal vasculature morphology [79]. This system uses automated methodologies for detecting important retinal landmarks and construct a representation of the vasculature. Then, trained graders are able to edit the detected structures, after which several measurements can be obtained.

Fritzsche in [80] described a fully automated method that finds changes in retinal vessels including changes in vessel width. Many prior methods considered global properties of the retina [81, 82]. These methods captured summary descriptions, such as the average width or the ratio of widths of the retinal vasculature, and compared these measures with those from the same individual obtained in previous visits or with population distributions.

A new and accurate method to measure the width of retinal blood vessels in fundus photography is proposed in [83] by Xu *et al.* which is based on a graph-theoretic algorithm. The two boundaries of the same blood vessel are segmented simultaneously by converting the two-boundary segmentation problem into a two-slice, three-dimension surface segmentation problem, which is further converted into the problem of computing a minimum closed set in a node-weighted graph.

In addition to the signs related to vessel width, there are other vascular signs which can provide useful information to aid prevention and treatment of diseases. The geometry of a vascular bifurcation can be summarized by the bifurcation angle and the bifurcation coefficient. Bifurcation angle is the angle subtended between the two daughter arterioles at the vascular junction. Changes

in bifurcation angle may reflect alterations in blood flow, endothelial dysfunction, and attenuation in oxygen saturation [84]. Increased angles have been associated with decreased retinal blood flow, whereas decreased angles are associated with ageing and hypertension [85].

The bifurcation coefficient measures the changes in the total cross-sectional area across the bifurcation which is the relationship between the diameter of the trunk vessel and the diameter of the two daughter vessels. An increased bifurcation coefficient represents wider branch vessels, and a decreased branching coefficient indicates narrower branch compared with the trunk vessel. Any changes in the bifurcation geometry are known to occur with increasing age and in diseased coronary arteries [86].

Normal retinal blood vessels are straight or gently curved. In some diseases, the blood vessels become tortuous, i.e. they become dilated and take on a twisting path. The dilation is caused by radial stretching of the blood vessel and the serpentine path occurs because of longitudinal stretching. The tortuosity may occur only in a small region of the retinal blood vessels, or it may involve the entire retinal vascular tree [87]. It has been shown that there is an association between arteriolar tortuosity and retinopathy of prematurity [88]. The degree of tortuosity of a vessel can be calculated as the ratio between the distance a vessel travels from two vessel points, and the shortest distance between the same points drawn by a straight line [86].

Neural network based retinal image analysis [89] and integrated analysis of vascular and non-vascular changes from color retinal fundus image sequences by Narasimha-Iyer *et al.* [90] are also major notable efforts in integrating the segmentation of the different retinal features.

One way for analyzing the branching pattern is by using mathematical techniques, such as fractal and local fractal dimension. Fractals are based on the concept of self-similarity of spatial geometrical patterns despite a change in scale or magnification so that small parts of the pattern exhibit the pattern's overall structure. The fractal dimension describes how thoroughly the pattern fills two-dimensional spaces [86]. Previous studies on the analysis of branching patterns demonstrated the fractal nature of the retinal blood vessel network and that the fractal dimension can be used to identify a pathology [91, 92].

2.5 Concluding Remarks

Assessment of retinal vascular changes can provide clinically useful information to aid prevention and management of diseases such as diabetes and hypertension. Detecting changes in individual vessels requires a number of capabilities. Algorithms are needed to automatically extract the vasculature tree, accurately locate vessel boundaries, classify arteries and veins, detect the optic disc, determine region of interest, and ultimately to calculate the signs related to vascular changes.

The methods that were described in this chapter still have some limitations. Most of these methods cannot achieve proper results in images with different characteristics such as size and camera field of view. The performance of these methods decreases in the images with variations of contrast and illumination, the presence of exudates and peripapillary atrophy caused by diabetic retinopathy, risk of macular edema, and the blurredness of images due to severe cataracts. Another limitation is that the mentioned systems and methods are mostly semi-automatic and require user's interaction.

In the next chapters, new retinal image analysis techniques are proposed, namely vessel caliber estimation, artery/vein classification and optic disc segmentation. A pipeline of these methods allows the computation of important vessel related indexes, namely the Central Retinal Arteriolar Equivalent (CRAE), Central Retinal Venular Equivalent (CRVE) and Arteriolar-to-Venular Ratio (AVR), as well as various geometrical features associated with vessel bifurcations, as will be described in Chapter 5.

Besides the above mentioned developments in the assessment of retinal vessels, other areas of research are also active in fundus image analysis [86, 93], namely:

- Optic nerve head analysis;
- Arteriolar color changes (copper-wiring/sliver-wiring);
- Detection of retinal lesions;
- Detection of irregularly shaped hemorrhages;
- Detection of rare but major pathology such as neoplasms and scarring;
- Detection of lesion distribution patterns, for example drusen;
- Segmentation of atrophy, including geographic atrophy;
- Content-based image retrieval for abnormality detection;
- Change over time detection for abnormality assessment.

Chapter 3

Optic Disc Segmentation

The optic disc (OD) is one of the main structures in a retinal image and its shape and appearance are important for the detection of glaucoma and assessment of white lesions related with diabetic retinopathy. The OD is also a landmark for other retinal features, such as the distance between the OD and the fovea, which is often used for estimating the location of the macula [94]. In addition, OD segmentation is an important stage for the calculation of indexes related to vascular changes, such as the Arteriolar-to-Venular Ratio (AVR) [95] as the estimation of this index requires a previous OD segmentation in order to determine the region of interest [75]. Since the intensity inside OD is variable and the OD region can be degraded by different types of retinal lesions, OD segmentation is a challenging and still open task mainly for reducing the processing time and, in pathological images, for improving the performance.

In this chapter, a new method for OD segmentation is proposed which can be classified as a template-based solution. The material herein described is based in the paper *"Optic Disc Segmentation using the Sliding Band Filter"* [9]. The main motivation was the development of a fully automatic method, able to produce useful results even in the presence of severe pathological conditions and showing a great independence from image acquisition settings. In our approach the filter response suitable for the enhancement of bright circular regions, the sliding band filter (SBF), is used for estimating both the OD center and the OD boundary. For high resolution images, the sliding band filter (SBF) is used twice. The first SBF is applied on downsampled images to estimate the optic disc center (ODC) which is then used for defining a region of interest where the second SBF is afterwards applied for fine boundary extraction.

The proposed method is fully automatic which segments the optic disc independently of image characteristics such as size and camera field of view. This approach is robust to variations of

contrast and illumination, the presence of exudates and peripapillary atrophy caused by diabetic retinopathy, risk of macular edema, and the blurredness of images due to severe cataracts. From now on this approach is shortly called the SBF-based OD segmentation, or simply SBF-based method.

Since the vessel extraction from retinal images is an important step in the proposed optic disk segmentation approach this chapter starts by describing the vessel segmentation method in Section 3.1. Afterwards, Section 3.2 presents the OD segmentation. The results in images of three different datasets are presented in Section 3.3, where a comparison with the manual segmentation is also included. Finally, Section 3.4 summarizes the concluding remarks.

3.1 Vessel Segmentation

In this section, a vessel segmentation method is described which is an important step in the proposed optic disc segmentation method. This method has been used for the vessel removal in Section 3.2.1 and for the initial optic disc detection in Section 3.2.3. The extracted vessels are also used for the graph generation as a phase for the A/V classification in Section 4.1.1 and for the measurement of vessel caliber in Section 5.2.

The method proposed by Mendonça *et al.* [8] was used for segmenting the retinal vasculature, after being adapted for the segmentation of high resolution images [22]. This method follows the combination of a centerline detection with a region growing approach in three phases. The first one is a pre-processing phase, where the intensity is normalized by subtracting an estimation of the image background, obtained by filtering with a large arithmetic mean kernel. In the next phase, centerline candidates are detected using information provided from a set of four directional Difference of Offset Gaussian filters, then connected into segments by a region growing process, and finally the centerline segments are validated based on their intensity and length characteristics. The third phase is vessel segmentation, where multi-scale morphological vessel enhancement and reconstruction approaches are followed to generate binary maps of the vessels at four scales. The final image with the segmented vessels is obtained by iteratively combining the centerline image with the set of images that resulted from the vessel reconstruction. This method achieved an accuracy of 0.9466 for the images of the DRIVE dataset, with an overall sensitivity and specificity of 0.7467 and 0.9762, respectively, while the obtained accuracy, sensitivity and specificity values for the images of STARE dataset were 0.9487, 0.7194 and 0.9759, respectively [22]. Figure 3.1 shows examples of vessel segmentation results for images of DRIVE, STARE, ONHSD, INSPIRE-AVR and MESSIDOR datasets, which are introduced in Appendix A.

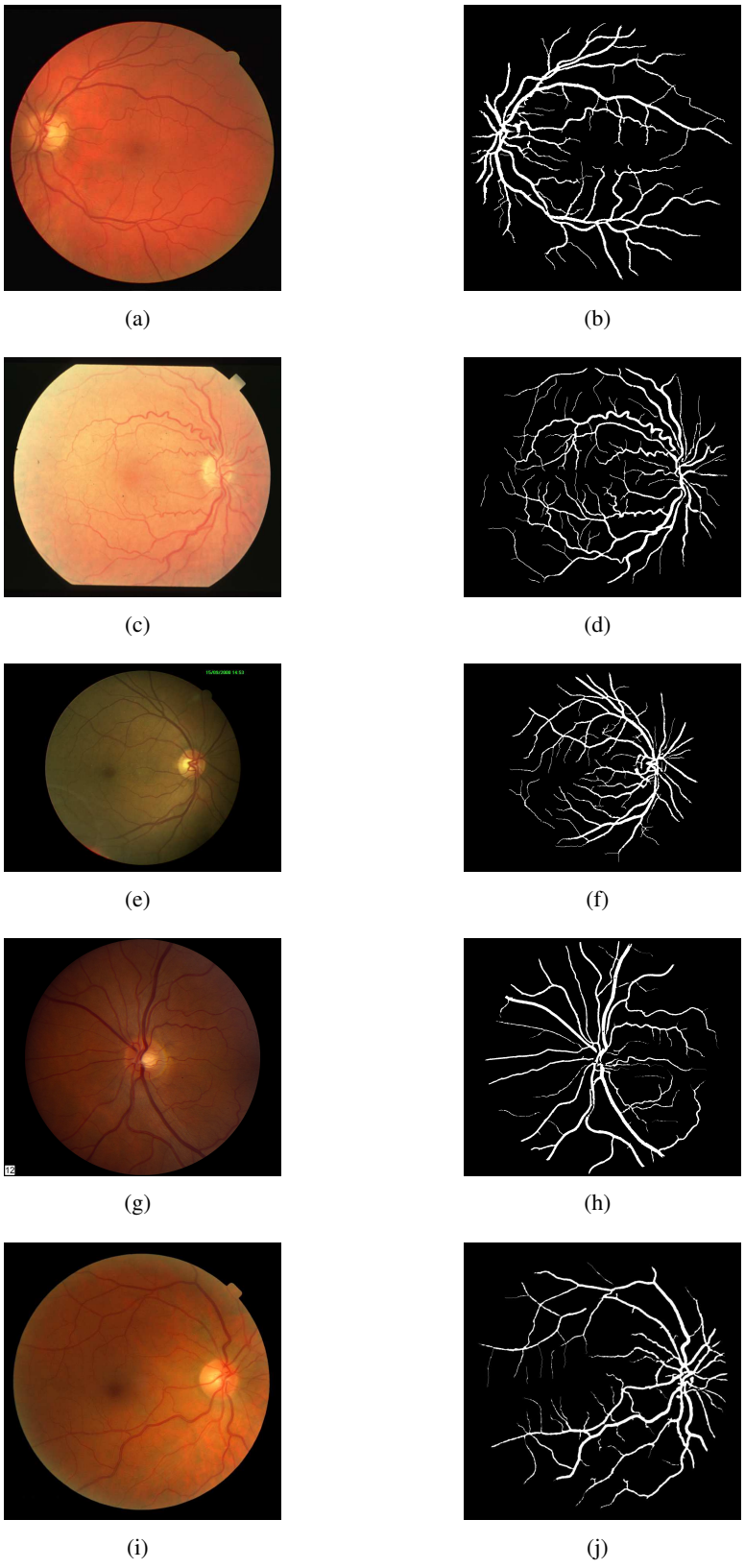

Figure 3.1: Examples of vessel segmentation results; left column: Original images; right column: segmentation result; (a), (b) DRIVE dataset; (c), (d) STARE dataset; (e), (f) ONHSD dataset; (g), (h) INSPIRE-AVR dataset; (i), (j) MESSIDOR dataset.

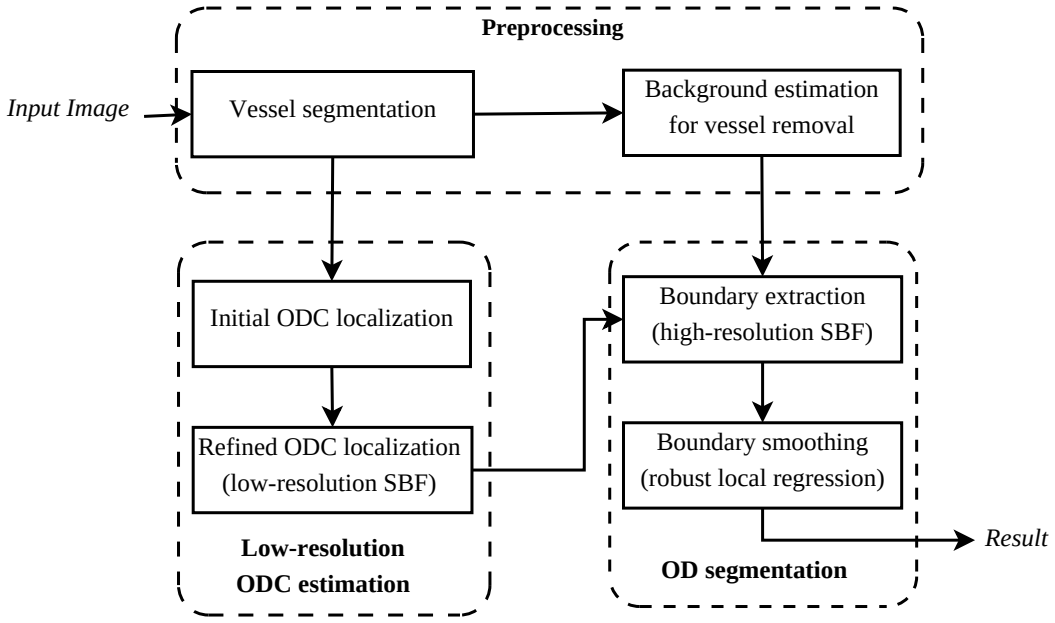

Figure 3.2: Block diagram of SBF-based optic disc segmentation.

3.2 Optic Disc Segmentation Using Sliding Band Filter

In this section, a new SBF-based OD segmentation approach is described. Figure 3.2 depicts the block diagram of the proposed OD segmentation method. The main phases are: 1) preprocessing, for vessel removal; 2) low-resolution ODC estimation, for obtaining an approximated location of the ODC on downsampled images; 3) OD segmentation, for extracting the OD boundary on high-resolution images.

For decreasing the interference of vessels in the OD segmentation, the method starts by the segmentation of vascular tree, followed by inpainting the vessel pixels with an estimation of the neighbouring background. In the next phase, an initial location for ODC is obtained aiming at defining a region of interest where, for reducing the computation time, a low-resolution SBF is applied to a downsampled image. As a result, a new candidate for the ODC location is selected from the filter response. In the third phase, the high-resolution SBF is applied to the region around the new ODC candidate on the original image. The parameters of this filter are automatically adapted to the image size and the camera field of view. The OD segmentation is finalized by detecting the maximum response of the SBF and applying a smoothing algorithm to the extracted boundary. In the following subsections, detailed descriptions of each phase are presented.

3.2.1 Preprocessing

Since the OD region is characterized by a yellowish bright region, it shows high contrast in both red and green components of image. Therefore the original color image is converted to a gray-scale one (I_{RG}), where the pixel values at the (x,y) positions are obtained from the red (I_R) and green (I_G) components of the RGB image using the equation

$$I_{RG}(x,y) = (I_R(x,y)^2 + I_G(x,y)^2)^{\frac{1}{2}} \tag{3.1}$$

The OD segmentation process can be negatively influenced by the presence of the retinal vessels. In order to decrease this influence, the vessels are segmented and then replaced by an estimate of their neighbouring background in the image I_{RG}. The method developed by Mendonça *et al.* [8,22] is used for vessel segmentation which was briefly described in Section 3.1. Figure 3.3(b) shows the segmented vascular tree for the original image of Figure 3.3(a).

The background is estimated by gray-level morphological closing applied to I_{RG} after removing the vessel pixels. The closing of an image I is a dilation followed by an erosion with respect to a structuring element B, defined by

$$(I \bullet B)(x,y) = (I \oplus B) \ominus B \tag{3.2}$$

where $\oplus$ and $\ominus$ denote the dilation and erosion operators, respectively. A non-flat, ball-shaped structuring element is considered which is defined by

$$B(i,j) = \frac{1}{r}\left(r^2 - \min(r^2, i^2 + j^2)\right)^{0.5}, \quad \text{for} \quad -r \leq (i,j) \leq r \tag{3.3}$$

For vessel caliber measurement a distance transform is applied to the segmented vascular tree and the result of this is the labelling of each vessel pixel (p) with its distance to the closest boundary point, d_p. After that, After that, the vessel caliber for each vessel centerline pixel, $vc(p)$, is estimated by $vc(p) = 2d_p - 1$. The radius of the structuring element, r, is given by $r = \frac{1}{2}\max(vc(p))$. Figure 3.3(c) shows the final image after replacement of the vessel pixels with local background estimates.

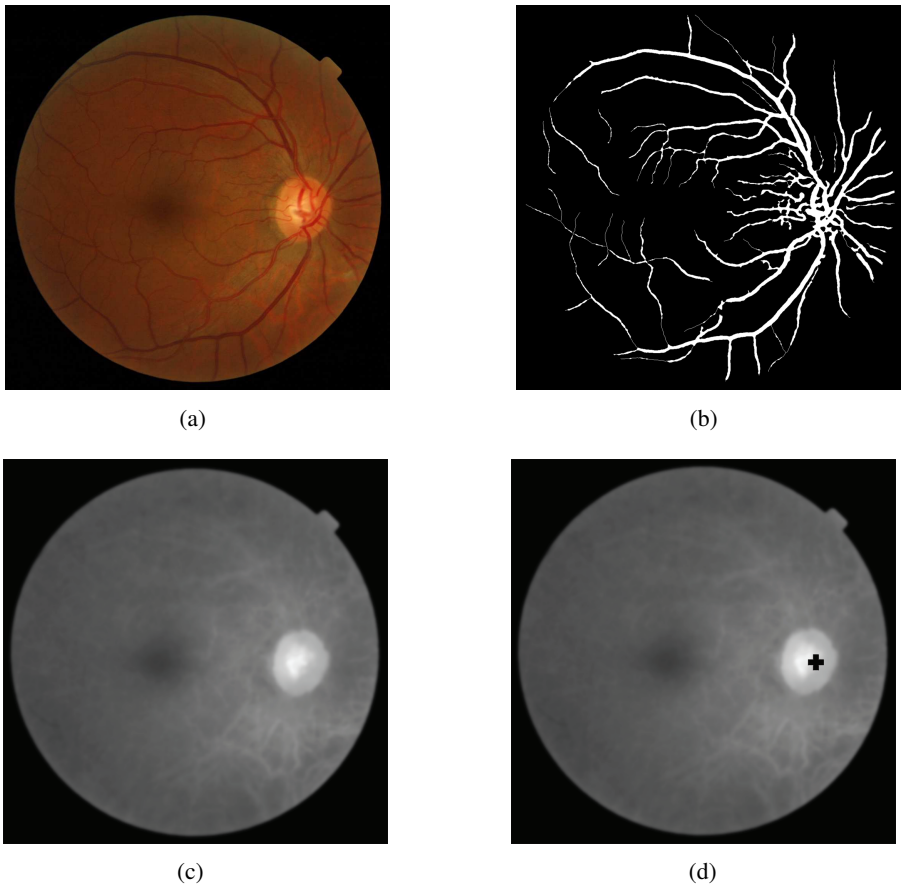

(a) (b)

(c) (d)

Figure 3.3: (a) Original image; (b) Vessel segmentation image; (c) Result of vessel pixels elimination; (f) I_{RG} image with the initial ODC (black cross).

3.2.2 Sliding Band Filter

The SBF is a member of the convergence index (CI) filter class, whose output is a measure of the convergence degree of the gradient vectors calculated for the pixels belonging to the filter support region [96–98]. For each pixel with spatial coordinates (x,y), the convergence index (C) is defined by

$$C(x,y) = \frac{1}{M} \sum_{(k,l)\in R} \cos\theta_i(k,l) \tag{3.4}$$

where $\theta_i(k,l)$ is the orientation angle of the gradient vector at point (k,l) with respect to the line, with direction i, that connects (k,l) to (x,y). M is the number of points in the filter support region R.

Distinct members of CI filters use different definitions for the support region, R. The support region of the coin filter (CF) is a circle with variable radius [99], while the support region of the iris

filter (IF) can change in each direction [100]. A ring shaped region with varying radius and fixed width is the support region of the adaptive ring filter (ARF) [101]. The support region of the SBF is a fixed width band whose position in each direction changes for maximizing the convergence index value in each point [96, 97]. For all these filters, the support region is usually restricted to a set of radial lines emerging from the point where the filter is being applied to, and equally distributed over a circular region centered at this point.

The SBF has a more generic formulation in comparison with other CI filters, which is desirable for OD segmentation due to the fact that the shape of OD differs from an exact rounded area [102]. The SBF can also be parameterized to use a narrow band and ignore the gradient information at the center of the OD, thus reducing the interference of vessels.

The SBF response at a pixel of interest $P(x,y)$ is defined by (3.5) and (3.6)

$$SBF(x,y) = \frac{1}{N}\sum_{i=0}^{N-1} C_{max}(i) \tag{3.5}$$

$$C_{max}(i) = \max_{R_{min}\leq n\leq R_{max}} \left(\frac{1}{d}\sum_{m=n}^{n+d} \cos\theta_{i,m} \right) \tag{3.6}$$

where N is the number of support region lines, $\theta_{i,m}$ represents the angle of the gradient vector at the point m pixels away from P in direction i, d corresponds to the width of the band, and R_{min} and R_{max} represent, respectively, the inner and outer sliding limits of the band. The number of support region lines (N) controls the resolution and computational cost of the SBF. The high-resolution SBF uses a higher number of support region lines, making the computation more time consuming while increasing the sensitivity of the filter to neighbouring changes; the low-resolution SBF uses a smaller number of support region lines which reduces the computation time as well as filter accuracy. Figure 3.4 presents a schematic representation of the SBF concept where the search region is defined by the inner (R_{min}) and outer (R_{max}) circles and the set of d points corresponding to maximal convergence is shown in gray; in this example only 8 support region lines are considered.

3.2.3 Low-resolution ODC Estimation

As a first step, an initial ODC location is estimated and used for defining the ROI where the SBF is applied. In this phase, both an SBF with a small number of support region lines and a downsampled image are used for reducing the computation time. The filter response gives a more accurate location for the ODC to be used in the next phase.

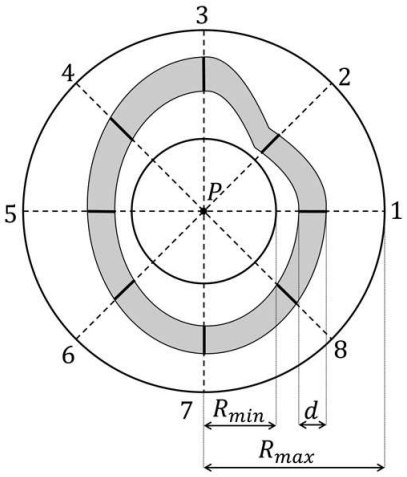

Figure 3.4: Schematics of the sliding band filter with 8 support region lines (dashed lines), where a simplified support region is depicted with the segmented lines. The gray region specifies a denser support region using a higher number of radial lines.

3.2.3.1 Initial Optic Disc Center Localization

Regarding the computational complexity of the SBF, the OD segmentation can be speed up by focusing the SBF on a limited region of interest (ROI). For this purpose, an initial ODC is estimated using the approach based on the entropy of vascular directions by Mendonça *et al.* [103], using the vessel segmented image obtained in the preprocessing phase. The initial ODC, O_{init}, is the center of this ROI (Figure 3.3(d)).

3.2.3.2 Image Downsampling

The SBF filter is computationally expensive and its application to a high-resolution image takes a lot of time. In order to reduce the computational burden, the SBF is used twice. The first SBF is applied on a large ROI of a downsampled image in order to obtain a coarse ODC location, whose position is used for establishing a smaller ROI on the original size image for applying the second SBF. To downsample an image to a common size, an image with the resolution of 760×570 pixels and 45° camera field of view (FOV) is used as reference. The images are downsampled according to the size and FOV of the reference image using the scale factor (α) that is computed by multiplying the image size scale factor (S_1) and the FOV scale factor (S_2). S_1 is defined as the quotient between the diameter of retinal image mask (d_2) and the diameter of the reference image mask (d_1).

S_2 is defined by $S_1 = \frac{D_1}{D_2}$, where D_1 and D_2 represent, respectively, the diagonal of the reference image plane and the diagonal of the actual image plane. From Figure 3.6(d), the diagonal field of view can be calculated using

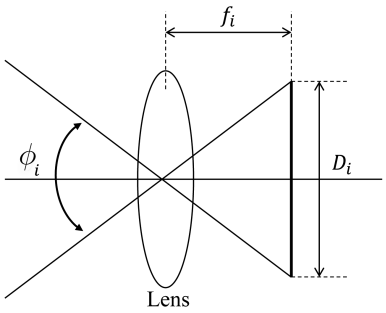

Figure 3.5: Geometric representation of camera field of view.

$$\tan\left(\frac{\phi_i}{2}\right) = \frac{D_i}{2f_i} \tag{3.7}$$

where ϕ_i is the field of view, D_i represents the diagonal of the image plane, and f_i is the camera focal length.

Using (3.7) and assuming that the focal lengths of cameras are similar ($f_1 \approx f_2$), the FOV scale factor is estimated by

$$S_2 = \frac{D_1}{D_2} = \frac{f_1 \tan(\phi_1/2)}{f_2 \tan(\phi_2/2)} \overset{f_1 \approx f_2}{\rightarrow} S_2 = \frac{\tan(\phi_1/2)}{\tan(\phi_2/2)} \tag{3.8}$$

where ϕ_1 represents the reference image FOV and ϕ_2 is the FOV of the image being processed.

Finally, the scale factor for image downsampling is calculated by

$$\alpha = S_1 S_2 = \frac{d_2 \tan(\phi_1/2)}{d_1 \tan(\phi_2/2)} \tag{3.9}$$

3.2.3.3 Low-resolution SBF

The image is downsampled using α, and afterwards, the SBF is applied to the ROI. The ROI is considered as an $w \times w$ square window centred at O_{init}. Figure 3.6(b) shows the SBF result on the ROI of Figure 3.6(a). In order to find a new candidate for ODC (O_{l1}), the locations of K candidate points with highest filter response are listed, $Q = \{(x_i, y_i),\ i = 1, 2..., K\}$. These points are represented by the dots in Figure 3.6(c). The outliers of this set are excluded based on two

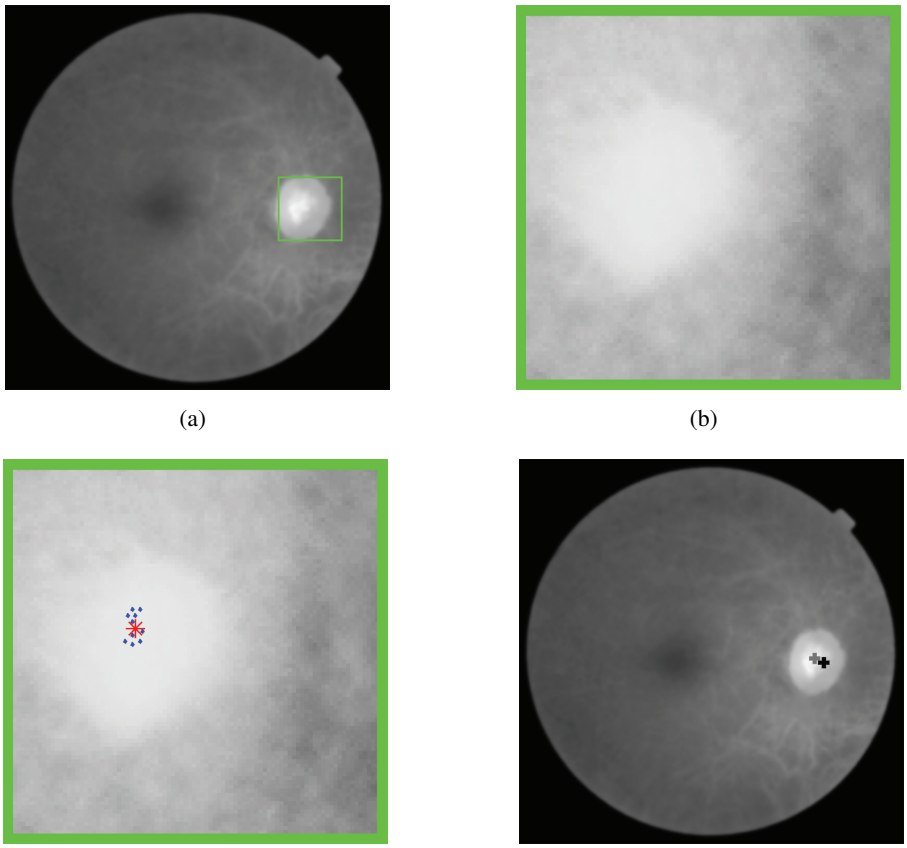

(a) (b) (c) (d)

Figure 3.6: (a) I_{RG} image with the ROI for the low-resolution SBF (square); (b) Low-resolution SBF response on ROI; (c) 10 highest values of filter response (dots) and mean value coordinates (star); (d) Initial ODC (black cross) and new ODC candidate (gray cross).

criteria: 1) the relation of its value with the highest value of the filter response; 2) distance to the centroid of the K point set. The criteria for excluding outliers are defined by (3.10) and (3.11).

$$SBF(x_i, y_i) < (1-\beta) \max_{1 \leq i \leq K} (SBF(x_i, y_i)) \tag{3.10}$$

$$\left((x_i - x_m)^2 + (y_i - y_m)^2 \right)^{0.5} > \gamma \tag{3.11}$$

where $SBF(x_i, y_i)$ is the filter response at point (x_i, y_i) using (3.5), and x_m and y_m represent the centroid of the K points. After excluding the outliers, the new centroid of the remaining points in set Q is the new candidate for ODC (O_{l1}), that will be the center of the new ROI to apply the high-resolution SBF in the next phase. The new ODC is shown with a gray cross in Figure 3.6(d).

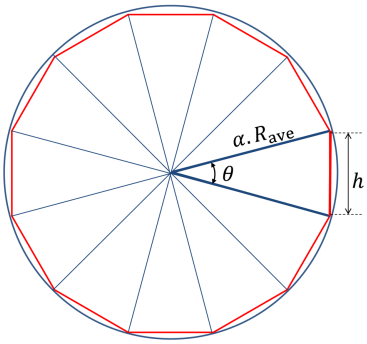

Figure 3.7: Geometric representation for calculating the number of support region lines.

3.2.4 OD Segmentation

In this phase, a high-resolution SBF is applied to the original image. High-resolution SBF is a filter with a higher number of support region lines, N. The ROI for applying the SBF is a square region around the new ODC that was calculated in the previous phase. Unlike the low-resolution version of the filter, all SBF parameters in this phase are computed using the scale factor α.

3.2.4.1 High-resolution SBF

For reducing the computation time, a smaller region for the ROI is used when compared with the ROI in the previous phase. For ROI determination, a default value of w_h pixels for the window size is then multiplied by the scale factor obtained from (3.9). The values for SBF parameters (R_{min}, R_{max} and d) depend on image size, so for each particular image they are obtained multiplying the low-resolution SBF ones by α.

As illustrated in Figure 3.7, the number of support region lines (N) is calculated using (3.12).

$$\sin(\theta/2) = \frac{h}{2\alpha R_{avg}} \xrightarrow{\theta=2\pi/N} N = \frac{\pi}{\sin^{-1}(h/2\alpha R_{avg})} \tag{3.12}$$

If $x \ll 1$, $\sin^{-1}(x) \approx x$, equation (3.12) can be simplified to

$$N = \frac{2\pi\alpha R_{avg}}{h} \tag{3.13}$$

where R_{avg} is an average value for OD radius in the reference image as mentioned in 3.2.3.2, and h is the distance between endpoints of the support region lines.

3.2.4.2 Boundary Extraction

After applying the SBF to the new defined ROI, the location of the point with the maximum value of filter response, (x_c, y_c), is selected as the final ODC. Given the detected ODC coordinates, the OD shape can be estimated using the position of the band that maximizes the convergence index response in each direction of the support region lines. To estimate the OD shape, we start by finding the positions of the sliding band points (band support points) are found corresponding to the filter maximum response. The coordinates of the band support points (X, Y) are obtained using (3.14) and (3.15).

$$X(\theta_i) = x_c + r_{max}(i) \times \cos(\theta_i) \tag{3.14}$$

$$Y(\theta_i) = y_c + r_{max}(i) \times \sin(\theta_i) \tag{3.15}$$

where $r_{max}(i)$ is the radius in direction i, which is defined by

$$r_{max}(i) = \underset{R_{min} \leq n \leq R_{max}}{\operatorname{argmax}} \left(\frac{1}{d} \sum_{m=n}^{n+d} \cos \theta_{i,m} \right) \tag{3.16}$$

The band support points that represent the OD boundary are shown on the original size and cropped images, respectively, in Figure 3.8(a) and Figure 3.8(b).

3.2.4.3 Boundary Smoothing

In order to finalize the OD shape, a robust local regression algorithm is used for smoothing the boundary [104]. First the distances between boundary points and the final ODC are obtained $(d_{op}(i))$, and afterwards a locally weighted smoothing method is applied to the set of $d_{op}(i)$. The smoothing process is considered local as it smooths each value by using a subset of neighbouring data points. A robust regression weight function is defined for the data points contained within the subset, which makes the process resistant to outliers.

The local regression smoothing process starts by computing the regression weights for each data point in the subset. The number of data points in the subset is set equal to $N/4$, and the symmetric weight function is defined by

$$w_1(j) = \left(1 - \left| 1 - \frac{2j}{(N/4)} \right|^3 \right)^3, j = \left\{ 1, 2, 3, ..., \frac{N}{4} \right\} \tag{3.17}$$

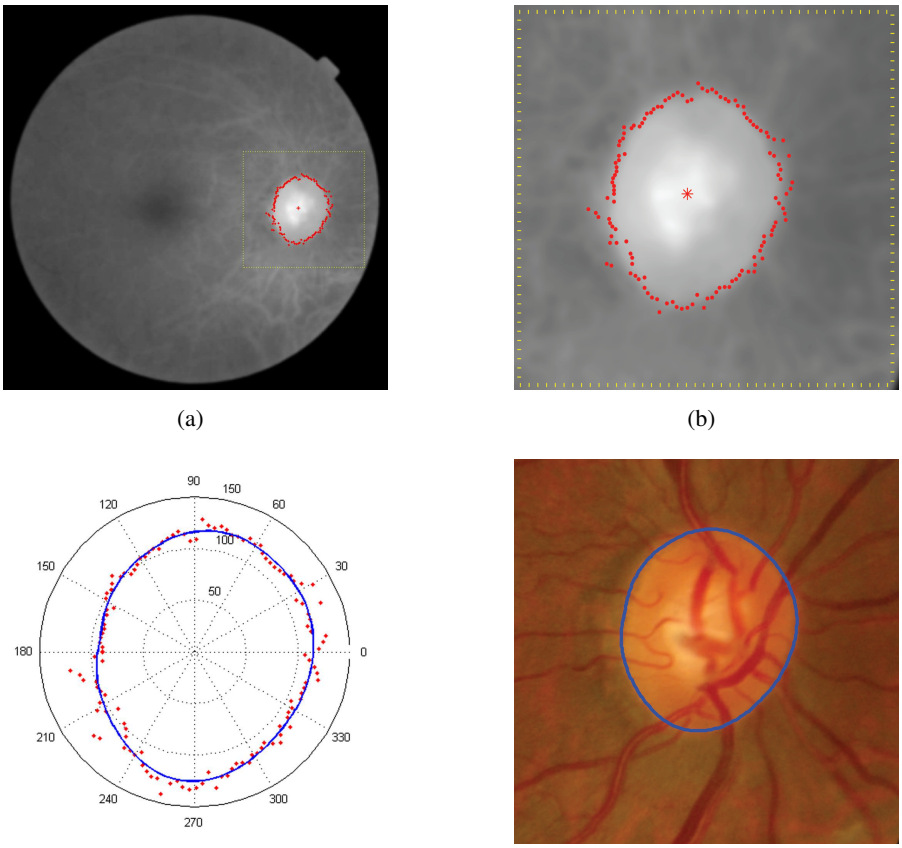

Figure 3.8: (a) Maximum value of high-resolution SBF response (star) and the obtained band support points (dots); (b) Band support points in cropped image round OD; (c) Polar plot of smoothing result (solid line) on the band support points (dots); (d) OD boundary after smoothing on the original RGB image.

where $w_1(j)$ is the weight for the j^{th} data point within the subset, and N is the number of boundary points. Afterwards, a second-degree polynomial is employed for the weighted linear least square regression of $d_{op}(i)$.

For preventing the distortion introduced by outliers, the distances $d_{op}(i)$ are smoothed again using robust weights. The computation of robust weights requires the computation of the residuals obtained in a previous smoothing step. The robust weights are given by

$$w_2(j) = \begin{cases} \left(1-(e_j/6M)^2\right)^2, & |e_j < 6M| \\ 0, & |e_j \geq 6M| \end{cases} \tag{3.18}$$

where e_j is the residual of the j^{th} data point produced by the previous regression smoothing algorithm, and M is the median of absolute deviation of the residuals.

Table 3.1: Parameters setting defined using ONHSD.

Parameter	**Value**	**Description**
d_1	530 *px*	Diameter of reference image mask
ϕ_1	45°	FOV of reference image
R_{ave}	40 *px*	Average of OD radius in reference image
h	4 *px*	Distance between endpoints of support region lines
K	10	Number of selected points with highest filter response
β	0.03	Parameter of (3.10) for excluding outliers
γ	8	Parameter of (3.11) for excluding outliers

px: pixel

The smoothing result is shown with a solid line in Figure 3.8(c). The final boundary points are specified using the smoothed distances from the ODC. Figure 3.8(d) presents the final OD boundary overlapped on the original RGB image.

3.3 Results

The automatic OD segmentation method described in the previous sections was evaluated in the images of three public datasets, ONHSD, MESSIDOR, and INSPIRE-AVR which are described in Appendix A. Using these three datasets makes it possible to analyse the performance of this new approach on images with different resolution (ranging from 760×570 to 2392×2048 pixels), acquired by various fundus cameras and distinct FOVs (30°, 45°).

Settings

The image and FOV sizes in the ONHSD were considered as reference values for parameter setting. Table 3.1 shows the values of the parameters that were established using the images of the ONHSD, and afterwards applied to the two other datasets.

The second column of Table 3.2 shows the values for the parameters of the low-resolution SBF, and the third column of Table 3.2 represents the formulas to obtain the parameters for the high-resolution SBF. Table 3.3 presents the scale factors for the different datasets calculated using (3.9). The SBF parameters for the MESSIDOR and INSPIRE-AVR datasets, calculated using (α), are shown in Table 3.4.

Table 3.2: Parameters setting for low-resolution SBF and high-resolution SBF.

Parameter	**Value** (low res.)	**Value** (high res.)	**Description**
N	64	64α	Number of support region lines
R_{min}	20	20α	Inner sliding band limit
R_{max}	60	60α	Outer sliding band limit
d	7	7α	Width of the band
w	91	αw_h	Window size for ROI
w_h	–	11	Default value for window size

Table 3.3: Scale factors for different datasets.

Dataset	Image size	FOV	Mask diameter	S_1	S_2	Scale factor (α)
ONHSD	760×570	45°	530	1	1	1
MESSIDOR	1440×960	45°	900	1.7	1	1.7
	2240×1488	45°	1357	2.6	1	2.6
	2304×1536	45°	1440	2.7	1	2.7
INSPIRE-AVR	2392×2048	30°	2045	3.9	1.5	5.8

Table 3.4: Parameter settings for high-resolution SBF for MESSIDOR and INSPIRE-AVR datasets.

Dataset	Image size	α	N	R_{min}	R_{max}	d	w	subset size
MESSIDOR	1440×960	1.7	109	34	102	12	19	27
	2240×1488	2.6	166	52	156	18	29	41
	2304×1536	2.7	173	54	162	19	31	43
INSPIRE-AVR	2392×2048	5.8	371	116	348	41	63	92

ONHSD

The original ONHSD dataset has 99 images. Similar to [46] and [42], the images with no discernible OD or with severe enough cataracts to prevent meaningful segmentation are excluded, leaving a final set of 90 images for assessing the SBF method. The size of the images in this dataset is equal to the reference size. Therefore the scale factor for ONHSD images is equal to 1 and there is no need to apply the high-resolution SBF. For this reason, after getting the result from the low-resolution SBF, the boundary was extracted as mentioned in 3.2.4.2. After finalizing the OD shape using the smoothing algorithm, the results were compared with those of the Circular

Hough Transform (CHT) [42], Morphology-based method (MBM) [54], Temporal Lock, Simple and DV-Hough methods [46].

In this dataset four clinicians marked 24 boundary points (at 15° angles), and the mean and the radial standard deviations of these values were calculated. For comparing the obtained results with those of the other methods, the same subjective evaluation method defined by Lowell *et al.* [46] is used. The discrepancy, δ_j on image j is defined by

$$\delta_j = \sum_i \frac{\left| m_i^j - \mu_i^j \right|}{\sigma_i^j + \varepsilon} \tag{3.19}$$

where μ_i^j and σ_i^j are, respectively, the mean and standard deviation of values obtained by four clinicians on spoke i of image j, m_i^j is the location of the boundary using the segmentation method on spoke i of image j, and ε is a small value to prevent division by zero when the clinicians are in exact agreement and was set equal to 0.5.

Lowell *et al.* also classified each image based on the discrepancy value as Excellent ($\delta_j < 1$), Good ($\delta_j < 2$), Fair ($\delta_j < 5$), and Poor ($\delta_j \geq 5$). The segmentation methods are assessed considering the percentage of OD segmentations classified in those four categories. Table 3.5 and Figure 3.9 shows the percentage of images per subjective category for different methods. The results of the proposed method are included in the first row and the second row presents the results of the Circular Hough Transform method [42]. The MBM [54], Temporal Lock, Simple and DV-Hough methods [46] are also included in this table.

Table 3.5: Comparison between proposed SBF-based method and four other methods in terms of percentage images per subjective category (ONHSD).

Method	Excellent	Good	Fair	Poor	Excellent-Fair
SBF-based	44%	47%	9%	0	100%
CHT [42]	40%	39%	18%	3%	97%
MBM [54]	28%	36%	31%	6%	94%
Temporal Lock [46]	42%	31%	10%	17%	83%
DV-Hough [46]	39%	22%	20%	19%	81%
Simple [46]	9%	8%	30%	53%	47%

In order to be able to compare with other publications, other measures were calculated such as: Dice's coefficient (DC) which describes the similarity degree between two regions; Accuracy (ACC), calculated by the sum of correctly detected OD pixels and non-OD pixels divided by the

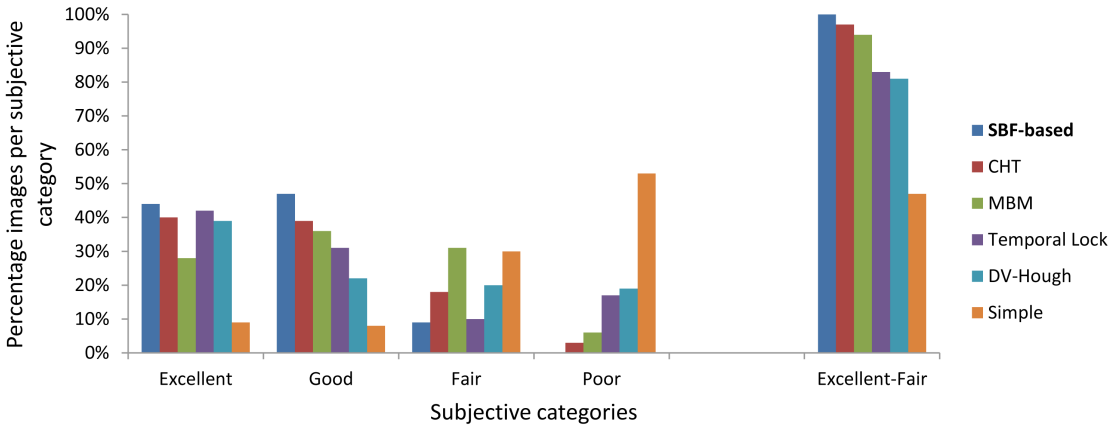

Figure 3.9: Comparison between proposed SBF-based method and four other methods in terms of percentage images per subjective category (ONHSD).

Table 3.6: Comparison of the average and standard deviation of different measures between proposed method and MBM on ONHSD dataset.

Method		$\bar{S}$	DC	ACC	TPF	FPF	MAD	MCC
SBF-based	Average	0.8341	0.9173	0.9968	0.9435	0.0012	2.4218	0.9133
	SD	0.0912	0.0634	0.0027	0.0791	0.0027	3.0727	-
MBM [54]	Average	0.8045	0.8867	0.9941	0.9310	0.0043	3.2753	0.7941
	SD	0.1175	0.0776	0.0042	0.1046	0.0042	3.0407	-

total number of pixels; true positive fraction (TPF) is obtained by dividing the number of correctly detected OD pixels by the total number of OD pixels in the reference image; false positive fraction (FPF) which is the ratio between the number of wrong detected OD pixels and the total number of non-OD pixels in the reference image; the mean absolute distance (MAD) which measures the accuracy of the OD boundary; and finally, Matthews correlation coefficient (MCC) which shows the quality of binary classifications by considering the different cardinalities of the two classes. Table 3.6 compares the result of proposed method with the results of MBM [54] on the ONHSD.

As it can seen in Table 3.5 and Table 3.6, the proposed method outperforms all the others, thus demonstrating that the method is adequate for low-resolution images. This gives us some confidence in evaluating this new approach in two other independent datasets, the MESSIDOR and INSPIRE-AVR datasets. Some results of the proposed OD segmentation method on images of ONHSD dataset are shown in Figure 3.10.

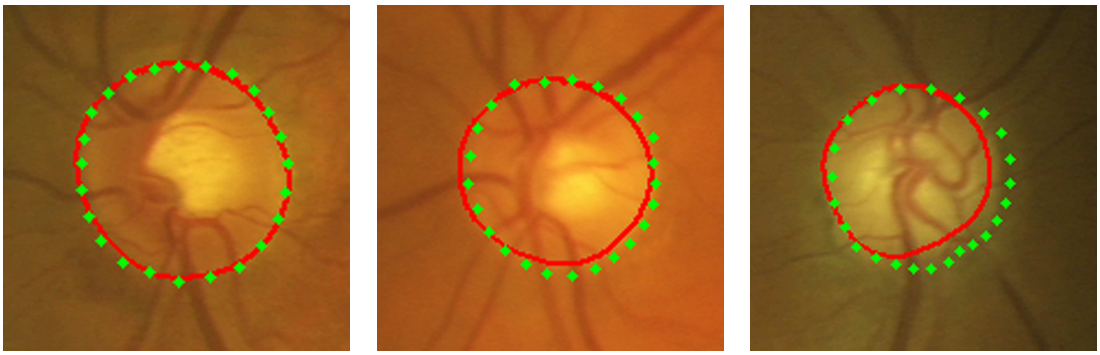

(a) (b) (c)

Figure 3.10: Samples of OD segmentation in the ONHSD (solid line: results of proposed method, dots: mean of clinician boundaries). (a) Excellent ($\delta = 0.5$); (b) Good ($\delta = 1.4$); (c) Fair ($\delta = 2.3$).

MESSIDOR dataset

The proposed method was used for segmenting the OD in the 1200 images of the MESSIDOR dataset. The parameters of the high-resolution SBF that were set based on the calculated scale factor (α) are shown in the first three rows of Table 3.4. In order to compare this result with those of the methods [42], [50] and [56], the overlapping score (S) is used which measures the common area between the OD region obtained using the automatic method (A) and the region delimited by experts (E) in [105], being defined by

$$S = \frac{\text{Area}\,(A \cap E)}{\text{Area}\,(A \cup E)} \tag{3.20}$$

The percentage of images for different intervals of the overlapping score, and the average of overlapping for all 1200 images are shown in Table 3.7 and Figure 3.11. The table includes the values for the SBF-based method, the multiresolution ellipse fitting (MEF) [45], the superpixel classification (SPC) approach proposed by Cheng *et al.* [56] and the CHT method [42]. The last row in this table presents the average overlapping score for the fast and hybrid level set model (F-HLSM) method proposed by Yu *et al.* [50]. As shown in this table, the overlapping between the manually segmented OD region and SBF-based method is always higher than the ones for the other methods, reaching an average overlapping score of 0.89 for the whole set of images in this dataset. Figure 3.12 shows some segmentation samples obtained with the proposed methodology.

The comparison between the result of this new method and the results of MBM [54] on the MESSIDOR dataset is shown in Table 3.8. The ratio between MAD and the estimated OD radius (r_{OD}) is used by Yu *et al.* [50] for evaluating the F-HLSM method. In order to measure this ratio,

Table 3.7: Comparison between the SBF-based method and other methods in terms of percentage of images per overlapping interval and average overlapping of the whole set (MESSIDOR dataset).

Method	$S \geq 0.95$	$S \geq 0.90$	$S \geq 0.85$	$S \geq 0.80$	$S \geq 0.75$	$S \geq 0.70$	$\bar{S}$
SBF-based	23%	66%	81%	87%	92%	94%	0.89
MEF [45]	13%	59%	82%	88%	92%	94%	0.88
SPC [56]	8%	51%	76%	86%	92%	-	0.88
CHT [42]	7%	46%	73%	84%	90%	93%	0.86
F-HLSM [50]	-	-	-	-	-	-	0.84
MBM [54]	-	-	-	-	-	-	0.82

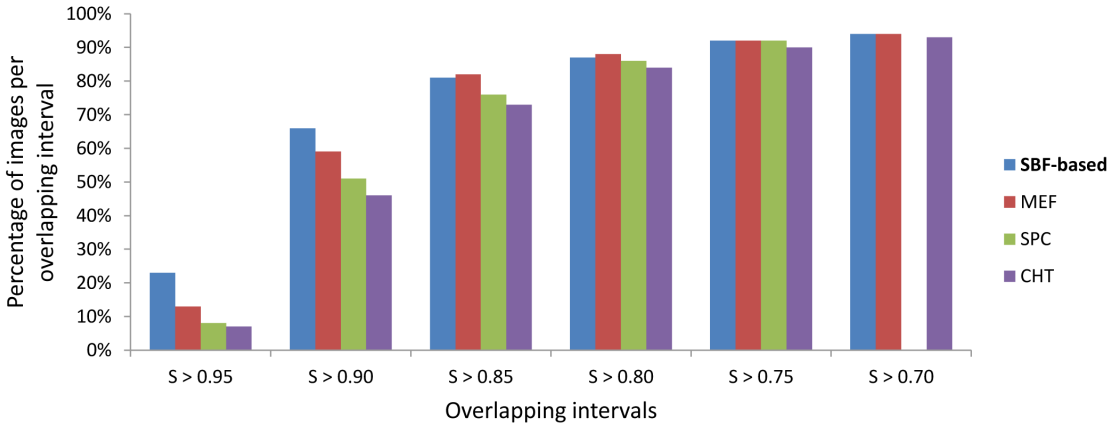

Figure 3.11: Comparison between the SBF-based method and other methods in terms of percentage of images per overlapping interval (MESSIDOR dataset).

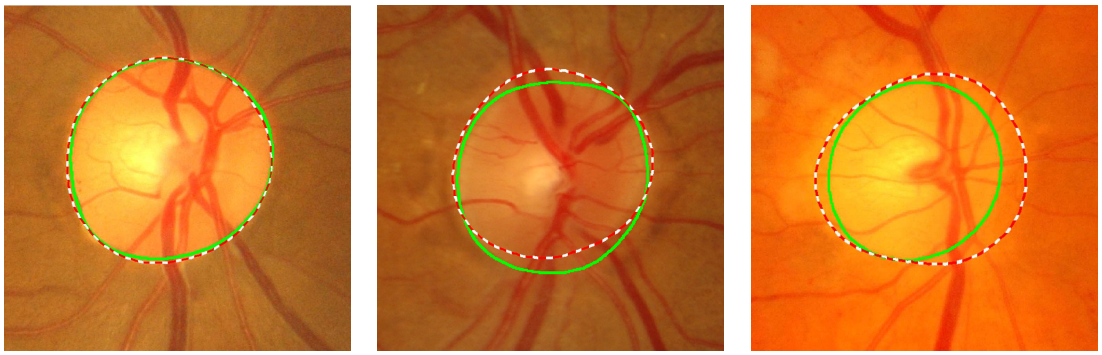

(a) (b) (c)

Figure 3.12: Samples of OD segmentation in MESSIDOR dataset (Dashed line: results of proposed method, Solid line: manually extracted boundaries by experts). (a) $S = 0.97$; (b) $S = 0.86$; (c) $S = 0.78$.

Table 3.8: Comparison of the average and standard deviation (SD) of different measures between proposed method and MBM on MESSIDOR dataset.

Method		$\bar{S}$	DC	ACC	TPF	FPF	MAD	MCC
SBF-based	Average	0.8859	0.9373	0.9987	0.9481	0.0008	3.1598	0.9339
	SD	0.0818	0.0509	0.0012	0.0459	0.0010	4.0178	-
MBM [54]	Average	0.8228	0.8950	0.9949	0.9300	0.0035	4.0759	0.8185
	SD	0.1384	0.1056	0.0050	0.1239	0.0041	6.0909	-

Table 3.9: Comparison between SBF-based method and F-HLSM method in terms of percentage images per subjective category based on the ratio between MAD and estimated OD radius (MESSIDOR dataset).

Categories	MAD/r_{OD}	**SBF-based**	F-HLSM [50]
Excellent	$\leqslant (1/20)$	42%	33%
Good	$\leqslant (1/10)$	76%	68%
Moderate	$\leqslant (1/5)$	91%	89%
Fair	$\leqslant (1/3)$	98%	97%

the authors estimated the OD radii equal to 70, 100 and 110 pixels for the images of MESSIDOR datasets with different sizes. Table 3.9 shows the percentage of images in four subjective categories (Excellent, Good, Moderate and Fair), which are defined based on the ratio between MAD and estimated OD radius. As it can seen in the second row of this table, the MAD value is not larger than one-tenth of the OD radius for 76% of 1200 images. The average of MAD is 8% of the OD radius, which is less than 10.1% reported by [50].

In the MESSIDOR datasets, there are several images from patients affected by diabetic retinopathy (DR) and macular edema (ME). These conditions can cause exudates with intensity similar to OD and peripapillary atrophy which can distort the result of OD segmentation. This dataset contains information regarding DR and risk of ME grading. The retinopathy grades (Normal, D1, D2 and D3) are obtained based on the number of microaneurysms, hemorrhages and neovascularization. The risk of macular edema is graded as Normal and two risk levels measuring the shortest distance between macula and hard exudates. The shortest distance between macula and hard exudates have been used for grading the risk of macular edema as Normal, R1 and R2. Table 3.10 shows the average and the standard deviation of the overlapping score (S) for the images with different DR and ME grades. As it can seen in this table, there is no significant difference between the average of overlapping scores, which demonstrates the robustness of the SBF-based method in

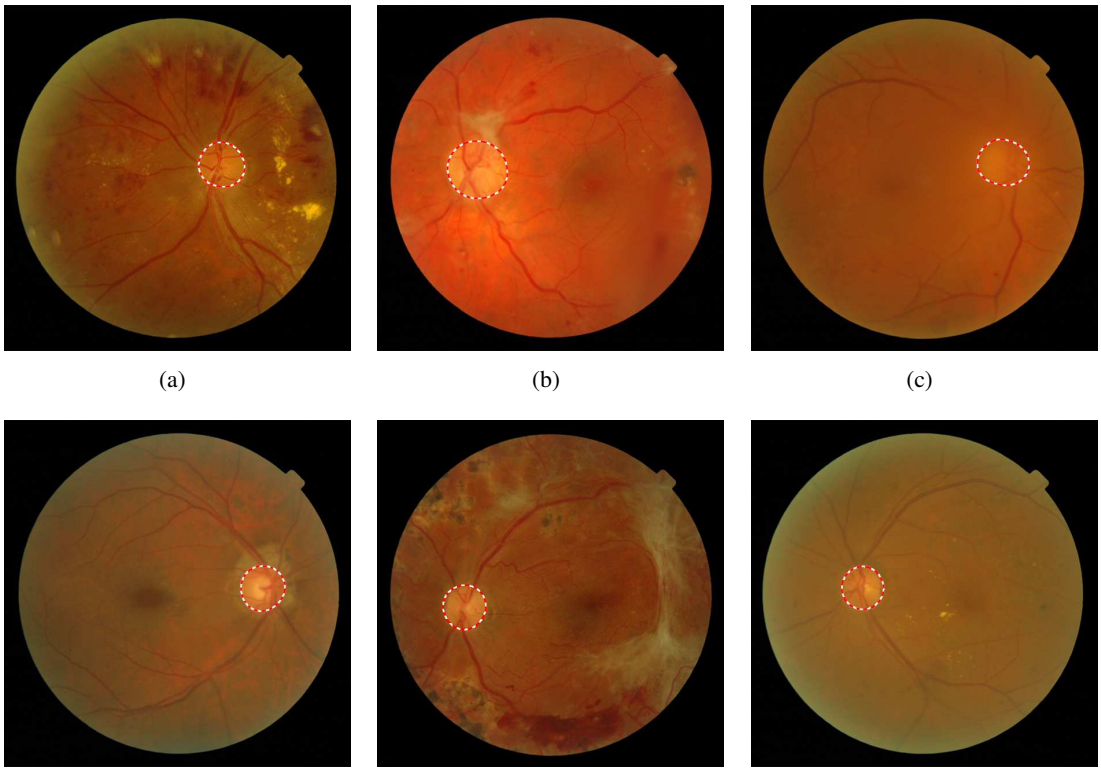

(a) (b) (c)

(d) (e) (f)

Figure 3.13: Samples of OD segmentation in the presence of exudates, peripapillary atrophy and blurredness; (a) DR: D3 and ME: R2; (b) DR: D3 and ME: R1; (c) DR: D3 and ME: Normal; (d) DR: D1 and ME: Normal ; (e) DR: D3 and ME: Normal; (f) DR: D3 and ME: R2.

the presence of diabetic retinopathy and risk of macular edema. Figure 3.13 shows examples the SBF-based results in the mentioned pathological conditions.

The good performance of the proposed method on the large number of images with different characteristics of the MESSIDOR dataset demonstrates the robustness of this method to illumination and contrast variations. Figure 3.14 shows the results of OD segmentation in different contrast and illumination conditions.

It should be noted that the initial OD detection method, described in section 3.2.2, failed in three images of the MESSIDOR dataset where the OD was located outside of the OD boundary in the standard reference as shown in Figure 3.15. In two of these images, the proposed algorithm failed to segment the OD correctly since the initial OD location is far from the actual ODC (Figures 3.15(a) and 3.15(b)). In the third image, the algorithm overcame the initial OD localization failure and segmented the OD correctly (Figure 3.15(c)).

In this dataset, the success rate of initial OD localization was 99.75% while now a success rate of 99.83% is achieved for the OD detection in both low-resolution and high-resolution phases. This

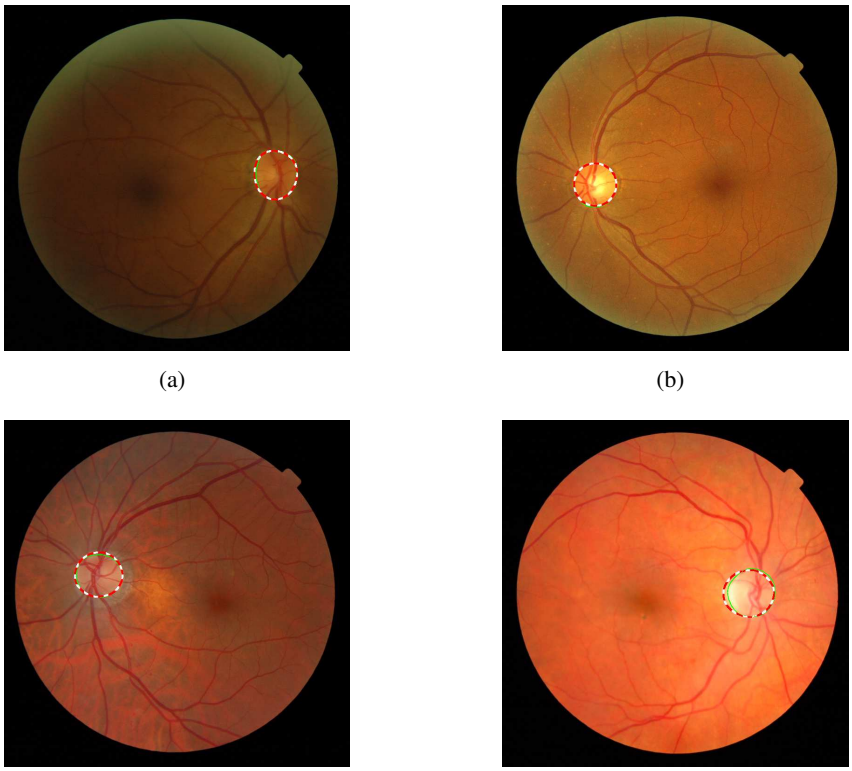

(a) (b) (c) (d)

Figure 3.14: Samples of OD segmentation in different conditions of contrast and illumination.

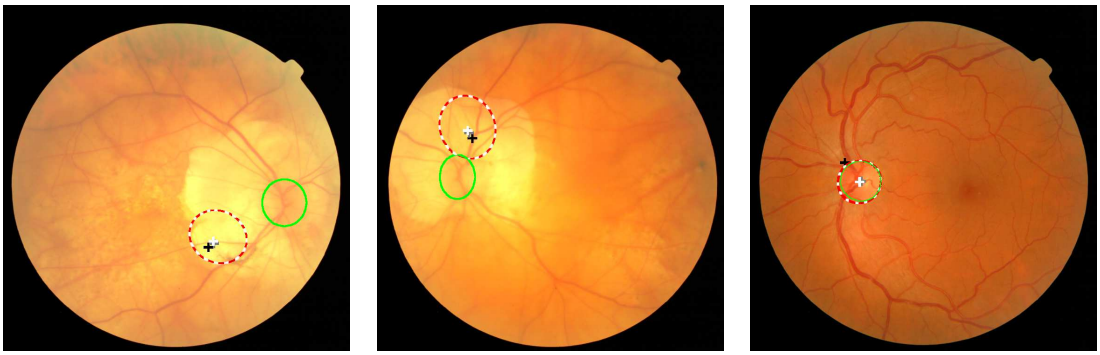

(a) (b) (c)

Figure 3.15: OD segmentation in MESSIDOR dataset where the initial OD detection (black cross) failed with the low-resolution ODC location (gray cross) and final ODC location (white cross); (a and b) The method failed to detect and segment the OD ($S = 0$); (c) The method overcame the initial OD localization failure and segmented the OD correctly ($S = 0.90$).

success rate is similar to the one for the MEF method and is higher than the ones for F-HLSM and CHT methods which are 99.08% and 98.83%, respectively.

The proposed algorithm was implemented in MATLAB on an Intel CPU i7-2600k, 3.40 GHz, 8 GB RAM computer. The average running time was 10.6 s per image in the MESSIDOR dataset,

Table 3.10: The average (standard deviation) of overlapping score (S) for the images of MESSIDOR dataset with different DR and ME grades.

		Diabetic retinopathy				Risk of macular edema		
	All	Normal	D1	D2	D3	Normal	R1	R2
Number	1200	540	153	247	260	971	75	154
S	0.8859	0.8885	0.8865	0.8805	0.8850	0.8853	0.8776	0.8939
	(0.0818)	(0.0788)	(0.0633)	(0.0907)	(0.0835)	(0.0801)	(0.0945)	(0.0765)

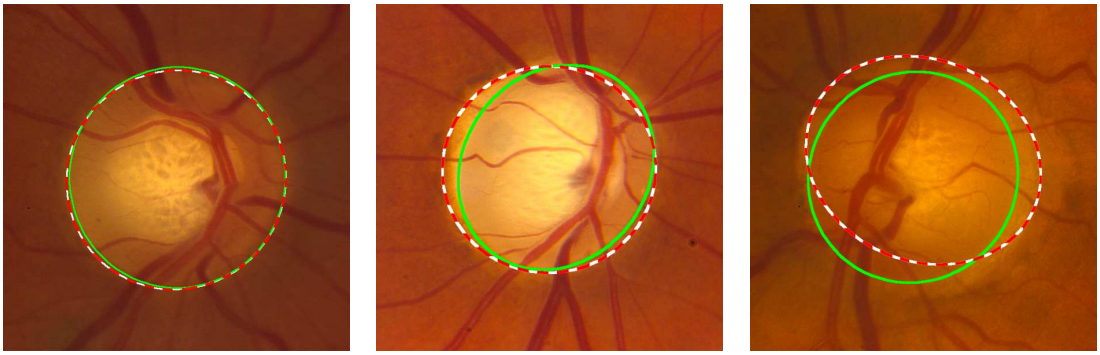

(a) (b) (c)

Figure 3.16: Samples of OD segmentation in INSPIRE-AVR dataset (Dashed line: results of proposed method, Solid line: manually extracted boundaries by an expert). (a) $S = 0.97$; (b) $S = 0.86$; (c) $S = 0.75$.

Table 3.11: The average and standard deviation of different measures on INSPIRE-AVR dataset.

	$\bar{S}$	DC	ACC	TPF	FPF	MCC	MAD/r_{OD}
Average	0.8505	0.9168	0.9958	0.9144	0.0020	0.9163	0.0897
Standard deviation	0.0864	0.0527	0.0030	0.0592	0.0025	0.0526	0.0600

while the running times for the CHT, MEF, SPC and F-HLSM methods on the same dataset were 7.36 s, 8 s, 10.9 s and 11.3 s, respectively.

INSPIRE-AVR dataset

In order to evaluate the performance of this new approach on high resolution images and different FOV (30°), the proposed method was also evaluated on the 40 images of INSPIRE-AVR dataset. For segmenting the OD, the parameters of the high-resolution SBF were set based on the last row of Table 3.4. The performance of the SBF-based method is in Table 3.11. An average overlapping score of 85% was achieved for the whole dataset, while the mean MAD value was less than 9% of the OD radius. Some images depicting the manual ground-truth and the result of the SBF-based segmentation are shown in Figure 3.16.

3.4 Concluding Remarks

The segmentation of the optic disc in retinal images is essential for the automated assessment of vascular changes. In previous sections, a new automatic methodology for OD segmentation is described which is distinct from previous approaches. This method uses the SBF in two different phases. In the first one, a low-resolution SBF is applied to the downsampled images in order to obtain an initial estimation of the ODC location, whose position is used for establishing the ROI for the high-resolution SBF in the following phase. The parameters of high-resolution SBF are adapted to the image size and camera field of view. The maximum response of the SBF gives the band support points that are used for an initial delineation of the OD boundary, which is afterwards smoothed using robust local regression.

The proposed method outperforms recently published approaches for OD segmentation. The promising results on the images of three different datasets prove the independence of this approach from changes in image characteristics such as size, quality and camera field-of-view.

Chapter 4

Artery/Vein Classification

The classification of retinal vessels into artery/vein (A/V) is an important phase for automating the detection of vascular changes, and for the calculation of characteristic signs associated with several systemic diseases such as diabetes, hypertension, and other cardiovascular conditions. Several works on vessel classification have been proposed [57–71], but automated classification of retinal vessels into arteries and veins has received limited attention, and is still an open task in the retinal image analysis field.

This chapter is mostly based in the paper *"An Automatic Graph-Based Approach for Artery/Vein Classification in Retinal Images"* [10]. Here, a graph-based method for automatic A/V classification is proposed. The graph extracted from the segmented retinal vasculature is analyzed to decide on the type of intersection points (graph nodes), and afterwards one of two labels is assigned to each vessel segment (graph links). Finally, intensity features of the vessel segments are measured for assigning the final artery/vein class using two different supervised and unsupervised approaches.

This chapter is organized as follows. In Section 4.1 the new methods for artery/vein classification are described. The results of tests on the images of three different datasets are presented in Section 4.2, where a comparison with the manual classifications is also included. Finally, Section 4.3 summarizes the conclusions of this chapter.

4.1 Graph-based A/V Classification Method

Most of the methods described in Section 2.3 use intensity features to discriminate between arteries and veins. Due to the acquisition process, very often the retinal images are non-uniformly illuminated and exhibit local luminosity and contrast variability, which can affect the performance of intensity-based A/V classification methods. For this reason, we propose a method, that uses additional structural information extracted from a graph representation of the vascular network.

This method follows a graph-based approach, which focuses on a characteristic of the retinal vessel tree that, at least in the region near the optic disc, veins rarely cross veins and arteries rarely cross arteries. This assumption demands for the detection of different types of intersection points, namely: bifurcation, crossing, meeting, and connecting points. A bifurcation point is an intersection point where a vessel bifurcates to narrower vessels. In a crossing point a vein and an artery cross each other. In a meeting point the two types of vessels meet each other without crossing, while a connecting point connects different parts of the same vessel. The decision on the type of the intersection points is made based on the geometrical analysis of the graph representation of the vascular structure.

Figure 4.1 depicts the block diagram of the method proposed for A/V classification. The main phases are: 1) graph generation; 2) graph analysis; and 3) vessel classification. The graph generator extracts a graph from the vascular tree, and afterwards makes a decision on the type of each intersection point (graph node). Based on the node types in each separate subgraph, all vessel segments (graph links) that belong to a particular vessel are identified and then labeled using two distinct labels. Finally, the A/V classes are assigned to the subgraph labels using supervised and unsupervised techniques. The supervised approach involves a set of features and a linear classifier, while the unsupervised approach is based on the red intensity and on a k-means clustering algorithm. In the following, each one of the phases are detailed.

4.1.1 Graph Generation

A graph is a representation of the vascular network, where each node denotes an intersection point in the vascular tree, and each link corresponds to a vessel segment between two intersection points. The graph generator is a three-step algorithm. First, the segmented image is used to obtain the vessel centerlines, then the graph is generated from the centerline image, and finally some additional modifications are applied to the graph.

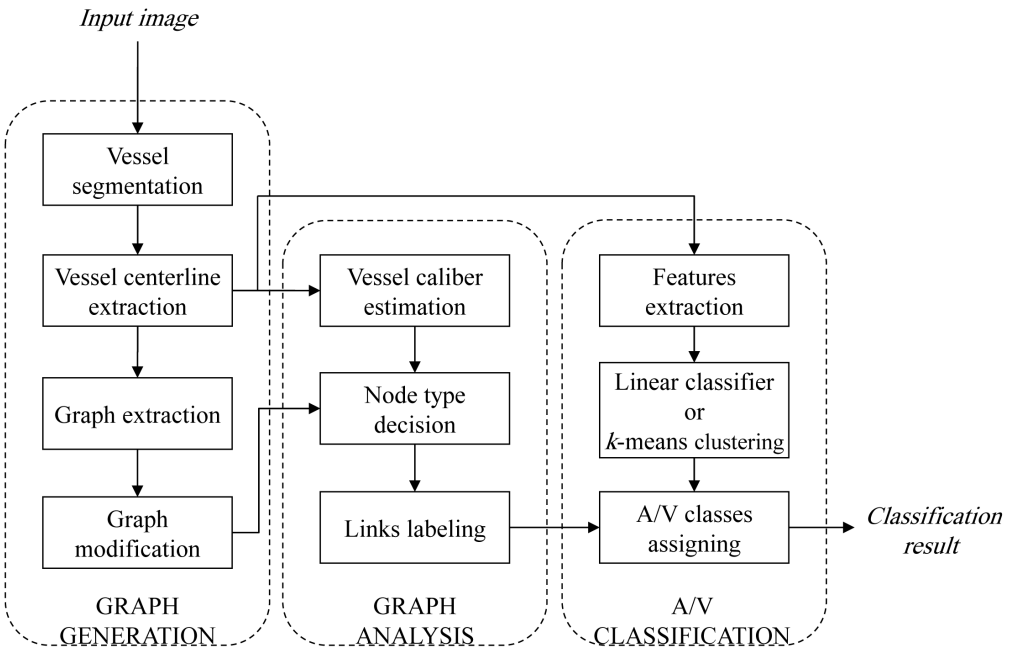

Figure 4.1: Block diagram of the proposed method for A/V classification.

4.1.1.1 Vessel Segmentation

The vessel segmentation was described in Section 3.1. The resulting segmented image is used for extracting the graph and also for estimating vessel calibers. Figure 4.2(a) illustrates the result of vessel segmentation.

4.1.1.2 Vessel Centerline Extraction

The centerline image is obtained by applying an iterative thinning algorithm described in [106] to the vessel segmentation result. This algorithm removes border pixels until the object shrinks to a minimally connected stroke. Thinning of an image I by a sequence of structuring elements $\{B\} = \{B_1, B_2, B_3, ..., B_n\}$, can be defined by terms of the hit-and-miss transform ($A \otimes B = A - (A \circledast B) = A \cap (A \circledast B)^c$), where B_i is a 45° rotated version of B_{i-1}. The process starts thinning I with B_1, then thinning the result with B_2, and so on until B_n, and the entire process repeats until no further changes occur. The vessel centerlines from the segmented image of Figure 4.2(b) are shown in Figure 4.2(c).

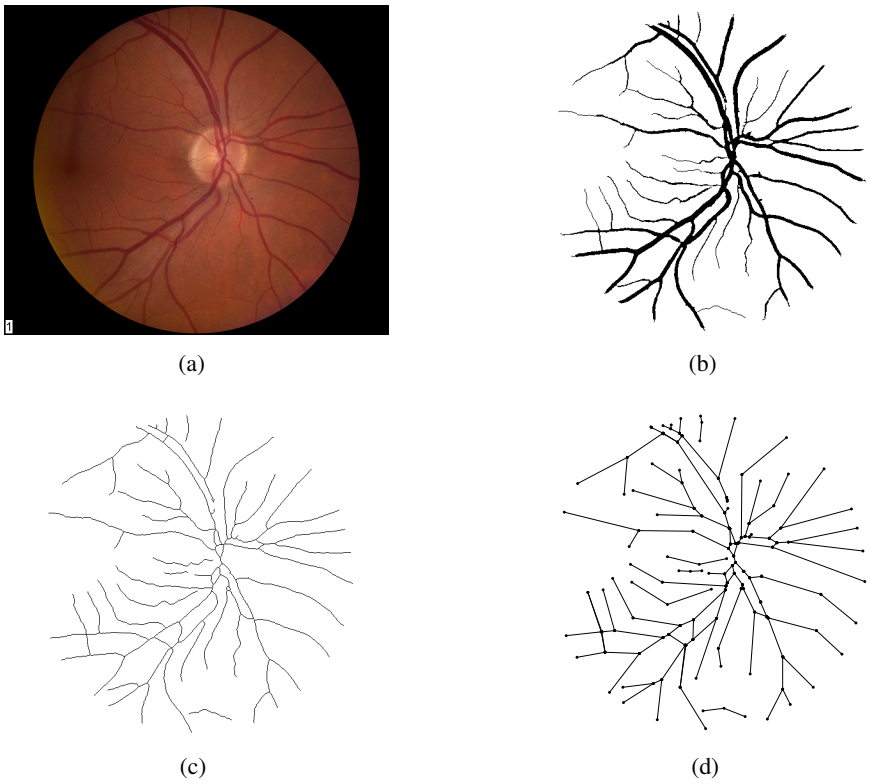

Figure 4.2: Graph generation. (a) Original image; (b) Vessel segmentation image; (c) Centerline image; (d) Extracted graph.

4.1.1.3 Graph Extraction

In the next step, the graph nodes are extracted from the centerline image by finding the intersection points (pixels with more than two neighbors) and the endpoints or terminal points (pixels with just one neighbor). In order to find the links between nodes (vessel segments), all the intersection points and their neighbors are removed from the centerline image and as result an image is obtained with separate components which are the vessel segments. Next, each vessel segment is represented by a link between two nodes. Figure 4.2(d) shows the graph obtained from the centerline image of Figure 4.2(c).

The graph contains nodes, and at each node several links can be connected. On the other hand, any given link can only connect two nodes. Table 4.1 shows the graph notations for nodes and links which will be used in the rest of this document. The degree of a node is the number of adjacent nodes. Two nodes in a graph are called adjacent if they are connected by one link. The angle between links is defined as the magnitude of the smallest rotation that projects one of the links onto the other by considering the common node between them as the vertex. A vessel caliber

Table 4.1: Graph Notations.

Notation	Description
N	Number of nodes in the graph
$n_i, \quad 1 \leq i < N$	Node i
D_{n_i}	Degree of node i which is the number of adjacent nodes
$l_{ip}, \quad 1 \leq p < D_{n_i}$	p^{th} link of node i
d_{ij}	Distance between node i and j
T_{n_i}	Type of node i
$\angle l_{ip} l_{iq}$	Angle between p^{th} and q^{th} links of node i
$W_{l_{ip}}$	Vessel caliber assigned to p^{th}link of node i
E_{n_i}	Number of degree 1 nodes adjacent to node i

is assigned to each link, as the average of the calibers along the corresponding vessel segment.

4.1.2 Graph Modification

The extracted graph may include some misrepresentation of the vascular structure as a result of the segmentation and centerline extraction processes. As defined in [58], the typical errors are (1) the splitting of one node into two nodes; (2) a missing link on one side of a node; (3) false link. The extracted graph should be modified when one of these errors is identified.

Figure 4.3 illustrates the three typical errors before and after modification. The typical errors are depicted in the left column; graphs in the middle column are the representations of the worst-case scenarios and graphs on the right side are the modified ones.

Node splitting

When extracting the centerline pixels in a single intersection, there are two graph nodes instead of only one. This situation, illustrated in Figure 4.3(a), creates false nodes which affect the correctness of the final result of the graph analysis phase.

For addressing this problem an adaptive parameter is defined, the threshold T_{ns}, which is used as the criterion for merging two neighborhood nodes. T_{ns} depends on the local vessel calibers and angles according to equations (4.1) to (4.4).

$$T_{ns} = \frac{1}{\sin(\alpha)} \left({d_1}^2 + {d_2}^2 + 2 d_1 d_2 \cos(\alpha) \right)^{1/2} \tag{4.1}$$

$$\alpha = \min(\angle l_{i1} l_{i2}, \angle l_{j1} l_{j2}) \tag{4.2}$$

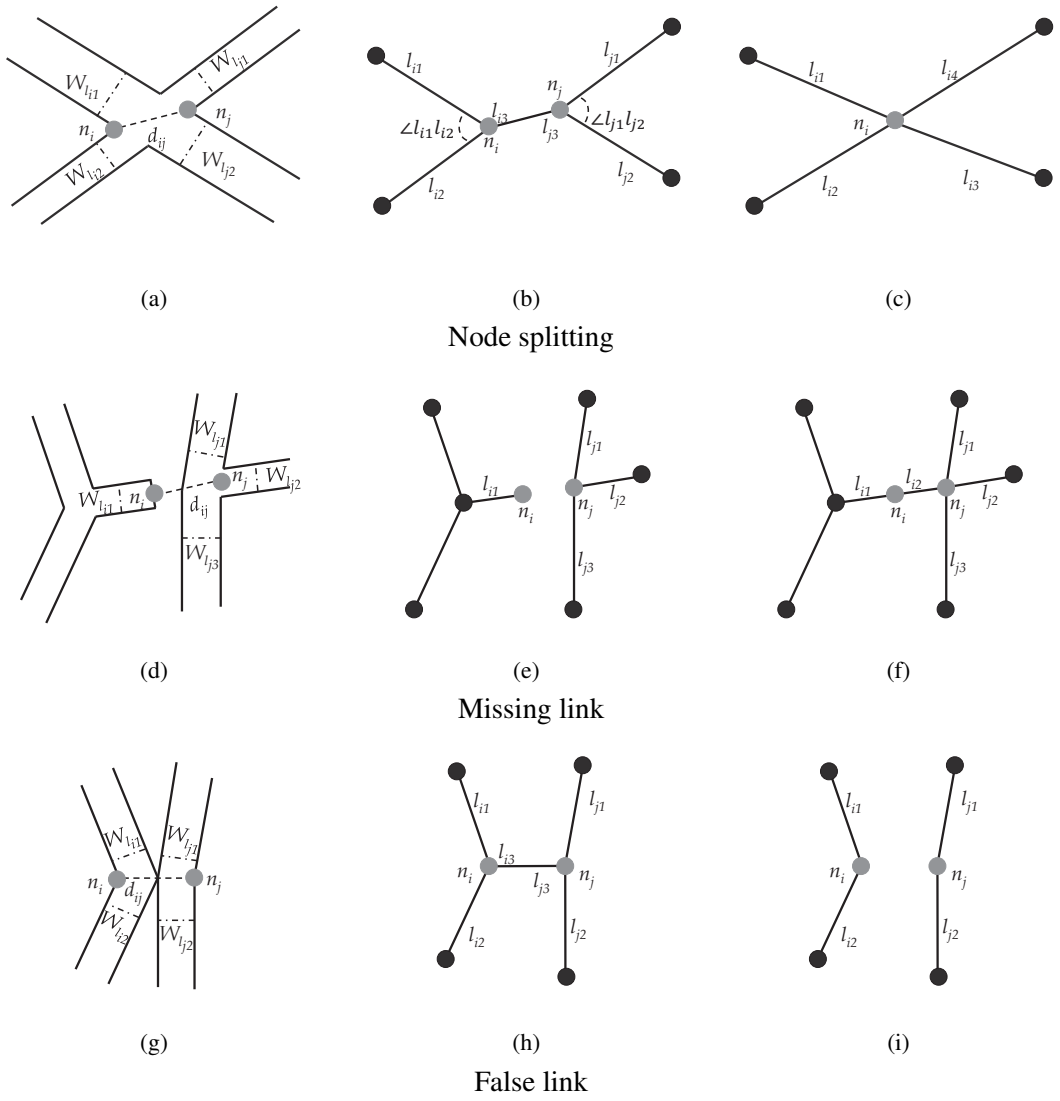

Figure 4.3: Graph Modifications. (a), (d), (g) Typical errors; (b), (e), (e) Graph representation of the worst-case scenarios; (c), (f), (i) Final graph after modification.

$$d_1 = \max\left(W_{l_{i1}}, W_{l_{j2}}\right) \tag{4.3}$$

$$d_2 = \max\left(W_{l_{i2}}, W_{l_{j1}}\right) \tag{4.4}$$

In adjacent nodes with degree 3, Figure 4.3(b), if the distance between node n_i and n_j is smaller than the threshold ($d_{ij} < T_{ns}$) and if a link in one node (common link excluded) has the same orientation of another link in the other node, and the same happens with the two remaining links, then the two corresponding nodes should be merged (Figure 4.3(c)).

Missing link

For solving the missing link cases (Figure 4.3(d)), the distance from a degree 1 node (endpoints) to other nodes is calculated. If this distance is less than a threshold T_{ml}, then the nodes will be connected with a new link as shown in Figure 4.3(f). T_{ml} estimation is based on the widths of the intervening vessels (Figure 4.3(e)), and is given by

$$T_{ml} = W_{l_{i1}} + \max_{p\in\{1,2,3\}} W_{l_{jp}} \tag{4.5}$$

False link

Figure 4.3(g) illustrates the last situation, corresponding to an incorrect detection of a link between two nodes. This happens when two vessels are very close to each other but they do not cross, and two close nodes ($d_{ij} < T_{fl}$) are artificially created. Equation (4.6) represents the threshold T_{fl} for this case, which is obtained from the maximum distance of nodes in the worst-case scenario (Figure 4.3(h)).

$$T_{fl} = \max_{p\in\{1,2\}} \left(\frac{W_{l_{ip}}}{\sin(\angle l_{ip} l_{i3})} \right) + \max_{q\in\{1,2\}} \left(\frac{W_{l_{jq}}}{\sin(\angle l_{jq} l_{j3})} \right) \tag{4.6}$$

For solving this case, the angle between the links connected to each node is checked. If, for at least one node, two of its links have an identical orientation and are more or less perpendicular to the third link (the common link between two nodes), then the common link is a falsely-detected link and should be removed (Figure 4.3(i)).

Algorithm 1, in page 62, states the conditions for detecting errors in the graph and for performing the necessary modifications. This algorithm repeats until no further changes occur. In order to reduce the complexity of the subsequent graph analysis, all endpoints with very short links are removed.

Before initiating the graph analysis phase, all vessels around the OD are removed. The optic disc area usually contains many vessels and the graph in that area is not reliable. As these vessels are not relevant for the A/V classification process, they can be removed. The result is a graph formed by several non-connected separate subgraphs. The operations in the graph modification step are illustrated in Figure 4.4.

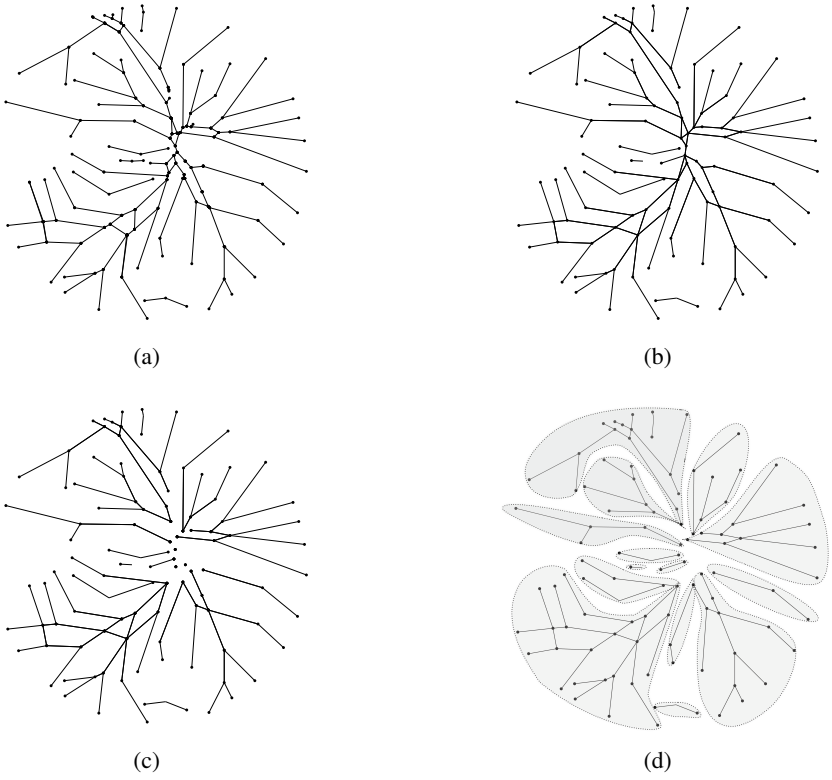

Figure 4.4: (a) Original graph; (b) New graph after modification step; (c) Modified graph without vessels around the optic disc; (d) Separate subgraphs (each gray region represents a subgraph).

Algorithm 1 Graph Modification

for $i = 1$ to N **do**
  for $j = 1$ to N, $j \neq i$ **do**
    if $D_{n_i} = 1 \wedge d_{ij} < T_{ml}$ **then**
      Make a new link (l_{i2}) between n_i, n_j
    else if n_i, n_j are adjacent $\wedge D_{n_i} = 3 \wedge D_{n_j} = 3$ **then**
      if $d_{ij} < T_{sn} \wedge (\angle l_{i1}l_{i3} + \angle l_{j2}l_{j3} = 180^\circ \pm 10^\circ) \wedge (\angle l_{i2}l_{i3} + \angle l_{j1}l_{j3} = 180^\circ \pm 10^\circ)$ **then**
        Merge n_i and n_j
      else if $d_{ij} < T_{fl} \wedge ((\angle l_{i1}l_{i3} = 90^\circ \pm 5^\circ \wedge \angle l_{i2}l_{i3} = 90^\circ \pm 5^\circ) \vee (\angle l_{j1}l_{j3} = 90^\circ \pm 5^\circ \wedge \angle l_{j2}l_{j3} = 90^\circ \pm 5^\circ))$ **then**
        Remove the link between n_i, n_j (l_{i3}, l_{j3})
      end if
    end if
  end for
end for

4.1.3 Graph Analysis

The output of the graph analysis phase is a decision on the type of the nodes. The links in each subgraph (i) are labeled with one of two distinct labels (C_1^i and C_2^i). In this phase we are not yet able to determine whether each label corresponds to an artery class or to a vein class. The A/V

Table 4.2: Different cases of nodes and the possible node types.

Cases	Possible node types
Case 1 - Nodes of degree 2	Connecting point Meeting point
Case 2 - Nodes of degree 3	Bifurcation point Meeting point
Case 3 - Nodes of degree 4	Bifurcation point Meeting point Crossing point
Case 4 - Nodes of degree 5	Crossing point

classes will be assigned to these subgraphs only in the last classification phase.

We have considered four different types of nodes:

1. Connecting point: most of the nodes with two links belong to this type; these nodes, where vessels never cross or bifurcate, are continuation nodes connecting different segments of the same vessel.

2. Crossing point: two different types of vessels cross each other.

3. Bifurcation point: a vessel bifurcates into narrower vessels.

4. Meeting point: two different types of vessels meet each other without crossing; the two vessels are very close to each other or one vessel ends exactly on the other vessel.

The node classification algorithm starts by extracting the following node information: the number of links connected to each node (node degree), the orientation of each link, the angles between the links, the vessel caliber at each link, and the degree of adjacent nodes.

Node analysis is divided into four different cases depending on the node degree. Table 4.2 shows the different cases, and the possible node types for each. In Figs. 4.5 and 4.6, the nodes under analysis are represented by gray dots and other nodes are represented as black dots, except the endpoints which are represented as white dots. Solid lines show the links for one label and the dashed lines represent the other label.

Nodes of degree 2

Nodes with two links are mostly connecting nodes. If at least one of its adjacent nodes is an endpoint, then the node is a connecting point (Figure 4.5(a)) and both links have the same label; however, if none of the adjacent nodes are endpoints then the node type depends on the angle between its links. If $\angle l_{i1} l_{i2} > 90^\circ$ then it is a connecting node (Figure 4.5(b)), otherwise it is a

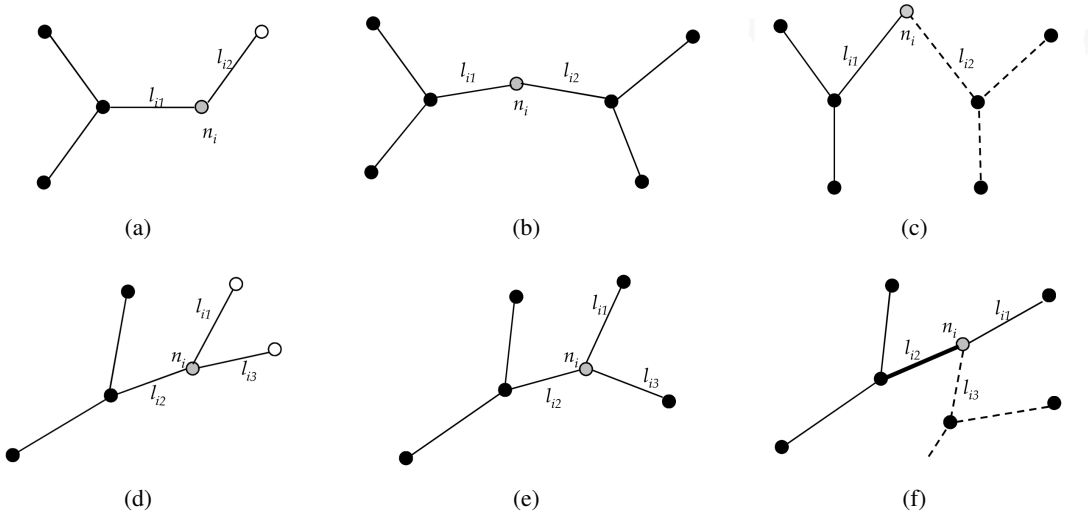

Figure 4.5: (a)-(c) Possible configurations for nodes of degree 2; (d)-(f) Possible configurations for nodes of degree 3.

meeting point and the links have different labels (Figure 4.5(c)). Algorithm 2 details the procedure for deciding on the type of nodes of degree 2.

Nodes of degree 3

For each node with 3 links, if at least two adjacent nodes are endpoints then the node is a bifurcation point and all the links have the same label (Figure 4.5(d)). If all the connected links have different orientations then the node is also a bifurcation point (Figure 4.5(e)). If two links have the same orientation then both belong to the same vessel type (Figure 4.5(f)) and they will be considered as a main vessel. We can decide if the third link is a branch of the same vessel or a segment of another vessel by checking its angle with the thicker segment of the main vessel. The thicker segment of the main vessel can be found by comparing the vessel caliber assigned to each link. If the difference between vessel calibers is very small, then it is not reliable to find the thicker one based on the calibers; in this situation, the link connected to the closest node to the optic disc center represents the thicker segment of the main vessel, and the link connected to the farthest node is the thinner segment of the main vessel. If the third link makes an angle less than 90° with the thicker segment of the main vessel then it is not a branch of this vessel but a part of another vessel, and the node is a meeting point; otherwise, it is a branch and all links have the same label. The sequence of operations for finding the type of nodes of degree 3 is described in Algorithm 3.

Algorithm 2 Node type - Nodes of degree 2

```
for i = 1 to N do
  if D_{n_i} = 2 then
    if E_{n_i} ≥ 1 then
      T_{n_i} = Connecting point
    else if ∠l_{i1}l_{i2} ≤ 90° then
      T_{n_i} = Meeting point
    else
      T_{n_i} = Connecting point
    end if
  end if
end for
```

Algorithm 3 Node type - Nodes of degree 3

```
for i = 1 to N do
  if D_{n_i} = 3 then
    if E_{n_i} ≥ 2 then
      T_{n_i} = Bifurcation point
    else
      flag = 0
      for p,q,r = 1 to 3 do
        if ∠l_{ip}l_{iq} = 180° ± 10° ∧ flag = 0 then
          flag = 1
          if W_{l_{ip}} > W_{l_{iq}} ∧ ∠l_{ip}l_{ir} < 90° then
            T_{n_i} = Meeting point
          else
            T_{n_i} = Bifurcation point
          end if
        end if
      end for
      if flag = 0 then
        T_{n_i} = Bifurcation point
      end if
    end if
  end if
end for
```

Nodes of degree 4

In this case there are three node type possibilities. First, the four links are grouped into two pairs, each one formed by the two links with the highest angle between them; if the two links of each of these pairs have an identical orientation (Figure 4.6(a)), then the node is a crossing point and each pair of links has a different label.

If the links of one pair do not have the same orientation, then the other pair will be selected as the main vessel. If the angle between each one of the other links and the thinner part of the main

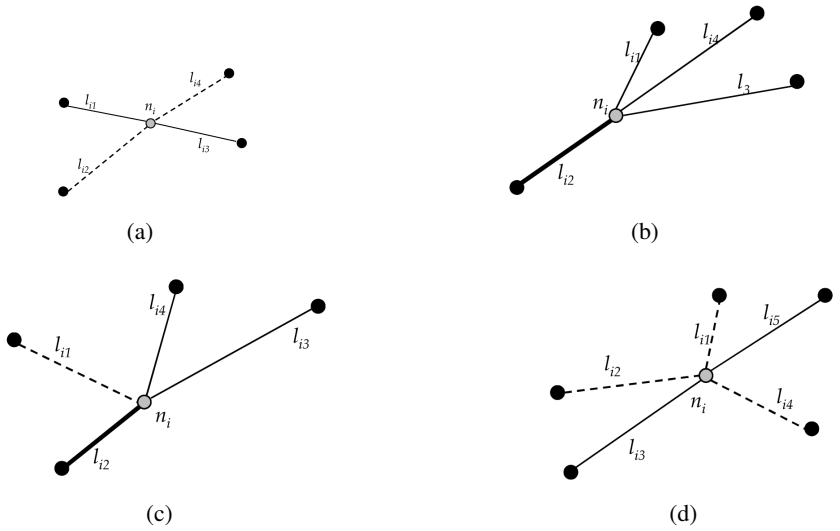

Figure 4.6: (a)-(c) Possible configurations for nodes of degree 4; (d) Node of degree 5.

Algorithm 4 Node type - Nodes of degree 4

for $i = 1$ to N **do**
  if $D_{n_i} = 4$ **then**
    for $p,q,r,s = 1$ to 4 **do**
      if $\angle l_{ip}l_{iq} = 180^\circ \pm 10^\circ \wedge \angle l_{ir}l_{is} = 180^\circ \pm 10^\circ$ **then**
        T_{n_i} = Crossing point
      else if $\angle l_{ip}l_{iq} = 180^\circ \pm 10^\circ \wedge W_{l_{ip}} < W_{l_{iq}} \wedge \angle l_{ip}l_{ir} < 90^\circ \wedge \angle l_{ip}l_{is} < 90^\circ$ **then**
        T_{n_i} = Bifurcation point
      else
        T_{n_i} = Meeting point
      end if
    end for
  end if
end for

vessel is less than 90°, then the node is considered a bifurcation point and all links have the same label (Figure 4.6(b)). If one of these links makes an angle less than 90° with the thicker segment of the main vessel, then it has a different label and the node is a meeting point (Figure 4.6(c)). Algorithm 4 details the procedure for finding the type for nodes of degree 4.

Nodes of degree 5

This is a rare situation that happens when a vessel crosses another vessel on a bifurcation point. For labeling, we start by finding the two links with the largest angle between them, as for instance l_{i3} and l_{i5} in Figure 4.6(d). These links belong to the vessel which crosses the other vessel on its bifurcation point, so these links will have the same label. The other three links (l_{i1}, l_{i2} and l_{i4})

belong to the vessel which bifurcates in this node, therefore all these links will be marked with the other label.

4.1.3.1 Graph labeling

After deciding on the node types, all links that belong to a particular vessel are identified and labeled. The generated graph contains two kinds of subgraphs; unpaired subgraphs representing only one type of vessel (vein or artery) and paired subgraph representing both types of vessels (vein and artery) which include crossing or meeting points. The final result is the assignment of one label to each unpaired subgraph and assignment of two labels to each paired subgraph. This means that labels C_1^1, C_2^1 will be assigned to the links in paired subgraph 1, labels C_1^2, C_2^2 to the links in paired subgraph 3, label C_1^3 will be assigned to the links in unpaired subgraph 3 and so on.

For each separate subgraph, the farthest link from the ODC is detected, and a label is assigned to this link (for instance C_1^1); the node connected to this link is found, and based on the node type the other links are labeled as C_1^1 or C_2^1. Some examples of link labeling is shown in Figure(4.7).

This procedure is repeated for all nodes until there are no more links for each subgraph. After finishing the labeling of one separate subgraph, we will repeat the process for all the separate subgraphs, each time defining new labels, until the entire graph is processed. In the end we have a graph with different pairs of labels for each disjoint subgraph, as illustrated in Figure 4.8(b), where each color in a separate subgraph represents a different label.

4.1.4 A/V Class Assignment

The above described labeling phase used the vessel structural information embedded in the graph representation. Based on these labels, the final goal is now to assign the artery class (A) to one of the labels, and the vein class (V) to the other. For this purpose the combination of structural information and vessel intensity information is used in order to allow the final discrimination between A/V classes. Two approaches are described in this section, the first one is based on a supervised classification technique and the second one is an unsupervised alternative.

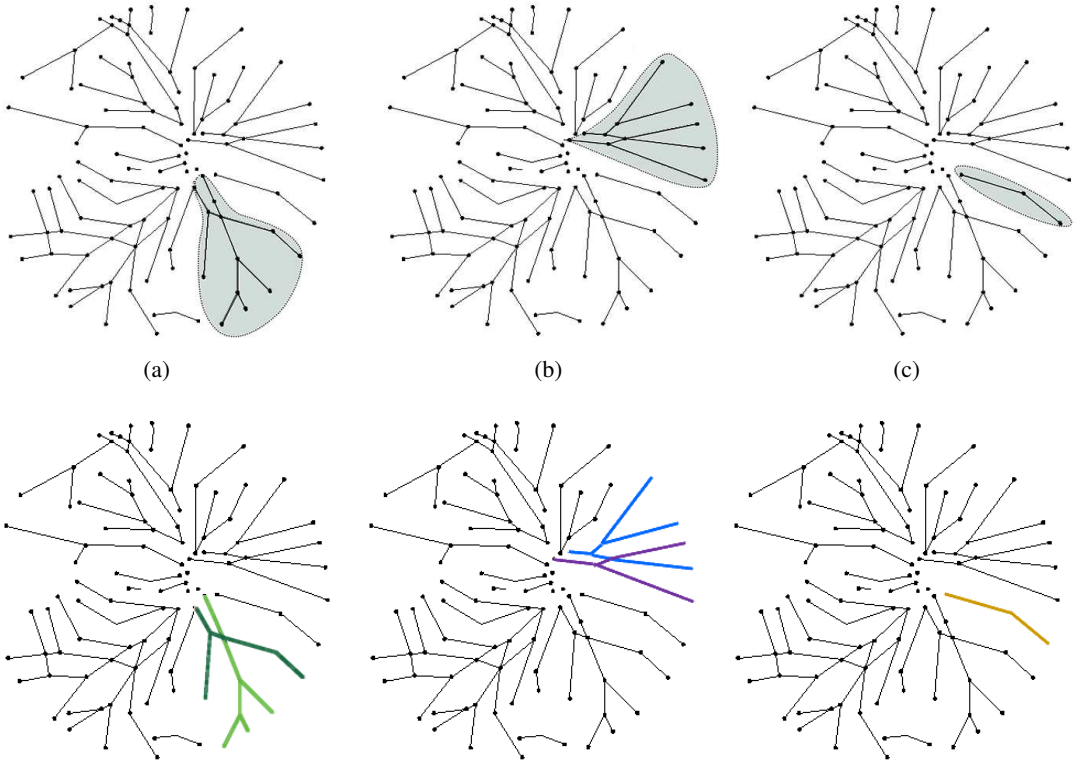

Figure 4.7: Examples of subgraph labeling where each color represent a distinct label; (a) Paired subgraph 1; (b) Paired subgraph 2; (c) Unpaired subgraph 3; (e), (e) and (f) Results of link labeling in subgraphs (a), (b) and (c).

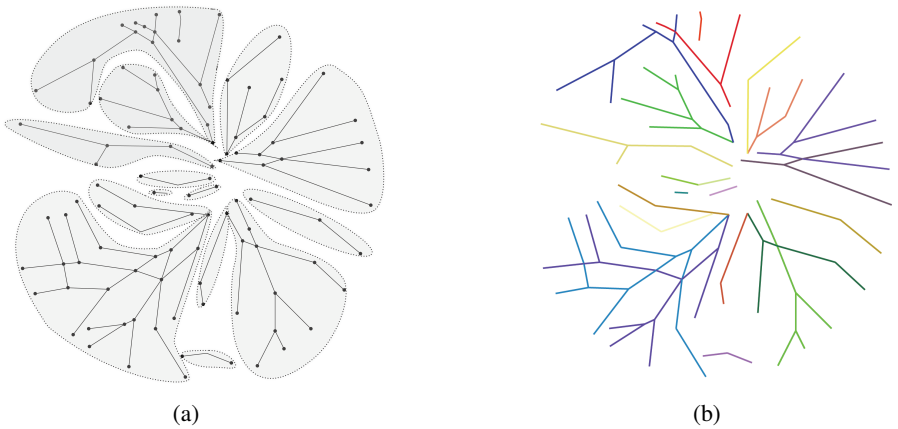

Figure 4.8: (a) Separate subgraphs (b) Final result of graph analysis.

Table 4.3: List of features measured for each centerline pixel.

Nr.	Features
1-3	Red, Green and Blue intensities of the centerline pixels.
4-6	Hue, Saturation and Intensity of the centerline pixels.
7-9	Mean of Red, Green and Blue intensities in the vessel.
10-12	Mean of Hue, Saturation and Intensity in the vessel.
13-15	Standard deviation of Red, Green and Blue intensities in the vessel.
16-18	Standard deviation Hue, Saturation and Intensity in the vessel.
19-22	Maximum and minimum of Red and Green intensities in the vessel.
23-30	Intensity of the centerline pixel in a Gaussian blurred ($\sigma = 2, 4, 8, 16$) of Red and Green plane.

4.1.4.1 Supervised A/V Class Assignment Approach

As a result of the acquisition process, very often the retinal images are non-uniformly illuminated and exhibit local luminosity and contrast variability. In order to make the classifier more robust, each image is processed using the method proposed by Foracchia *et al.* [107], which normalizes both luminosity and contrast based on a model of the observed image. Luminosity and contrast variability in the background are estimated and then used for normalizing the whole image.

For each centerline pixel, the 30 features listed in Table 4.3 are measured and normalized to zero mean and unit standard deviation. Some of these features were used previously in [65, 66]. We have tested the most commonly used classifiers, namely linear discriminant analysis (LDA), quadratic discriminant analysis (QDA), and k-nearest neighbor (kNN), on the INSPIRE-AVR dataset. In both LDA and QDA classifiers, it is assumed that the conditional probability density functions of both classes are normally distributed and the prior probabilities are equal.

For feature selection, we have used sequential forward floating selection [108], which starts with an empty feature set and adds or removes features when this increases or decreases the performance of the classifier using the classification accuracy as criterion.

Table 4.4 shows the performance of intensity-based classifiers on the INSPIRE-AVR image dataset using 2-fold cross-validation. The optimal value of parameter k (number of nearest neighbors) in KNN classier is obtained equal to 5. This table contains the accuracy values obtained when these classifiers are used for centerline pixel classification, and also for labeling vessel segments (links). The LDA classifier provided the best results and was selected for the A/V classification phase, using the set of selected features (1-2, 7, 10, 12-14, 16-17, 19-20 and 23-30).

The trained classifier is used for assigning the A/V classes to each one of the subgraph labels. First, each centerline pixel is classified into A or V classes (Figure 4.10(a)), then for each label

Table 4.4: Performance evaluation and comparison of individual intensity-based classifiers (INSPIRE-AVR dataset).

Classifier	Selected features	Most important feature	Accuracy-centerline pixels	Accuracy-labeling links
LDA	No. 1, 2, 7, 10, 12-14, 16, 17, 19, 20, 23-30	No. 1	75.2%	79.7%
QDA	No. 1-3,7,8,13,14,19,21-23	No. 1	73.2%	75.9%
kNN	No. 1-3,7-9,13,14,16,20,23	No. 13	68.3%	73.0.%

$(C_j^i, j = 1,2)$ in subgraph i, the probability of its being an artery is calculated based on the number of associated centerline pixels classified by LDA to be an artery or a vein. The probability of label C_j^i to be an artery is $P_a(C_j^i) = n^a_{C_j^i}/(n^a_{C_j^i} + n^v_{C_j^i})$ where $n^a_{C_j^i}$ is the number of centerline pixels of a label classified as an artery and $n^v_{C_j^i}$ is the number of centerline pixels classified as a vein. For each pair of labels in each subgraph, the label with higher artery probability will be assigned as an artery class, and the other as a vein class.

Finally, to prevent a wrong classification as a result of a wrong graph analysis, we calculate the probability of being an artery or a vein for each link individually. The probability of a link (l_i) being an artery $(P_a(l_i))$ is computed as $P_a(l_i) = n^a_{l_i}/\left(n^a_{l_i} + n^v_{l_i}\right)$, and the probability of being a vein $((P_v(l_i))$ is computed as $P_v(l_i) = n^v_{l_i}/\left(n^a_{l_i} + n^v_{l_i}\right)$, where $n^a_{l_i}$ is the number of centerline pixels of link (l_i) classified as an artery and $n^v_{l_i}$ is the number of centerline pixels classified as a vein. If the probability of being an artery is higher than 0.9 $(P_a(l_i) \geq 0.9)$ then the link will be assigned as an artery, and if $P_v(l_i) \geq 0.9$ then it will be assigned as a vein, without considering the result of the graph analysis.

Figure 4.9 shows some examples of using the LDA result for the assignment of A/V classes to each subgraph. The A/V classification result on the link inside the ellipse in Figures 4.9(a)- 4.9(c) emphasizes the impact of graph analysis on the final results of A/V classification. As it can be seen in Figure 4.9(b), if the result of LDA classifier will be used only, then the link inside the ellipse will be classified wrongly as artery, but the graph-based method correctly classified this link as vein using the labels obtained in the graph analysis step. The final result of assigning a class to the link centerline pixels is shown in Figures 4.10(b) and 4.10(c). The red color represents arteries and blue color represents the veins.

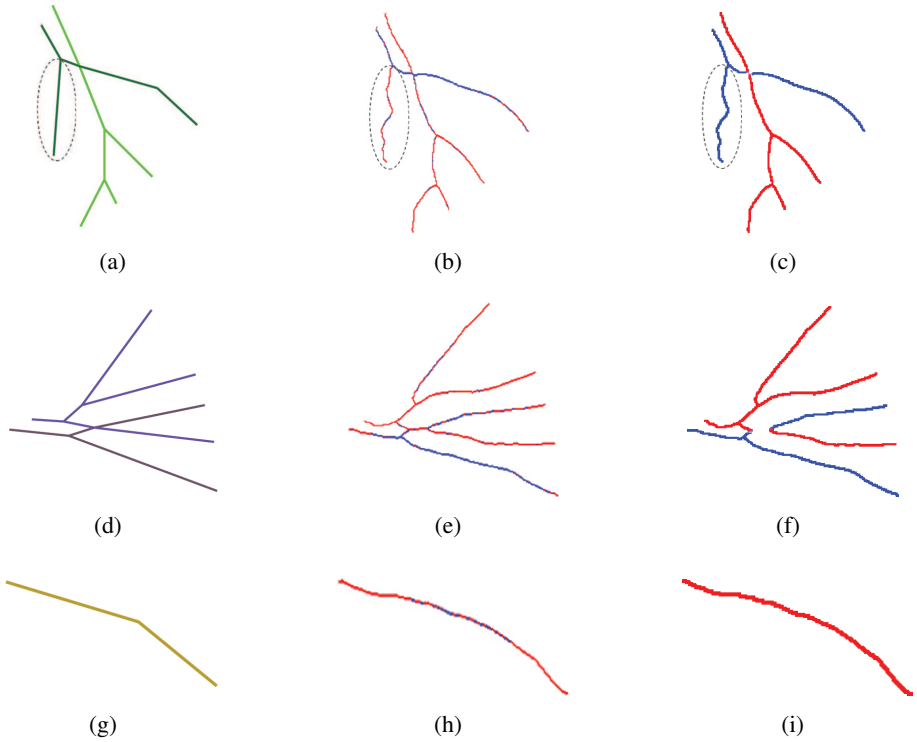

Figure 4.9: Examples of assigning A/V classes to the labels in each subgraph using LDA classifier; (a), (d) and (g) Graph analysis results for each subgraph; (b), (e) and (h) LDA classifier result; (c), (f) and (i) Final result of assigning A/V classes.

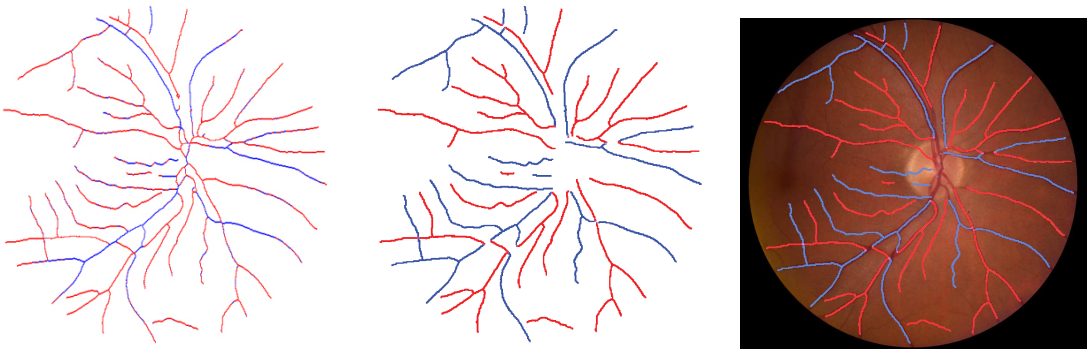

Figure 4.10: (a) LDA classifier result; (b) Final result of supervised graph-based A/V classification; (c) A/V classification result overlapped on original image (Red: arteries, Blue: veins).

4.1.4.2 Unsupervised A/V Class Assignment Approach

Since images of different datasets have diverse properties, the LDA classifier in the supervised A/V class assignment approach requires a computationally demanding training phase for each dataset. This requirement prevents the method from achieving the expected A/V classification performance when the classifier is trained with images from a different set. In order to overcome this limitation, a new unsupervised approach for the final A/V class assignment is developed using *k*-means clustering algorithm.

Figure 4.11 shows the histogram and normal distribution fit for artery pixels and vein pixels in different color planes using the manual A/V classification. As illustrated in this figure, the histogram of red intensity shows the best discrimination between artery pixels and vein pixels, although with some overlap. For this reason, we selected the red component for using in the *k*-means clustering algorithm.

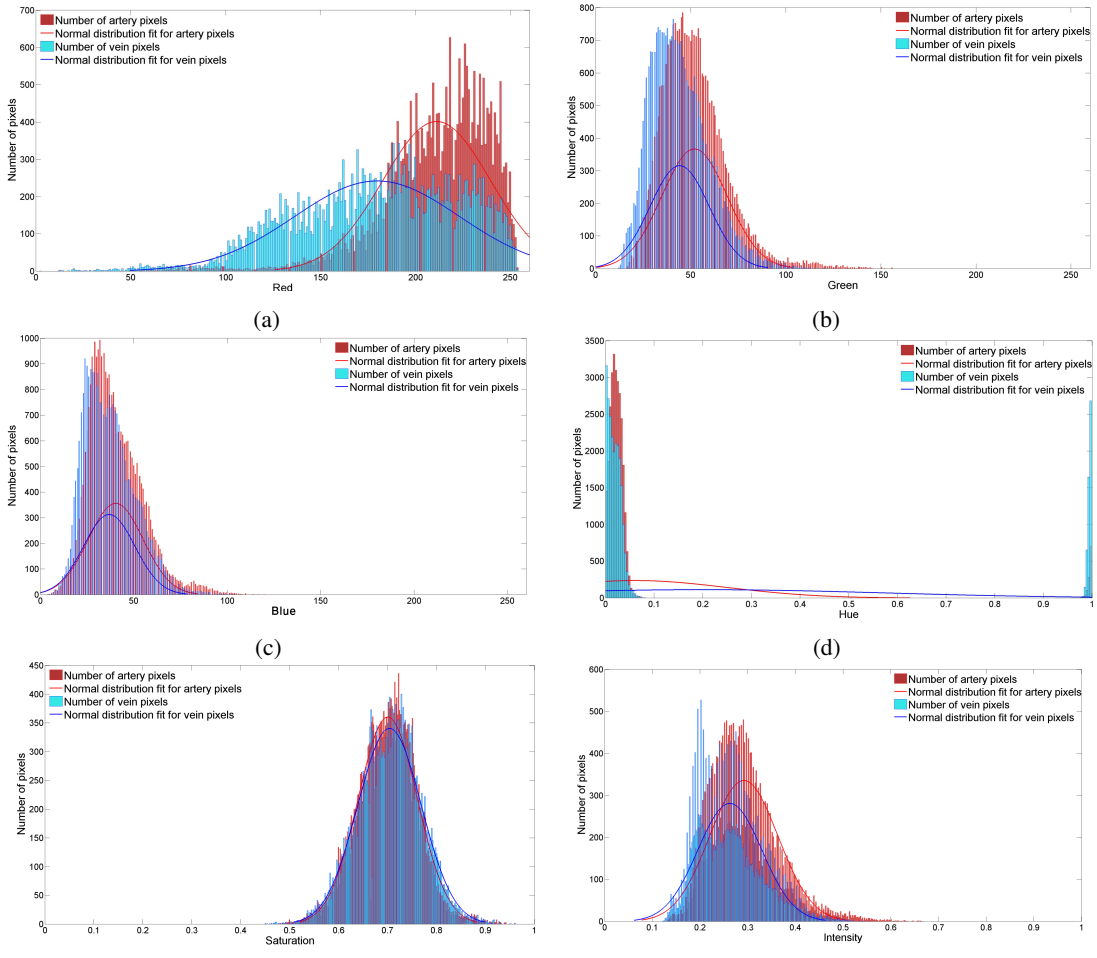

Figure 4.11: Histograms and normal distribution fits for artery and vein pixels based on manual A/V classification in (a) Red channel; (b) Green channel; (c) Blue channel; (d) Hue; (e) Saturation; (f) Intensity.

First from the original color image (Figure 4.12(a)), a normalized intensity image from red plane is obtained (Figure 4.12(b)) and the red intensity for all vessel pixels are extracted (Figure 4.12(c)) and stored in a set, I. The elements of the obtained set are sorted in ascending order which is used for determining three cluster centroids, C_v, C_u and C_a, that allow the initializing of a k-means algorithm for clustering each vessel pixel into one of three classes cases: 1) Artery; 2) Vein; 3) Unknown.

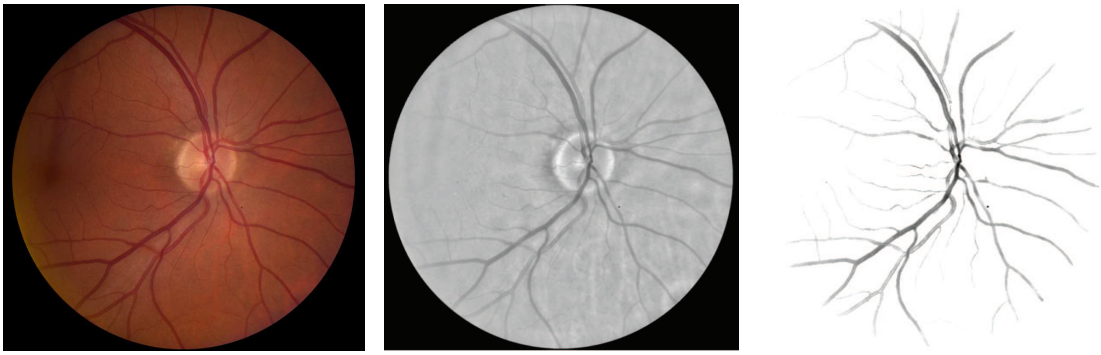

(a) (b) (c)

Figure 4.12: (a) Original image; (b) Normalized red plane; (c) Intensity of vessel pixels.

As retina arteries normally appear thinner and brighter red than the corresponding veins with a normal artery-to-vein caliber ratio of 2:3 [109], to compute the initial centroids the sorted set of intensities is divided into 7 intervals, each one containing the same number of pixels. The first 3 intervals are considered as initial vein cluster, the 2 last intervals belong to initial artery cluster and the 2 middle intervals are initially considered as unknown cluster. The different number of intervals in the artery and vein classes derives from the fact that veins are larger than arteries, so we have more vein pixels than artery pixels. All intensities in the 2 middle intervals are associated with the unknown class for the case of uncertainty. As it is illustrated in Figure 4.13, the initial centroids, C_v, C_u and C_a, are set equal to the center of vein, unknown and artery initial clusters, respectively. Figure 4.14 shows the obtained initial cluster centroid positions on the histogram of Red intensity.

Using the k-means algorithm and the obtained initial centroids all vessel pixels are clustered as artery, vein or unknown as shown in Figure 4.15(a). Then, the probability of a label being an artery is calculated based on the relation between the number of pixels in each cluster. Subsequently, in each paired subgraph (Figure 4.15(b)), the label with higher artery probability will be considered as an artery, and the other one as a vein, where the result is illustrated in Figure 4.15(c).

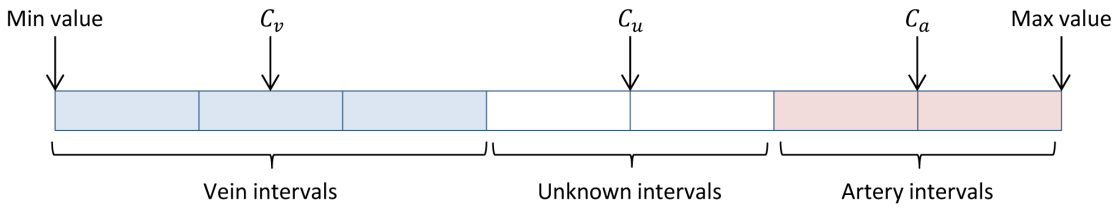

Figure 4.13: Initial cluster centroid positions on the sorted set of intensities.

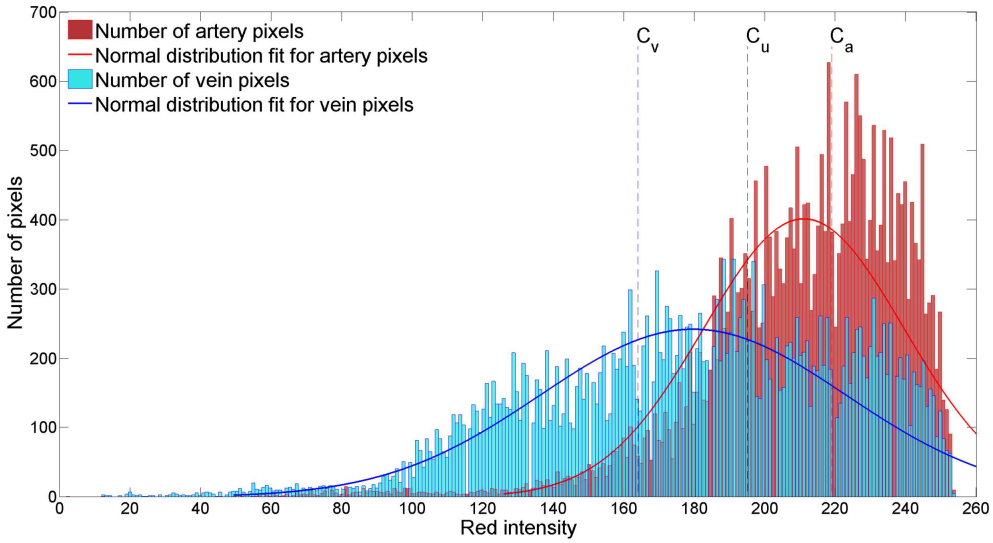

Figure 4.14: Initial cluster centroid positions on the histogram of Red intensity.

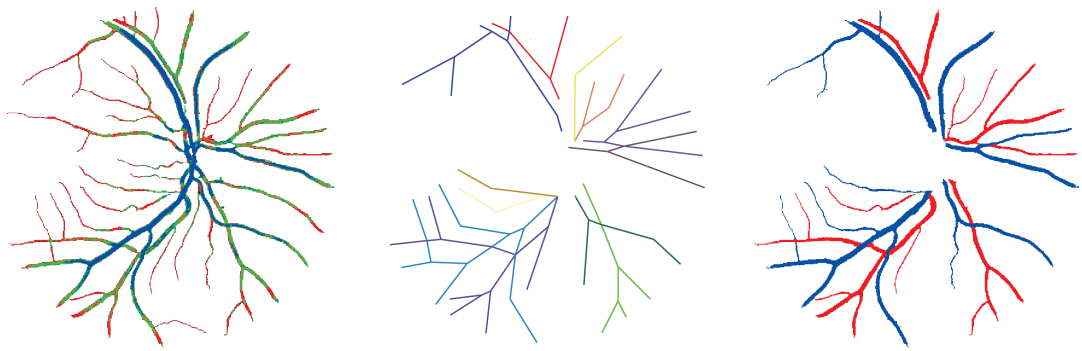

(a) (b) (c)

Figure 4.15: (a) *k*-means clustering result (Red: artery, Blue: vein and Green: unknown); (b) Paired subgraphs; (c) Result of assigning A/V classes to paired subgraphs using *k*-means algorithm.

In the next step, the two thresholds are recalculated based on the result of A/V assignment in paired-subgraphs. The threshold values for arteries (T_a) and veins (T_v) are set as

$$T_a = \mu_a - \sigma_a \tag{4.7}$$

$$T_v = \mu_v + \sigma_v \tag{4.8}$$

where μ_a is the average intensity and σ_a is the standard deviation of all pixels in the artery subgraphs previously classified, respectively, and μ_v and σ_v have identical definition for the vein subgraphs. Afterwards, the classification process is repeated for all vessel pixels based on the obtained threshold. Each pixel (p) with intensity of I_p is classified as following:

$$\text{For each pixel } (p) \begin{cases} \text{if } I_p \leq T_v & \Rightarrow p \in \text{Vein class} \\ \text{if } I_p \geq T_a & \Rightarrow p \in \text{Artery class} \\ \text{if } T_v < I_p < T_a & \Rightarrow p \in \text{Unknown class} \end{cases} \tag{4.9}$$

For the subgraphs, each vessel pixel is counted as a vein or an artery using the threshold values and the probability of each label to be an artery is calculated. Then for each label in each unpaired subgraph if the probability of being artery is higher than 0.5 then the label will be assigned as artery or otherwise it will be assigned as vein; and for each pair of labels in paired subgraphs, the label with higher artery probability is assigned as an artery class, and the other as a vein class.

Finally, to prevent a wrong classification of a link as a result of an error in the analysis of the graph, A/V probability for each individual vessel (graph link) is also calculated. If one of these probabilities is higher than 0.8, the vessel is considered as belonging to that class independently of the result derived from the subgraph classification procedure. Final result of unsupervised A/V classification is shown in Figure 4.16.

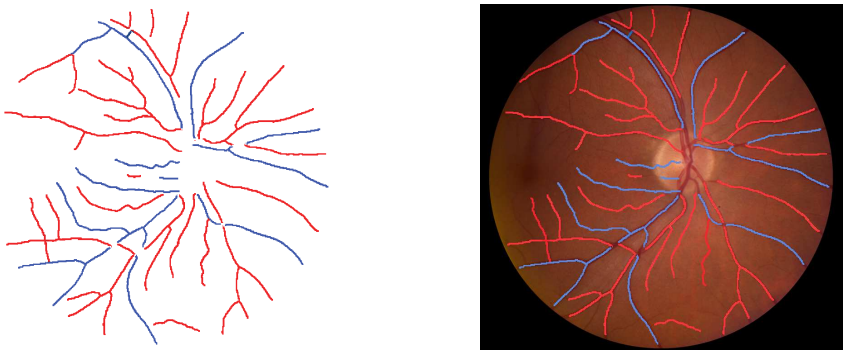

(a) (b)

Figure 4.16: (a) Final result of unsupervised graph-based A/V classification; (b) Unsupervised A/V classification result overlapped on original image (Red: arteries, Blue: veins).

4.2 Results

The automatic methods described in the previous sections were tested on the images of two datasets, DRIVE [110] and INSPIRE-AVR [111] which are described in Appendix A. A manual artery/vein labeling was performed by an expert on the 20 images of the DRIVE test set and for the 40 images of the INSPIRE dataset. In following, the proposed methods were evaluated on these datasets and finally the performance of both supervised and unsupervised A/V classification approaches were compared using 25 images of a dataset from a local hospital (CHSJ dataset).

INSPIRE-AVR dataset

For applying the supervised graph-based method on the images of INSPIRE-AVR dataset, 2-fold cross-validation is used. The images are randomly assigned to two sets S_1 and S_2, so that both sets were of equal size. Then the classifier is trained on S_1 and it is tested on S_2, followed by training on S_2 and testing on S_1. For training the LDA classifier, 15,000 labeled centerline pixels were randomly selected from each set. Some results of the proposed A/V classification methods on this dataset are shown in Figure 4.17.

Table 4.5 shows the performance evaluation of the individual LDA classifier for classifying vessel segments in INSPIRE-AVR dataset, and the results obtained using the combination of graph-based classification with LDA and unsupervised graph based approach. The analysis of these values shows that both supervised and unsupervised graph-based methods outperform the accuracy of the LDA classifier alone. For further evaluation of the graph-based method, we consider a semi-automatic approach by manually assigning the A/V classes to the labels of each subgraph. The results obtained are included in the first row of Table 4.5.

For evaluating the proposed methods, the accuracy is calculated both for centerline pixel classification and for vessel pixel classification. Table 4.6 and Table 4.7 show the accuracy values for centerline and vessel pixels in the entire image, as well as for the pixels inside the region of interest (ROI) for supervised and unsupervised approaches, respectively. The ROI is usually defined for the calculation of the arteriolar-to-venular ratio; the ROI is the standard ring area within 0.5 to 1.0 disc diameters from the optic disc margin [75]. Each row of these tables contains the accuracy values calculated using different ranges for vessel calibers. The first rows contain the results for all the vessels, while the remaining rows present the results for vessels with caliber higher than 5, 10, 15 and 20 pixels.

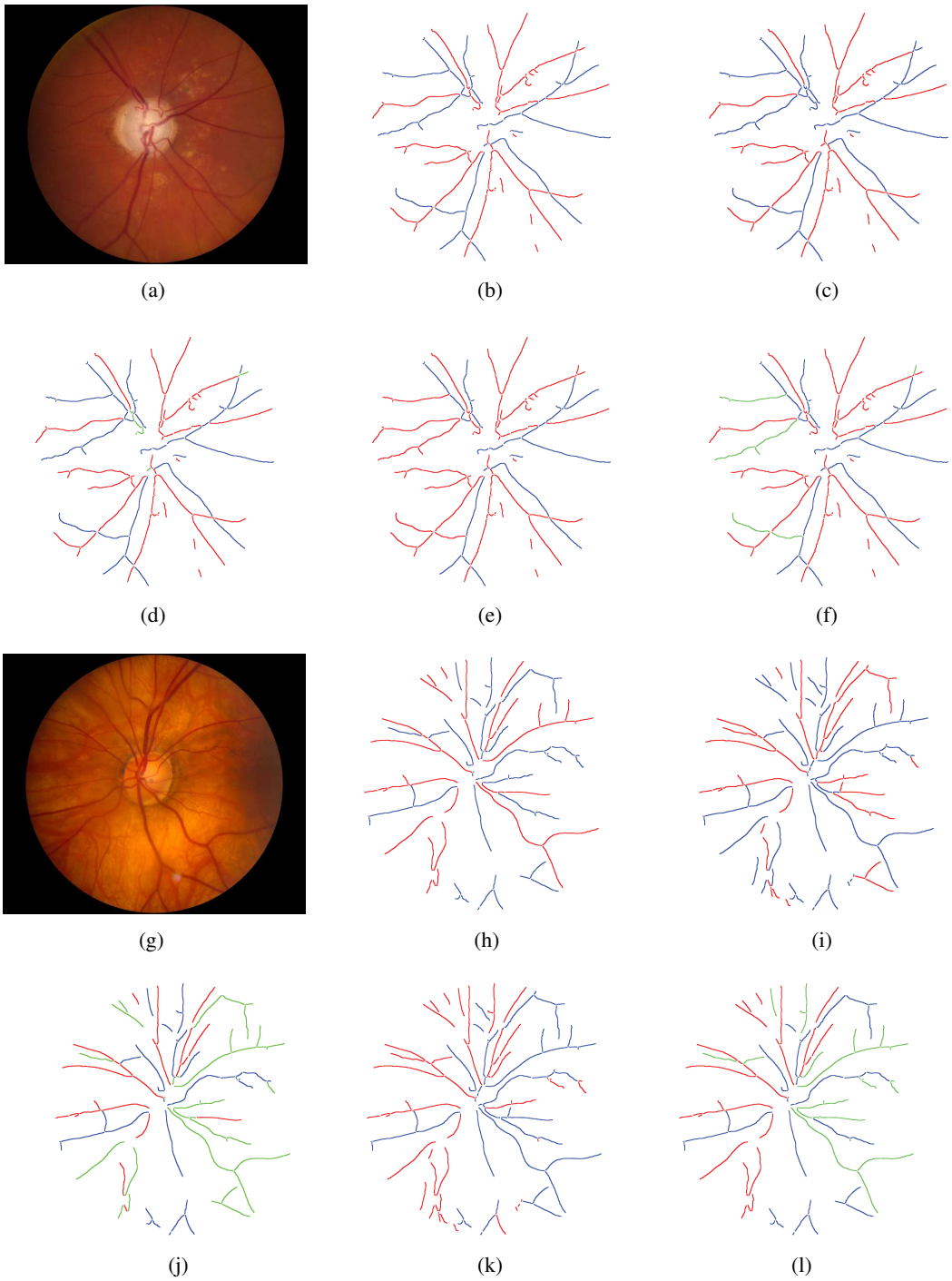

Figure 4.17: Samples of A/V classification results in INSPIRE-AVR dataset (Red: correctly classified arteries, Blue: correctly classified veins, Green: wrong classification); (a), (g) Original images; (b), (h) Manual A/V labeling; (c), (i) Supervised A/V classification results (accuracy = 97.7% and 61.2%); (d), (j) Comparison of supervised A/V classification results with manual labeling; (e), (k) Unsupervised A/V classification results; (f), (l) Comparison of unsupervised A/V classification results with manual labeling (accuracy = 89.6% and 70.1%).

Table 4.5: Accuracy of individual methods before and after combination (INSPIRE-AVR dataset).

Method		Centerline pixels in entire image	All vessel pixels in entire image	Centerline pixels inside ROI	All vessel pixels inside ROI
Semi-automatic	Manual assignment of A/V classes to the subgraph labels	90.7%	92.3%	91.3%	93.7%
Automatic	LDA-only	79.9%	85.0%	80.4%	86.2%
	Supervised graph-based	84.9%	88.3%	95.9%	91.1%
	Unsupervised graph-based	81.8%	86.1%	83.1%	87.5%

Table 4.6: Supervised graph-based method: accuracy rates for the entire image and inside the ROI (INSPIRE-AVR dataset).

Vessel caliber (vc)	Centerline pixels in entire image	All vessel pixels in entire image	Centerline pixels inside ROI	All vessel pixels inside ROI
$vc > 0$ *pixels*	84.9%	88.3%	85.9%	91.1%
$vc > 5$ *pixels*	86.5%	88.7%	87.9%	91.4%
$vc > 10$ *pixels*	89.6%	90.5%	91.1%	92.8%
$vc > 15$ *pixels*	92.6%	92.8%	95.9%	96.2%
$vc > 20$ *pixels*	93.4%	93.4%	97.1%	97.2%

vc: vessel caliber

Table 4.7: Unsupervised graph-based method: accuracy rates for the entire image and inside the ROI (INSPIRE-AVR dataset).

Vessel caliber (vc)	Centerline pixels in entire image	All vessel pixels in entire image	Centerline pixels inside ROI	All vessel pixels inside ROI
$vc > 0$ *pixels*	81.8%	86.1%	83.1%	87.5%
$vc > 5$ *pixels*	83.2%	86.5%	87.2%	89.0%
$vc > 10$ *pixels*	87.1%	88.7%	90.9%	91.7%
$vc > 15$ *pixels*	90.2%	91.1%	93.4%	94.0%
$vc > 20$ *pixels*	94.1%	94.6%	95.8%	96.2%

vc: vessel caliber

As illustrated in Figure 4.18, there is a slight decrease in the global accuracy of vessel classification for the unsupervised approach, but this fact had no special impact on the assessment of vascular changes because only the main vessel are normally involved in the calculation protocol, and no significant classification errors were observed for main vessels.

The percentage of correctly classified vessel pixels of the six largest arteries and the six largest veins inside the ROI was also calculated, as these are the vessels normally used for AVR calcu-

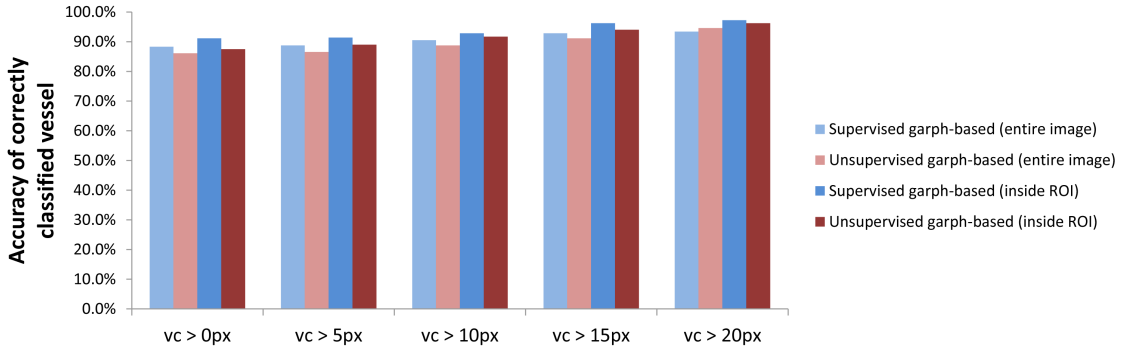

Figure 4.18: Accuracy of correctly classified vessel pixels for the supervised and unsupervised approaches in entire image and inside the ROI.

lation. An accuracy value of 98.0% and 96.8% were obtained for supervised and unsupervised methods, respectively, thus demonstrating that the proposed methodologies for A/V classification are reliable for use in an automated procedure for AVR calculation.

DRIVE dataset

For the 20 test images of the DRIVE dataset, the accuracy values of 87.4% and 86.6% were obtained for the results of supervised and unsupervised methods, respectively. These values are achieved for the classification of centerline pixels of the main vessels (vessels with caliber higher than 3 pixels). Two examples of automatic classification of DRIVE images can be observed in Figure 4.20. The differences between the results of the proposed methods and manual labeling are shown in green, while the correctly classified arteries and veins are presented in red and blue, respectively.

Results for A/V classification in DRIVE and INSPIRE-AVR images were presented by Niemeijer *et al.* using ROC curves. The reported value for the area under the curve (AUC) was 0.88 for the main vessel centerline pixels of DRIVE [65], and 0.84 for the vessel centerline pixels inside the ROI of INSPIRE-AVR images [66].

By considering arteries as negatives and veins as positives, the sensitivity values of obtained results are calculated by computing the proportion of positives which are correctly identified, while specificity values are measured by the proportion of negatives which are correctly identified. To facilitate comparison with the results of proposed approaches, sensitivity and specificity values were extracted from the figures of ROC curves presented in [65, 66], after selecting three specific cut-off points on the curves: 1) best cut-off (the balanced sensitivity and specificity values are extracted from the curve); 2) sensitivity cut-off (the specificity value is extracted from the curve on

a point where the sensitivity value is identical to the result of supervised graph-based method); 3) specificity cut-off (the sensitivity value is extracted from the curve on a point where the specificity value is identical to the result of supervised graph-based method).

The comparison of sensitivity and specificity values are presented in Table 4.8. Figure 4.19 shows Niemeijer's ROCs with these three operating points represented as blue, purple and green dots, while the result of the methods herein described are presented in red dot (supervised) and yellow dot (unsupervised). For all calculated values, both supervised and unsupervised graph-based classification methods outperform Niemeijer's approach.

Table 4.8: Comparison of sensitivity and specificity values

Method	INSPIRE-AVR		DRIVE	
	Sensitivity	Specificity	Sensitivity	Specificity
Supervised Graph-based	0.91	0.86	0.90	0.84
Unsupervised Graph-based	0.85	0.80	0.87	0.84
Niemeijer (best cut-off[1])	≈0.78	≈0.78	≈0.80	≈0.80
Niemeijer (sensitivity cut-off)	≈0.91	≈0.63	≈0.90	≈0.67
Niemeijer (specificity cut-off)	≈0.60	≈0.86	≈0.73	≈0.84

[1] cut-off: specific point on the ROC curve for extracting sensitivity and specificity values

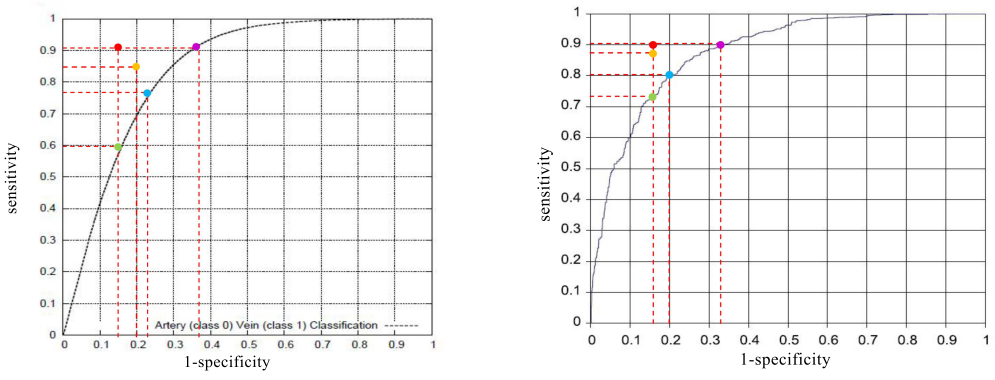

(a) (b)

Figure 4.19: Performance of the supervised graph-based method (Red dot) and unsupervised approach (Yellow dot) compared with the results of Niemeijer's method (Blue dot: best cut-off, Purple dot: sensitivity cut-off and Green dot: specificity cut-off); (a) INSPIRE-AVR dataset; (b) DRIVE dataset. (ROC curves adapted from [65, 66]).

Comparison between supervised and unsupervised approaches

Table 4.9 compares the results of the two methods for the main vessels of the images of the INSPIRE-AVR and DRIVE datasets and a subset images from Centro Hospitalar São João (CHSJ dataset). The 25 images in the subset of CHCJ dataset were captured with 2196 $\times$1958 pixels and a field of view of 45° where the manual artery/vein labeling was performed by an expert. The first row shows the accuracy of supervised graph-based method, where the CHSJ images were classified with the LDA trained using INSPIRE-AVR images. The second row of Table 4.9 represents the results of unsupervised graph-based approach.

Although a slight decrease in performance was observed for the results of unsupervised technique in the images of INSPIRE-AVR and DRIVE datasets, the higher accuracy of unsupervised approach on the images of CHSJ dataset clearly shows the higher stability and the independency of this approach from image properties (with no training phase), thus demonstrating the reliability of proposed unsupervised solution for the A/V classification. The results of supervised and unsupervised A/V classification methods in comparison with manual labeling on a sample image from CHSJ dataset are shown in Figure 4.21.

Table 4.9: Accuracy of correctly classified pixels using supervised and unsupervised graph-based approaches for the main vessels.

Method	Dataset		
	INSPIRE-AVR ($vc > 10 pixels$)	DRIVE ($vc > 3 pixels$)	CHSJ ($vc > 8 pixels$)
Supervised graph-based approach *Training set:*	90.5% *INSPIRE-AVR*	88.9% *DRIVE*	81.8% *INSPIRE-AVR*
Unsupervised graph-based approach	88.7%	88.6%	91.7%

vc: vessel caliber

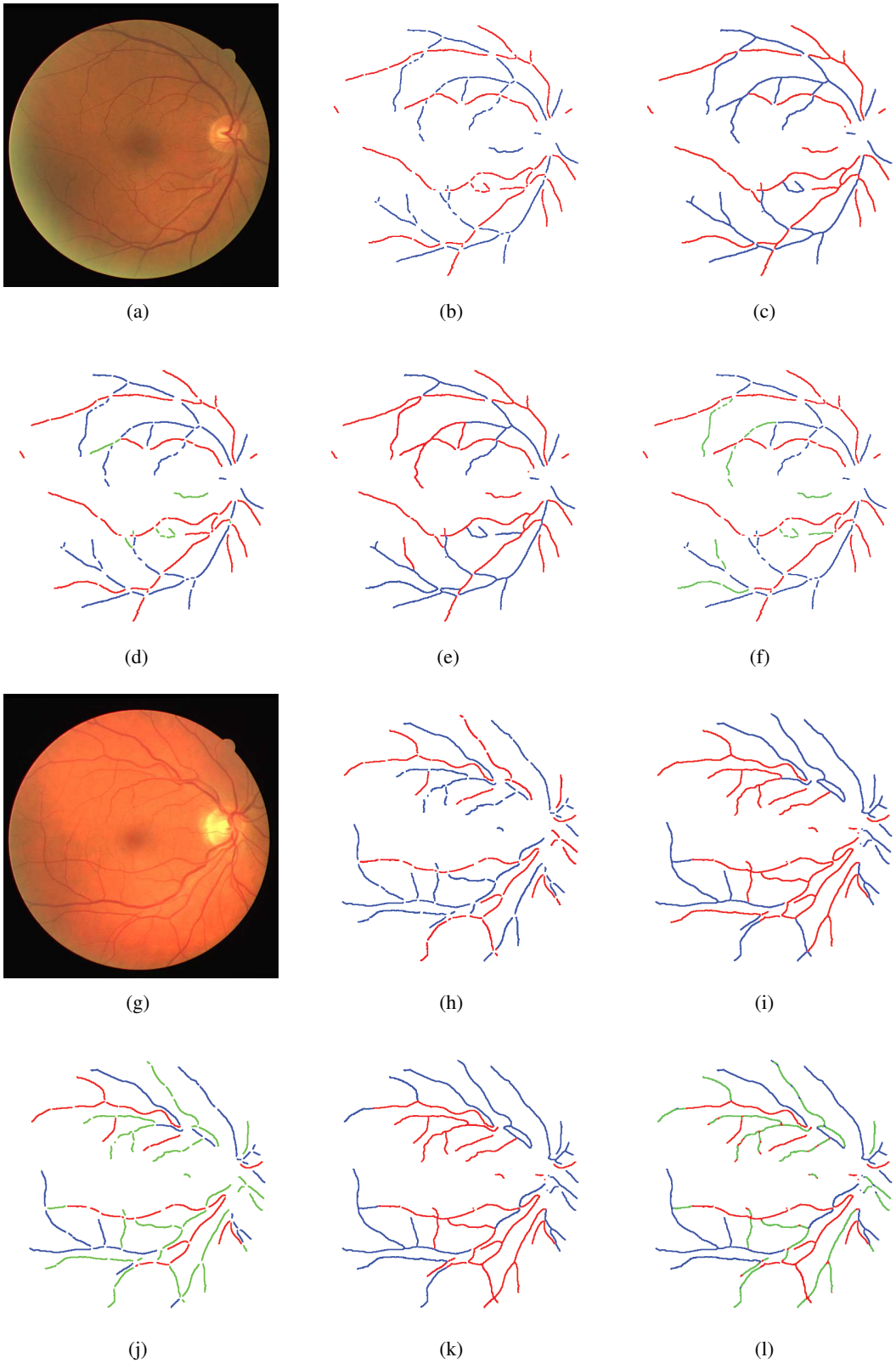

Figure 4.20: Samples of A/V classification results in DRIVE dataset (Red: correctly classified arteries, Blue: correctly classified veins, Green: wrong classification); (a), (g) Original images; (b), (h) Manual A/V labeling; (c), (i) Supervised A/V classification results (accuracy = 96.1% and 72.9%); (d), (j) Comparison of supervised A/V classification results with manual labeling; (e), (k) Unsupervised A/V classification results; (f), (l) Comparison of unsupervised A/V classification results with manual labeling (accuracy = 88.8% and 78.5%).

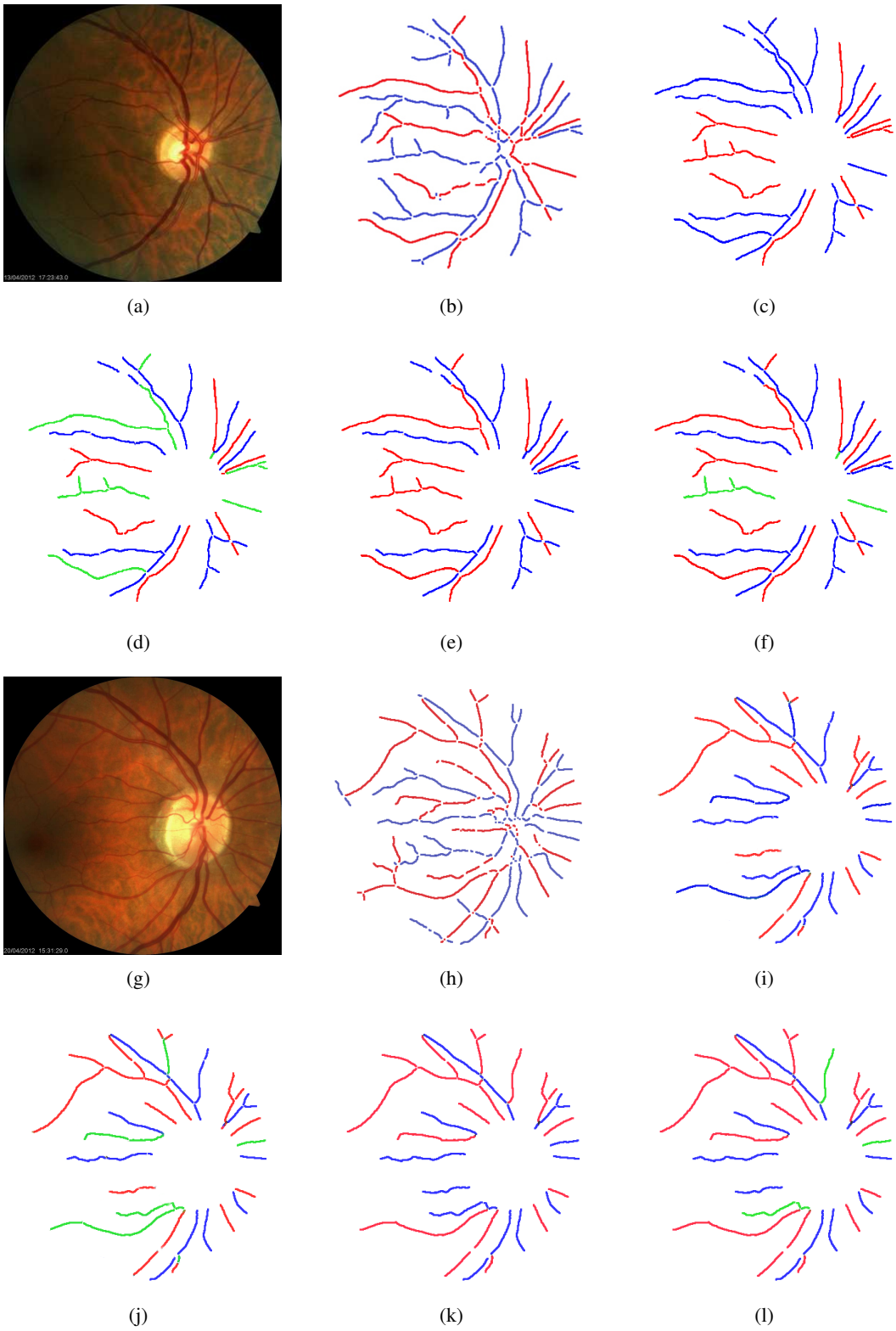

Figure 4.21: Samples of A/V classification results in CHSJ dataset (Red: correctly classified arteries, Blue: correctly classified veins, Green: wrong classification); (a), (g) Original images; (b), (h) Manual A/V labeling; (c), (i) Supervised A/V classification results (accuracy = 83.5% and 84.2%); (d), (j) Comparison of supervised A/V classification results with manual labeling; (e), (k) Unsupervised A/V classification results; (f), (l) Comparison of unsupervised A/V classification results with manual labeling (accuracy = 92.5% and 93.1%).

4.3 Concluding Remarks

The classification of arteries and veins in retinal images is essential for the automated assessment of vascular changes. In the previous sections, new automatic methodologies are described for the classification of retinal vessels into arteries and veins which is distinct from previous publications. One major difference is the fact that the proposed methods are able to classify the whole vascular tree and does not restrict the classification to specific regions of interest, normally around the optic disc. While most of the previous methods mainly use intensity features for discriminating between arteries and veins, the proposed methods use additional structural information extracted from the graph representation of the vascular network.

The information about node degree, the orientation of each link, the angles between links, and the vessel caliber related to each link are used for analyzing the graph, and then decisions on type of nodes are made (bifurcation, crossing, or meeting points). Next, based on the node types, the links that belong to a particular vessel are detected, and finally A/V classes are assigned to each one of these vessels using supervised and unsupervised approaches.

The supervised graph-based method with LDA and the unsupervised graph-based method using k-means clustering outperform the accuracy of the LDA classifier using intensity features, which shows the relevance of using structural information for A/V classification. Furthermore, the proposed approaches in comparison with other recently punished methods, achieved better results.

The promising results of proposed graph-based A/V classification methods on the images of three different datasets demonstrate the independence of these methods in A/V classification of retinal images with different properties, such as differences in size, quality, and camera angle. On the other hand, the high accuracy achieved by these methods, especially for the largest arteries and veins, confirm that this A/V classification methodology is reliable for the calculation of several characteristic signs associated with vascular alterations.

Chapter 5

Assessment of Retinal Vascular Changes

Automated detection of retinopathy in eye fundus images using digital image analysis has huge potential benefits, allowing the examination of a large number of images in less time, with lower cost and reduced subjectivity than current observer-based techniques. Another advantage is the possibility to perform automated screening for pathological conditions, such as diabetic retinopathy, in order to reduce the workload required of trained manual graders [86].

The Arteriolar-to-Venular Ratio (AVR) is an index used for the early diagnosis of diseases such as diabetes, hypertension or cardiovascular pathologies. Here, we present three automatic approaches for the estimation of the AVR in retinal images that result from the combination of different methodologies in some of the processing phases used for AVR estimation. Each one of these methods includes vessel segmentation, vessel caliber estimation, optic disc detection or segmentation, region of interest determination, vessel classification into arteries and veins and finally AVR calculation. This chapter is mostly based in the paper *"Assessment of Vascular Changes in Retinal Images"* [12].

This chapter is organized as follows. In Section 5.1, the importance of the retinal vascular changes measurement, especially the AVR, is discussed. Section 5.2 presents the methods required for accomplishing the distinct phases of the AVR estimation process. The results of the tests on the images of INSPIRE-AVR database are presented in Section 5.3, where a comparison with the reference AVR values is also included. Finally, Section 5.4 summarizes the conclusions of this chapter.

5.1 Background

Retinal vessels are affected by several systemic diseases, namely diabetes, hypertension, and vascular disorders. In diabetic retinopathy, the blood vessels often show abnormalities at early stages [112], as well as vessel diameter alterations [6]. Changes in retinal blood vessels, such as significant dilatation and elongation of the main arteries, veins, and their branches [3, 6], are also frequently associated with hypertension and other cardiovascular pathologies.

Results of different studies indicate that retinal vasculature can be deeply affected by hypertension. There is a strong association between changes in retinal vascular and blood pressure in both adult and child populations [113, 114].

Generalized retinal arteriolar narrowing is considered to be as an early characteristic sign of hypertension. The results of the Atherosclerosis Risk in Communities (ARIC) study in the United States showed that retinal arteriolar diameter is strongly and inversely related to higher blood pressure levels [115]. These data support the fact that there is a large connection between generalized arteriolar narrowing and hypertension. These studies have mainly focused on the use of smaller AVR as a way to measure generalized retinal arteriolar narrowing.

Unfortunately, clinical examinations based on ophthalmoscopy are unlikely to be capable of detecting the subtle degree of arteriolar narrowing. Advances in medical image analysis, has made it possible to detect the smallest changes in arteriolar and venular diameters.

Retinal image analysis can be used in order to study the cerebral microvasculature and related diseases due to the similarities of the retinal and cerebral vasculature in embryological origin, anatomical features, and physiological properties [116]. There is solid and consistent evidence that there is an association between retinal vascular changes and both clinical and subclinical stroke and a variety of cerebrovascular conditions independent of typical risk factors such as hypertension, diabetes, and smoking. The results of ARIC study showed that smaller retinal AVR values which is interpreted as generalized retinal arteriolar narrowing, can be an independent predictor of incident of stroke in middle-aged individuals.

Researchers show that retinal microvascular flow is reduced in individuals with cerebral small vessel disease [116], and the retinal and cerebral arteriolar histopathology in these patients is similar to stroke cases. Discovery of the deficits related to the use of retinal AVR, subsequently encouraged newer studies to evaluate the association of retinal arteriolar and venular calibers separately with the risk of stroke [117, 118]. By the use of this approach, two studies including the Rotterdam Eye Study [119] and the Cardiovascular Health Study [2] showed that, independent of

other stroke-related risk factors, wider retinal venular caliber predicted the future risk of clinical stroke rather than narrower retinal arteriolar caliber. As a result, the importance of arteriolar and venular caliber in prediction of stroke risk still remains to be determined.

Using retinal vessel measurements, recent studies have tested the hypothesis that diabetes may have etiologic links with microvascular disease. The ARIC and Beaver Dam Eye studies [119, 120], indicate that nondiabetic individuals with smaller AVR have higher risk of developing diabetes, independent of other diabetes-related risk factors. The results of Beaver Dam Study showed that this association is significantly stronger in individuals with hypertension at baseline [121]. The conductors of Rotterdam Eye Study suggested that this association may be a result of retinal venular dilatation rather than arteriolar narrowing. They verified an association of larger retinal venular caliber with pre-diabetes. This finding is consistent with earlier findings of prevalence data from the ARIC study [122]. While the responsible biological mechanisms for these observations remain to be clarified, experimental studies have shown that dilatation of retinal venules in normoglycemic patients can be achieved by administration of intravenous dextrose. Furthermore, reduced vascular reactivity associated with endothelial dysfunction and inflammatory processes may also play an essential role in the development of wider retinal venules and diabetes [123].

Several characteristic signs associated with vascular changes are measured aiming at assessing the stage and severity of some retinal conditions. Among the mentioned signs, generalized arteriolar narrowing, which is inversely related to higher blood pressure levels [117, 118], is usually expressed by the Arteriolar-to-Venular diameter Ratio (AVR). The AVR value can also be an indicator of several diseases, like diabetes, hypertension and retinopathy of prematurity [124].

5.2 Arteriolar-to-Venular Ratio (AVR) Calculation Method

The estimation of AVR requires the detection of several retinal landmarks, namely the optic disc and the vessels, followed by accurate vessel caliber measurement and artery/vein classification [75, 125]. Vessel segmentation is used for finding the vessels, and optic disc detection and segmentation is necessary to locate the ROI where vessel diameters are to be measured. An automatic AVR measurement system must also classify the retinal vessels into arteries and veins with high accuracy since small classification errors can have a significant influence on AVR values. Finally, caliber measurements are used for computing AVR according to the formula proposed

by Knudtson *et al.* [75]. Figure 5.1 shows the block diagram of the proposed method, which is detailed in the following subsections.

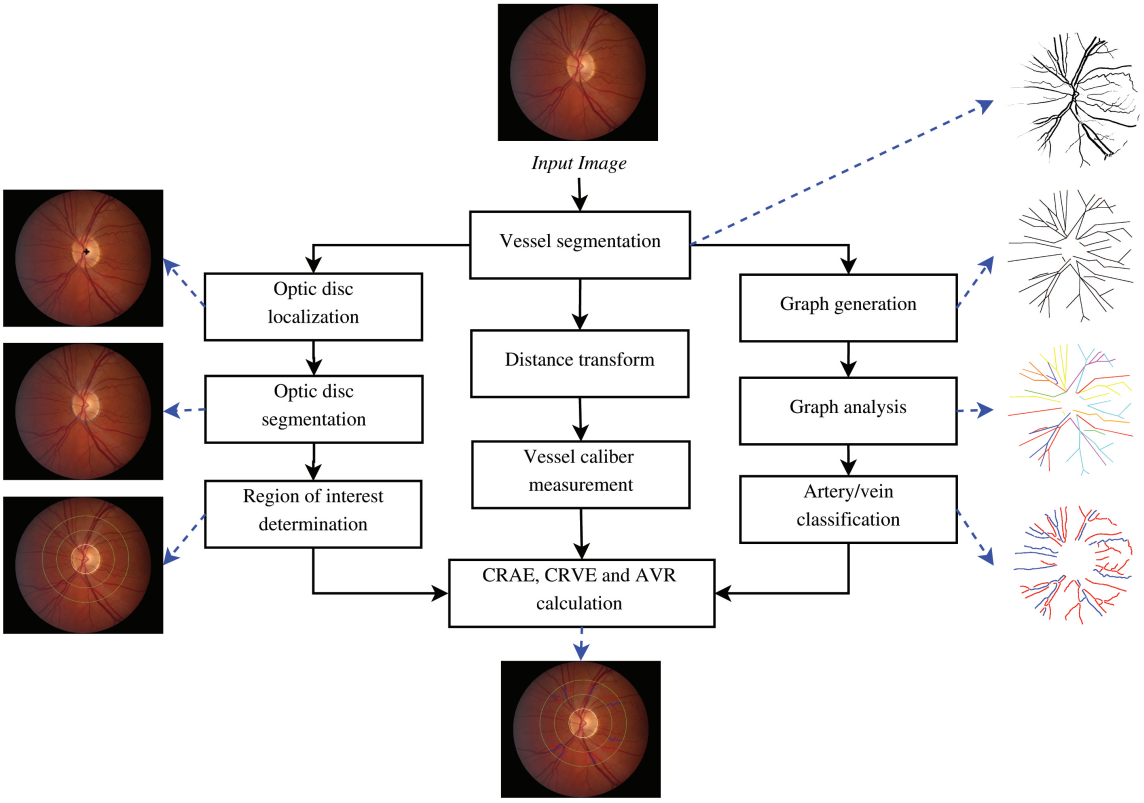

Figure 5.1: Block diagram of the proposed method for AVR estimation.

Vessel segmentation

Vessel segmentation is used for finding the vessels, and as first stage for optic disc detection and A/V classification. Vessel segmentation is also necessary for the measurement of vessel diameters. For segmenting the vessels, the method previously proposed by Mendonça *et al.* [22] was chosen which was described in Section 3.1.

The segmented vascular structure generated by this method for the high resolution image presented in Figure 5.2(a) is the binary image shown in Figure 5.2(b).

Vessel caliber measurement

Vessel calibers are the inside diameters of the blood vessels which are estimated using the distance transform of the binary vessel image. The result of this operation is a gray-level image in which the intensity value of each pixel, d_p is the Euclidean distances from the considered pixel (p) and the

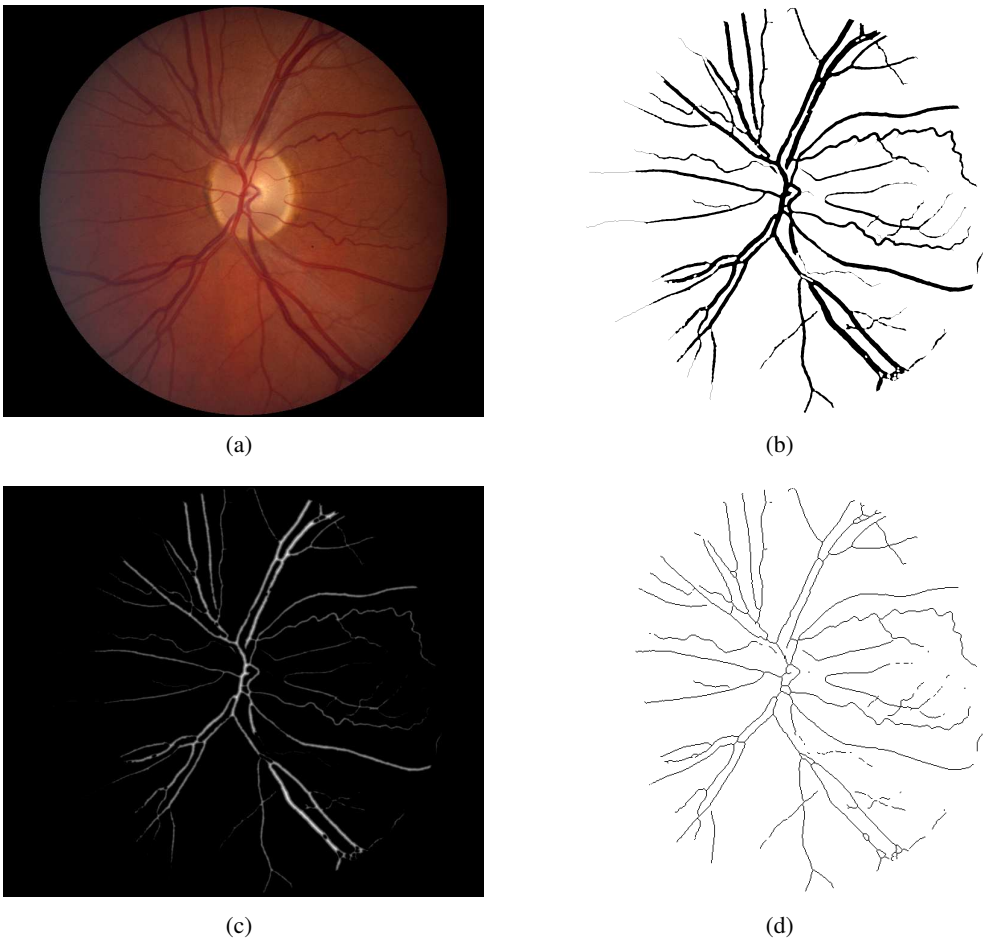

(a) (b)

(c) (d)

Figure 5.2: (a) Input image; (b) Binary vessel image result; (c) Distance transform result; (d) Centerline image.

closest background pixel. Then the image is thinned in order to extract the centerline of vessels. For each vessel centerline pixel, the vessel caliber, $vc(p)$, is simply estimated by doubling the distance values minus one ($vc = 2d - 1$).

Afterwards, for the estimation of vessel caliber for each vessel segment, the average of all vessel calibers for its centerline pixels is calculated. The results of distance transform and centerline extraction are shown in Figure 5.2(c) and Figure 5.2(d), respectively.

Region of interest determination

The literature suggest the measurement of the AVR as the ratio between artery and vein widths measured in several circumferences centered at the optic disc. In most of the approaches, the region of interest (ROI) for the AVR calculation is considered as the ring area between the circumferences with diameter d_{OD} and $1.5 \times d_{OD}$, where d_{OD} is the optic disc diameter [66, 75, 125, 126].

Benavent *et al.* [127] considered the region between $0.5 \times d_{OD}$ and $1.5 \times d_{OD}$ and used three measurements in each vessel corresponding to the intersections between the vessels and the circles with diameters $0.5 \times d_{OD}$, d_{OD} and $1.5 \times d_{OD}$. Pose *et al.* [128] took into account a region from d_{OD} outwards and they considered several measurements for the same vessel over the region. In the manual method proposed by Hubbard *et al.* [125], the experts can move outside this region in order to measure the branches of an artery and they took into account only a measurement for each vessel found in the region between circles with diameters d_{OD} and $1.5 \times d_{OD}$.

Li *et al.* [126] proposed a tracking process to find all vessel segments in the ring area between to circles with d_{OD} and $1.5 \times d_{OD}$ diameters, while, Niemeijer *et al.* [66] calculated an AVR in six concentric regions around the OD and after that they computed the final AVR as the average of these values.

In this work, the AVR is calculated from the calibers of vessels inside a ROI which is defined as the standard ring area within 0.5 to $1.5 \times d_{OD}$ from the optic disc margin [75]. As a consequence, both the localization of the optic disc center (ODC) and its diameter are required for automating the AVR calculation.

Two main options were considered for ROI definition: in the first approach, the ODC is estimated using an automatic methodology based on the entropy of vascular directions described in Mendonça *et al.* [103]. Then, the ODC is used as the center of the ROI, which is afterwards established considering a fixed disc diameter adapted to the size and field of view (FOV) of the image under analysis; the second approach delineates the OD border using SBF-based OD segmentation algorithm which was described in Chapter 3. Then for the ROI determination, the ODC and the disc diameter for each image are obtained by fitting a circle to the extracted OD boundary.

The two approaches for ROI delimitation are illustrated in Figure 5.3. The initial estimate for the ODC location, obtained by the entropy-based method, is shown in Figure 5.3(a) and the ROI defined using a fixed OD radius is presented in Figure 5.3(c). Figure 5.3(d) shows the result of segmented OD boundary using SBF-based method. The approximation of the OD boundary by a circle is illustrated in Figure 5.3(e). Figure 5.3(f) refers to ROI definition after OD segmentation.

Artery/vein classification

In order to classify a vessel as artery or vein, two alternatives are used in this work: a supervised automatic graph-based A/V classification method and the unsupervised classification method described previously in Chapter 4.

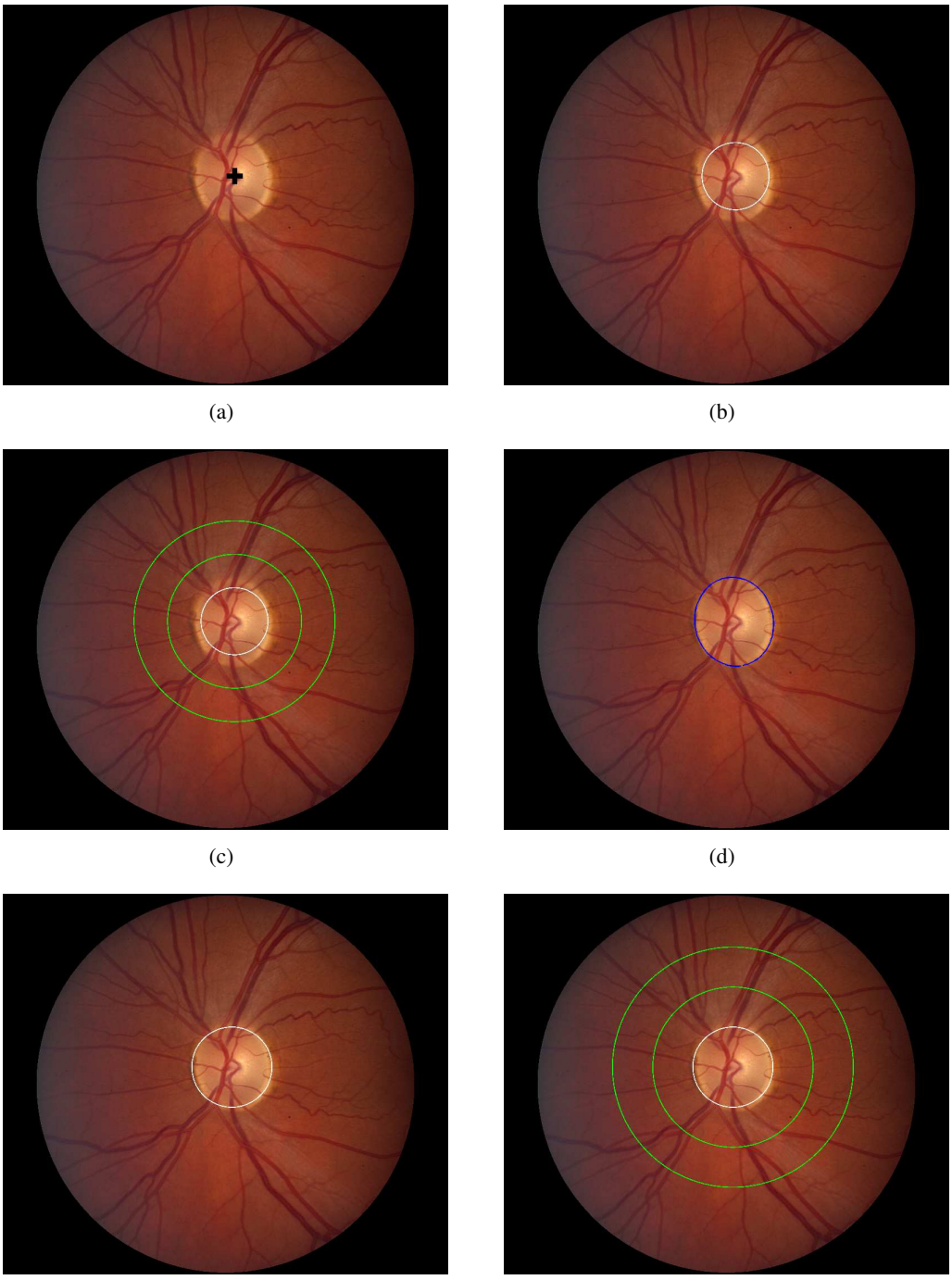

Figure 5.3: (a) Retinal image with the ODC (black cross) detected using the method based on the entropy of vascular directions; (b) Circular OD boundary using a fixed OD radius of 180 pixels centered on the initial ODC in (a); (c) ROI for AVR calculation (delimited by the two green circles) with a fixed OD radius; (d) OD boundary using SBF-based method; (e) Approximation of the OD boundary by a circle (radius of 215 pixels); (f) ROI for AVR calculation (delimited by the two green circles) and the estimated optic disc margin (white circle).

The two approaches mainly differ in the methodology for assigning the final A/V class to each one of the labels resulting from graph analysis. In the supervised approach described in Section 4.1.4.1, the structural information provided by the graph is combined with the individual setting of A/V class for each vessel provided by a linear discriminant analysis (LDA) classifier and a set of intensity features extracted from the image. The result of A/V classification for the input image in Figure 5.2(a) is displayed in Figure 5.4(a), where the red color is used for representing arteries and veins are shown in blue. Figure 5.4(b) shows the arteries and veins found inside the ROI.

The unsupervised approach described in Section 4.1.4.2, uses the red intensity of all vessel pixels and k-means clustering algorithm to assign the final A/V classes. The results of A/V classification for the whole image and for the main arteries and veins inside the ROI are shown in Figure 5.4(c) and Figure 5.4(d), respectively.

AVR Computation

Different approaches to estimate the AVR value have been proposed in the literature [125, 129], where the AVR is calculated as the quotient between the estimated averages of artery and vein widths. Parr and Spears [129, 130] and Hubbard *et al.* [125] obtained formulas which are widely used in medical studies [66, 126, 131]. In these methods, the AVR is computed as the quotient of the Central Retinal Artery Equivalent (CRAE) and the Central Retinal Venular Equivalent (CRVE) as follows

$$AVR = \frac{CRAE}{CRVE} \tag{5.1}$$

The CRAE and CRVE equivalents represent the relation among a vessel trunk and its two branches and they are computed iteratively using all vessels using Parr-Hubbard's formulas [125, 129]. The Parr-Hubbard's formulas for the calculation of CRAE and CRVE have been obtained theoretically and empirically and were afterwards revised by Knudtson *et al.* [75] . The revised formulas are independent of the number of selected vessels and only use the six main arteries and veins.

In this work, the revised formulation is used for the calculation of CRAE and CRVE. These formulas correlate highly with those previously proposed by Parr-Hubbard formulas [125, 129], with the advantages of being more robust against variability in the number of selected vessels and being independent of image scale.

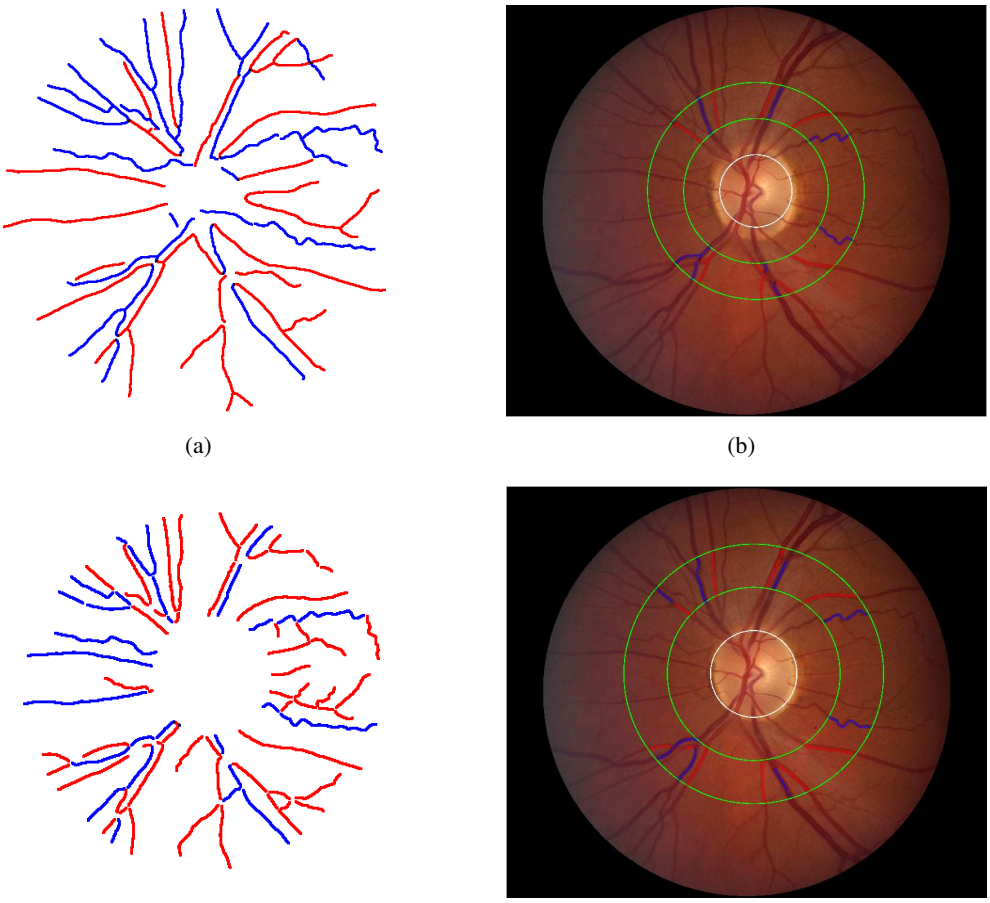

(a) (b)

(c) (d)

Figure 5.4: (a) A/V classification result using the supervised graph-based method; (b) Main vessels inside the ROI (supervised AV classification and fixed OD radius); (c) A/V classification results using the unsupervised graph-based method; (d) Main vessels inside the ROI (unsupervised AV classification and OD segmentation).

The CRAE and CRVE values based on Knudtson's revised formulas are calculated as follows

$$Arterioles : \hat{W}_a = 0.88 * \left({w_{a1}}^2 + {w_{a2}}^2\right)^{\frac{1}{2}} \tag{5.2}$$

$$Venules : \hat{W}_v = 0.95 * \left({w_{v1}}^2 + {w_{v2}}^2\right)^{\frac{1}{2}} \tag{5.3}$$

where w_{a1} , w_{a2}, and $\hat{W}_a$ are, respectively, the width of the narrowest artery, the width of the widest artery, and the estimate of parent trunk for those arteries; w_{v1}, w_{v2}, and $\hat{W}_v$ have similar meanings for veins.

For computing the CRAE, the set with the six largest arteries inside the ROI is first selected.

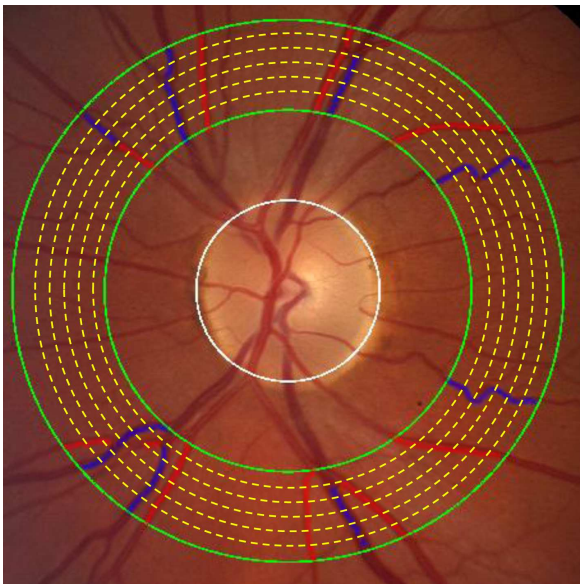

Figure 5.5: Region of interest divided in six concentric regions.

Then, the largest and the smallest vessels in this set are paired up, and the parent trunk width is determined using Knudtson's formula (5.2). A new set is formed by substituting the largest and smallest arteries with the parent trunk, and this algorithm is iterated until a single vessel is kept, whose width is the CRAE value. A similar procedure is used for calculating the CRVE, starting from the set formed by six largest veins and using Knudtson's formula (5.3). The AVR is calculated as the quotient between CRAE and CRVE.

An approach similar to the one described in Niemeijer *et al.* [66] is applied for the AVR calculation. The ROI is equidistantly sampled to provide six regions as illustrated in Figure 5.5 and for each region, the six largest arteries and the six largest veins are identified, and the regional AVR is calculated. The final AVR estimate for the complete image is the average of the six regional values.

5.3 Results

For validating the proposed AVR calculation methods, the INSPIRE-AVR dataset which contains 40 high resolution color images is used. This dataset includes two AVR measures that were computed by two ophthalmologists using a semi-automated computer program, IVAN, developed at the University of Wisconsin [111]. The AVR estimates of Observer 1 are used as reference for calculating the errors for the results of both Observer 2 and proposed methods. Three different methods for AVR calculation are used which mainly differ in the approach for A/V classification and ROI determination.

- Method 1: In this method, the results of supervised A/V classification are used and the ROI is determined by defining a ring area within 0.5 to 1.0 disc diameter from the optic disc margin and considering a fixed radius of 180 pixels for the OD.
- Method 2: Similar to method 1, the results of supervised A/V classification are used but the ROI is determined using the OD radius obtained from SBF-based OD segmentation method.
- Method 3: In this method, the A/V classification result is obtained using the unsupervised technique and the ROI is defined based on the OD radius obtained from the SBF-based OD segmentation method.

Table 5.1 summarizes the estimated AVR values for the images of the INSPIRE-AVR dataset, and besides the results achieved by the proposed method 1, it includes the values computed by the two human observers and the results produced by the recent approach presented by Niemeijer *et al.* [66]. In this table, all values were obtained considering a fixed radius of 180 pixels for the OD. The values for method 1, shown in columns 3 and 4, were calculated considering a ROI centered on the optic disc location with the vessels classified using the combination of the graph and supervised LDA classification. The reference values and the results of method 1 are repeated in the first columns of Table 5.2 that presents also the AVR values for method 2 and method 3 combining ROI establishment based on the obtained disc center and radius using the SBF-based OD segmentation method, and the two developed approaches for A/V classification (supervised A/V classification and unsupervised A/V classification).

The analysis of the individual AVR and error values, as well as the global measures included in the last four rows of both Table 5.1 and Table 5.2, allow the conclusion that the correlation coefficients and errors produced by proposed methods are similar to those of Observer 2 and of the approach presented in Niemeijer *et al.* [66].

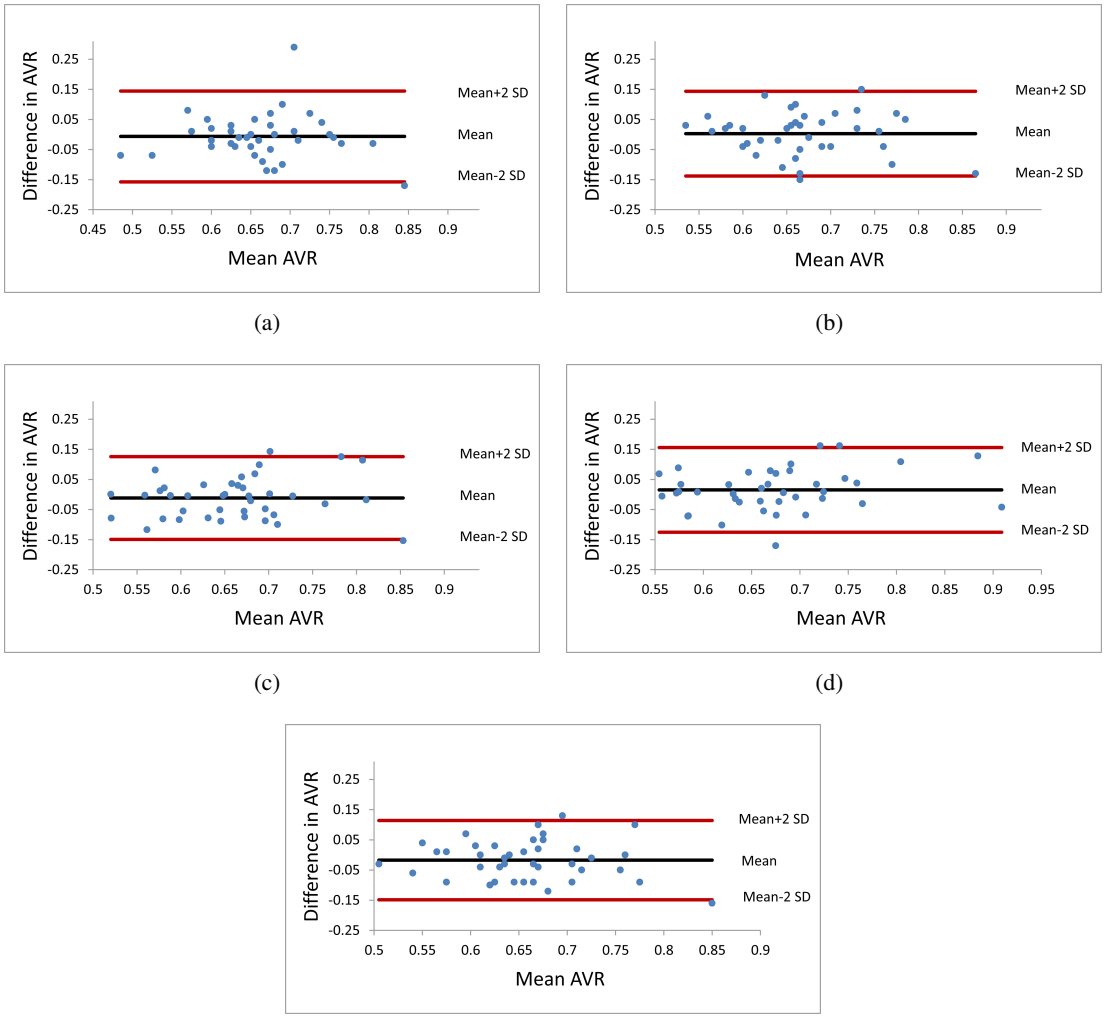

Figure 5.6: Bland-Altman plots of the agreement (a) between Observer 2 and reference; (b) between Niemeijer's method and reference; (c) between Method 1 and reference; (d) between Method 2 and reference; (e) between Method 3 and reference.

The agreement between the described methods and the reference can be observed in the Bland-Altman plots depicted in Figure 5.6, where the results of the second human observer and Niemeijer's method are also compared. Each plot shows the mean of two AVR values against the difference between them and allows a visual assessment of the distribution of errors. From the observation of these plots, it is worth mentioning that the results of the proposed methods are similar to those of Observer 2, and do not show a substantial bias as the mean of differences between the AVR values is close to 0. The 95% limits of agreement for all methods are also almost identical.

Figure 5.7 shows the boxplot graphs of the obtained AVR values by the different methods, including the reference AVR values. The scatter plots showing the correlation for all AVR values

Table 5.1: AVR values for the 40 images of the INSPIRE-AVR dataset

Image number	Reference AVR	Method 1 (OD location + Fixed OD radius) + supervised A/V classification)		Observer 2		Niemeijer's method	
		AVR	Error	AVR	Error	AVR	Error
1	0.7	0.7	0	0.71	0.01	0.62	0.08
2	0.63	0.77	0.14	0.68	0.05	0.61	0.02
3	0.7	0.64	0.06	0.65	0.05	0.59	0.11
4	0.65	0.65	0	0.64	0.01	0.68	0.03
5	0.78	0.75	0.03	0.75	0.03	0.74	0.04
6	0.65	0.68	0.03	0.65	0	0.58	0.07
7	0.67	0.62	0.05	0.65	0.02	0.74	0.07
8	0.64	0.74	0.1	0.71	0.07	0.68	0.04
9	0.69	0.6	0.09	0.76	0.07	0.77	0.08
10	0.56	0.56	0	0.85	0.29	0.57	0.01
11	0.64	0.7	0.06	0.74	0.1	0.7	0.06
12	0.76	0.66	0.1	0.75	0.01	0.81	0.05
13	0.57	0.58	0.01	0.62	0.05	0.6	0.03
14	0.62	0.5	0.12	0.58	0.04	0.59	0.03
15	0.64	0.68	0.04	0.61	0.03	0.67	0.03
16	0.68	0.68	0	0.68	0	0.67	0.01
17	0.52	0.52	0	0.45	0.07	0.55	0.03
18	0.62	0.54	0.08	0.63	0.01	0.58	0.04
19	0.67	0.59	0.08	0.63	0.04	0.71	0.04
20	0.71	0.64	0.07	0.62	0.09	0.67	0.04
21	0.57	0.59	0.02	0.58	0.01	0.59	0.02
22	0.72	0.85	0.13	0.76	0.04	0.74	0.02
23	0.66	0.68	0.02	0.69	0.03	0.81	0.15
24	0.65	0.72	0.07	0.64	0.01	0.63	0.02
25	0.56	0.48	0.08	0.49	0.07	0.69	0.13
26	0.73	0.73	0	0.61	0.12	0.6	0.13
27	0.64	0.56	0.08	0.63	0.01	0.66	0.02
28	0.63	0.58	0.05	0.68	0.05	0.61	0.02
29	0.72	0.67	0.05	0.7	0.02	0.68	0.04
30	0.59	0.59	0	0.61	0.02	0.61	0.02
31	0.75	0.86	0.11	0.75	0	0.76	0.01
32	0.53	0.61	0.08	0.61	0.08	0.59	0.06
33	0.61	0.61	0	0.59	0.02	0.71	0.1
34	0.65	0.65	0	0.61	0.04	0.68	0.03
35	0.74	0.67	0.07	0.64	0.1	0.59	0.15
36	0.69	0.67	0.02	0.62	0.07	0.64	0.05
37	0.82	0.8	0.02	0.79	0.03	0.72	0.1
38	0.93	0.78	0.15	0.76	0.17	0.8	0.13
39	0.61	0.64	0.03	0.64	0.03	0.7	0.09
40	0.74	0.65	0.09	0.62	0.12	0.81	0.07
Mean	0.67	0.65	0.05	0.66	0.05	0.67	0.06
Stdev	0.08	0.09	0.04	0.08	0.05	0.07	0.04
Min	0.52	0.48	0	0.45	0	0.55	0.01
Max	0.93	0.86	0.15	0.85	0.29	0.81	0.15
Correlation coefficient	-	0.67	-	0.55	-	0.59	-

Table 5.2: AVR values for the 40 images of the INSPIRE-AVR dataset

Image number	Reference AVR	Method 1 (OD location + Fixed OD radius + supervised A/V classification)		Method 2 (OD segmentation + supervised A/V classification)		Method 3 (OD segmentation + unsupervised A/V classification)	
		AVR	Error	AVR	Error	AVR	Error
1	0.7	0.7	0	0.73	0.03	0.72	0.02
2	0.63	0.77	0.14	0.71	0.08	0.76	0.13
3	0.7	0.64	0.06	0.69	0.01	0.61	0.09
4	0.65	0.65	0	0.62	0.03	0.62	0.03
5	0.78	0.75	0.03	0.75	0.03	0.73	0.05
6	0.65	0.68	0.03	0.73	0.08	0.66	0.01
7	0.67	0.62	0.05	0.65	0.02	0.58	0.09
8	0.64	0.74	0.1	0.8	0.16	0.69	0.05
9	0.69	0.6	0.09	0.63	0.06	0.65	0.04
10	0.56	0.56	0	0.59	0.03	0.63	0.07
11	0.64	0.7	0.06	0.74	0.1	0.71	0.07
12	0.76	0.66	0.1	0.59	0.17	0.76	0
13	0.57	0.58	0.01	0.57	0	0.58	0.01
14	0.62	0.5	0.12	0.55	0.07	0.72	0.1
15	0.64	0.68	0.04	0.71	0.07	0.64	0
16	0.68	0.68	0	0.69	0.01	0.65	0.03
17	0.52	0.52	0	0.59	0.07	0.49	0.03
18	0.62	0.54	0.08	0.55	0.07	0.53	0.09
19	0.67	0.59	0.08	0.57	0.1	0.57	0.1
20	0.71	0.64	0.07	0.64	0.07	0.62	0.09
21	0.57	0.59	0.02	0.58	0.01	0.51	0.06
22	0.72	0.85	0.13	0.77	0.05	0.82	0.1
23	0.66	0.68	0.02	0.82	0.16	0.68	0.02
24	0.65	0.72	0.07	0.68	0.03	0.61	0.04
25	0.56	0.48	0.08	0.55	0.01	0.57	0.01
26	0.73	0.73	0	0.72	0.01	0.72	0.01
27	0.64	0.56	0.08	0.63	0.01	0.63	0.01
28	0.63	0.58	0.05	0.63	0,00	0.59	0.04
29	0.72	0.67	0.05	0.73	0.01	0.69	0.03
30	0.59	0.59	0	0.6	0.01	0.62	0.03
31	0.75	0.86	0.11	0.86	0.11	0.66	0.09
32	0.53	0.61	0.08	0.62	0.09	0.57	0.04
33	0.61	0.61	0	0.64	0.03	0.61	0
34	0.65	0.65	0	0.67	0.02	0.7	0.05
35	0.74	0.67	0.07	0.78	0.04	0.62	0.12
36	0.69	0.67	0.02	0.67	0.02	0.6	0.09
37	0.82	0.8	0.02	0.95	0.13	0.73	0.09
38	0.93	0.78	0.15	0.89	0.04	0.77	0.16
39	0.61	0.64	0.03	0.68	0.07	0.64	0.03
40	0.74	0.65	0.09	0.67	0.07	0.69	0.05
Mean	0.67	0.65	0.05	0.68	0.05	0.65	0.05
Stdev	0.08	0.09	0.04	0.1	0.05	0.07	0.04
Min	0.52	0.48	0	0.95	0	0.49	0
Max	0.93	0.86	0.15	0.55	0.17	0.82	0.16
Correlation coefficient	-	0.67	-	0.69	-	0.64	-

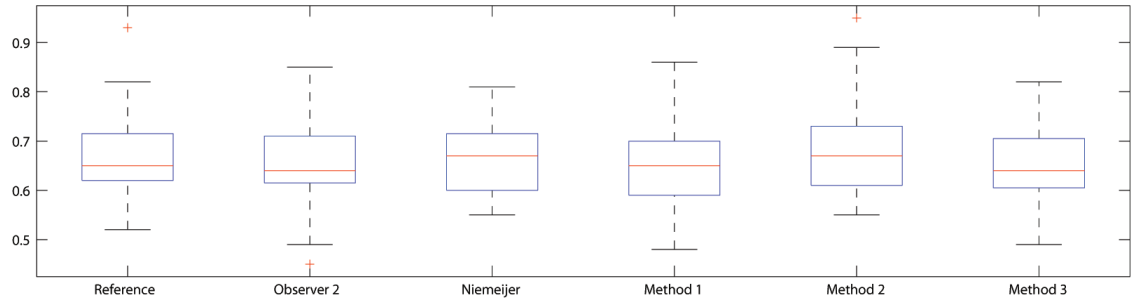

Figure 5.7: Boxplot of AVR values for different methods.

are depicted in Figure 5.8. The results demonstrate that the methods provides an estimation of the AVR similar to the one obtained by the human observers.

The AVR value can be used as a sign for screening patients in the case of diabetes, hypertension or other cardiovascular diseases. Different values of AVR are considered as a threshold for the differentiation between subjects with or without pathological conditions, depending on the method which is used for the AVR calculation.

Here, in order to evaluate the performance of the proposed methods for clinical applications, the 40 subjects of INSPIRE-AVR dataset are classified based on a threshold as pathological and non-pathological using the obtained AVR values for each method. Since there is no information about the average of AVR values for the normal subjects, several values between the range of 0.63-0.70 are defined as a threshold (T_{AVR}) for the classification of subjects. If the AVR value of a subject is higher than the threshold the subject is considered as non-pathological, otherwise as pathological one.

Figure 5.9(a) shows the number of subjects with matched classification for different methods when compared with the reference values, while Figure 5.9(b) shows the number of subjects with mismatched classification. As defined in 5.4, the matched classification means that the classification result of a subject based on the reference value (R_{AVR}) and the method value (M_{AVR}) is the same, while the mismatched classification represents that the results of classification using reference value and method value are not the same.

$$\begin{cases} M_{AVR} \leq T_{AVR} \text{ and } R_{AVR} \leq T_{AVR} & \Rightarrow \quad \text{Matched classification} \\ M_{AVR} > T_{AVR} \text{ and } R_{AVR} > T_{AVR} & \Rightarrow \quad \text{Matched classification} \\ M_{AVR} \leq T_{AVR} \text{ and } R_{AVR} > T_{AVR} & \Rightarrow \quad \text{Mismatched classification} \\ M_{AVR} > T_{AVR} \text{ and } R_{AVR} \leq T_{AVR} & \Rightarrow \quad \text{Mismatched classification} \end{cases} \tag{5.4}$$

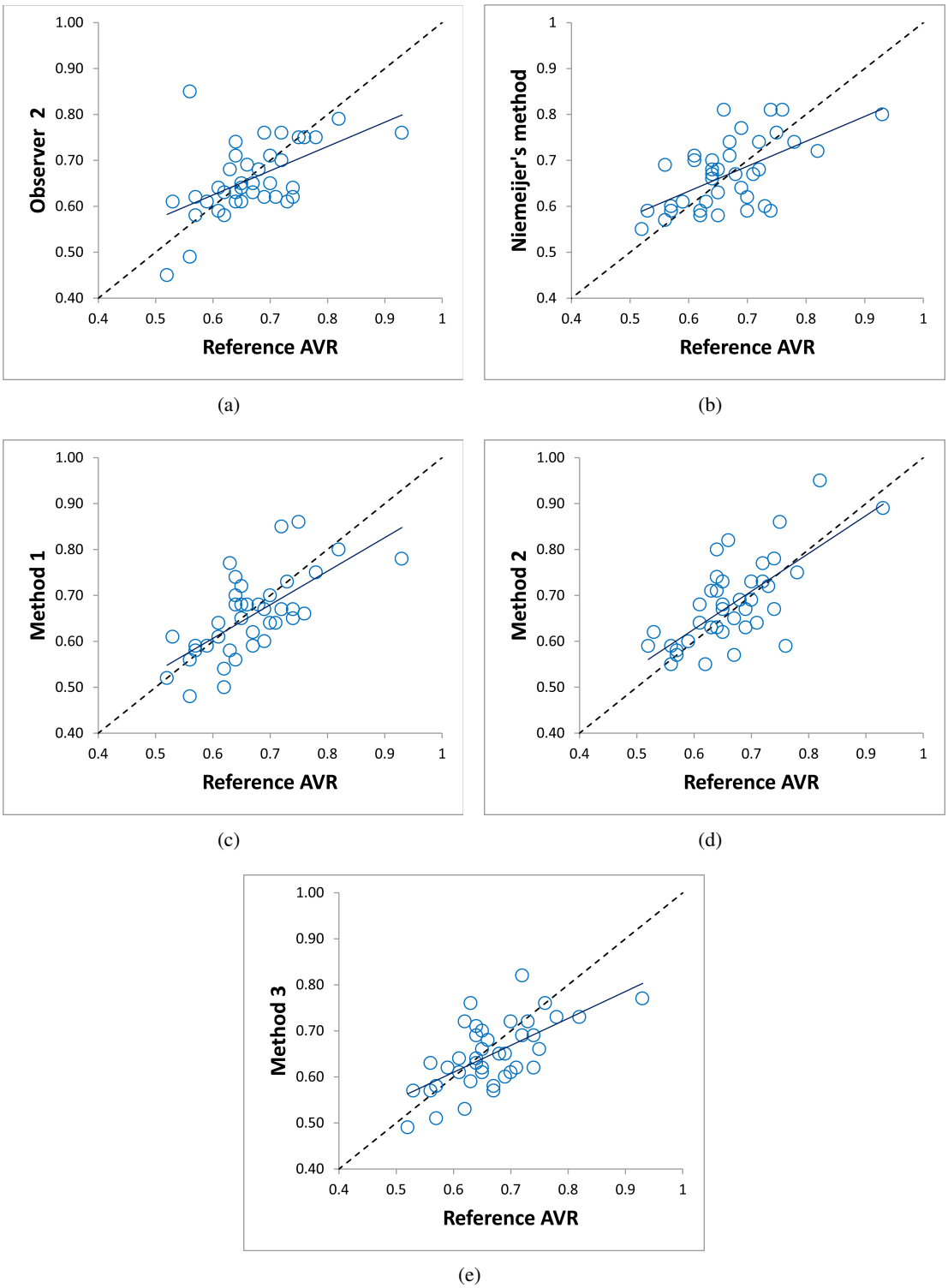

Figure 5.8: Scatter plots and regression lines between reference AVR values (a) between Observer 2 and reference; (b) between Niemeijer's method and reference; (c) between Method 1 and reference; (d) between Method 2 and reference; (e) between between Method 3 and reference.

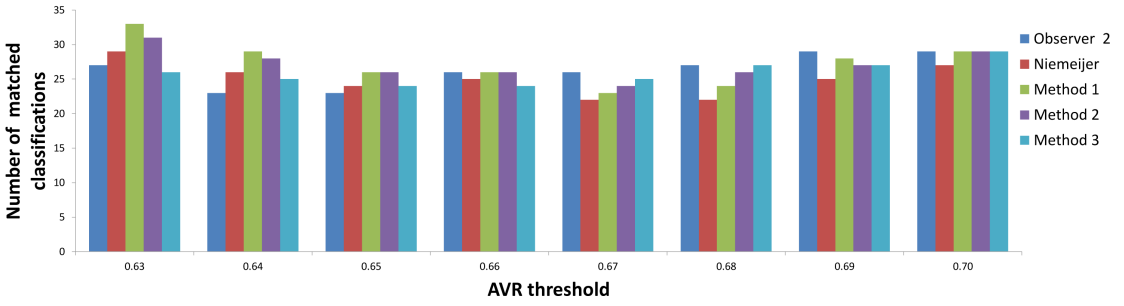

(a)

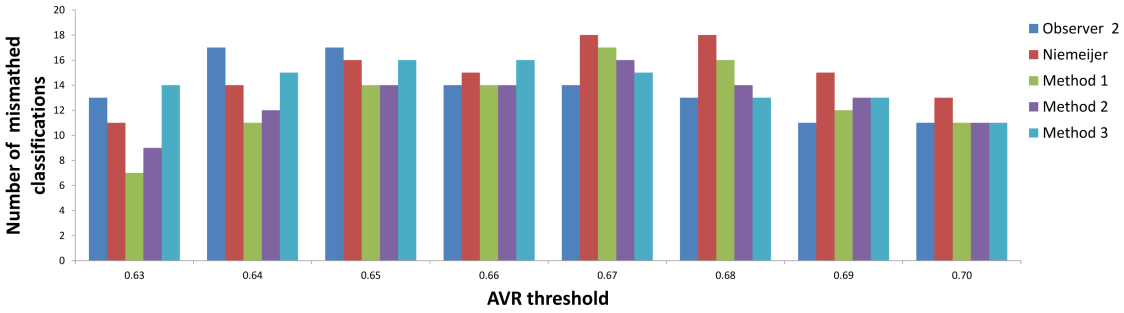

(b)

Figure 5.9: (a) Number of subjects with matched classification between methods and reference; (b) Number of subjects with mismatched classification between methods and reference

As it can be seen in Figure 5.9(a) and Figure 5.9(b), the number of matched and mismatched classifications for the proposed approaches are similar to the ones for the second observer in the case of considering different AVR values as a threshold. For example by consideration the AVR threshold value equal to 0.66, the number of matched classification between the reference and observer 2 is 26, while the number of matched classification between reference and method 1, method 2 and method 3 are 26, 26 and 24, respectively.

5.4 Concluding Remarks

In this chapter, three automatic approaches for calculating AVR in retinal images are described which are supported by a new approach for the optic disc segmentation and by new supervised and unsupervised techniques for the artery/vein classification. The proposed approaches were assessed in the 40 images of the INSPIRE-AVR dataset.

For comparison purposes, first a fixed OD diameter is defined identical to the one established by other authors for this set of images. This solution has achieved a mean error of 0.05, identical to the one obtained by the second human observer.

However, in order to increase the independence of AVR calculation from the particular characteristics of the images to be evaluated, two new solutions that are alternatives to the first one are described. One of the methods complements the OD detection algorithm with a segmentation approach that allows the estimation of the actual disc radius of the image under analysis, thus making the definition of the ROI for AVR calculation a fully automated procedure.

The other method is an unsupervised classifier using intensity features whose results still needs to be combined with the structural information extracted from the graph representation for A/V classification purposes. This is also an important step towards automation because the classifier is naturally adapted to the intensity characteristics of each particular image. Although the unsupervised classification approach has produced a slight decrease in the global accuracy of vessel classification, this fact had no special impact on the result of AVR calculation because only the main vessel are normally involved in the calculation protocol, and no significant classification errors were observed for these vessels.

The AVR values presented in Table 5.1 and Table 5.2 show that the proposed methods have a performance similar to those of human observers. The low errors and good correlation with reference AVR values are promising and demonstrate that described approaches have a high potential for clinical application.

Chapter 6

Experimental Results

This chapter presents RetinaCAD (Retinal Computer-Aided Diagnosis), an automatic system for analysing retinal images aiming at the estimation of features derived from retinal vasculature useful for the early detection and diagnosis of several systemic diseases. From the ophthalmologic point of view, this system is also relevant for assessing the implications of such diseases in the eye, as well as to evaluate the response of patients to specific therapeutic approaches. Several semi-automatic retinal image analysis systems have been proposed but the development of a fully automatic system for the assessment of vascular changes is still open.

In this chapter, the image analysis tools available in RetinaCAD are presented, namely vessel segmentation, vessel width estimation, artery/vein (A/V) classification and optic disc segmentation. A pipeline of these methods, already described in the previous chapters, allows the computation of some relevant vessel related indexes, namely CRAE, CRAE and AVR, as well as various geometrical features associated with vessel bifurcations. The evaluation of the system on images of a new dataset from a local hospital shows a low failure rate and a significant correlation between the AVR calculated for distinct images of both eyes of the same patient. The obtained AVR values are also compared with the clinical information available for the subjects in this dataset. The images and clinical information in this study are anonymized and informed consent was obtained from all individuals.

This chapter is organized as follows. Section 6.1 describes the RetinaCAD system and the tools available in the framework of the application. Experimental results using the images of a dataset from a local hospital are presented in Section 6.2. Finally, Section 6.3 summarizes the conclusions of this chapter.

6.1 RetinaCAD System

The RetinaCAD is a fully automatic system for the segmentation and classification of retinal structures and for the measurement of vascular features. This system can analyse optic disc centered retinal images with variable resolution and camera field of view. The implemented image analysis methods in this system are the ones that are introduced in the previous chapters.

The developed system interacts with the user by means of a Graphical User Interface (GUI) which is shown in Figure 6.1. The implementation of the system was performed using MATLAB® R2013a version 8.1 (MathWorks Inc, Nattick, Massachusetts, USA).

6.1.1 Tools

The main retinal image analysis tools provided by this application were detailed in the previous chapters. All tools are fully automatic and have shown a good performance when applied both individually and in combination. The list of available tools is the following:

1. Vessel segmentation
2. Vessel centerline extraction
3. Optic disc localization
4. Optic disc segmentation
5. Graph generation
6. Graph modification
7. A/V vessel classification
8. ROI determination

The system has two options for using these tools:

1. Option to process each one of these tools as an individual task.
2. Single click option which uses these tools to compute some relevant vessel related indexes, namely CRAE, CRAE and AVR, as well as various geometrical features associated with vessel bifurcations.

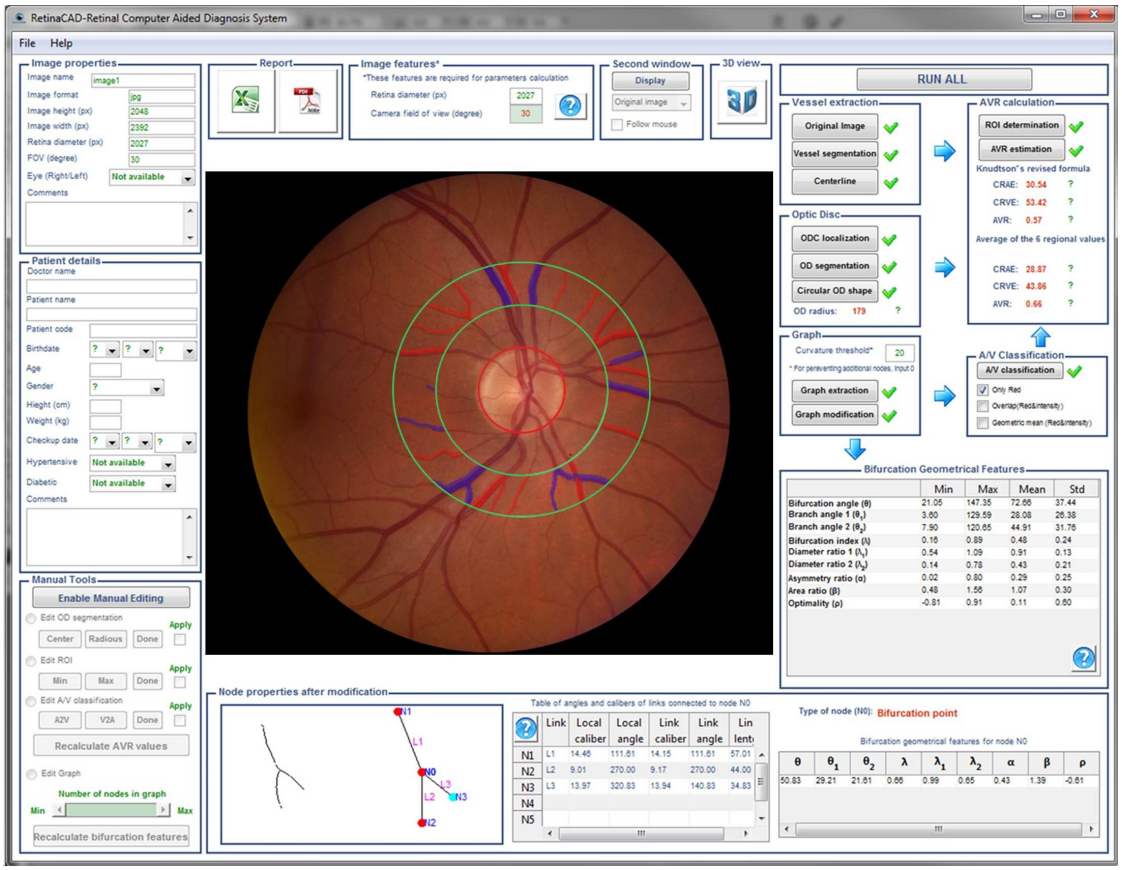

(a)

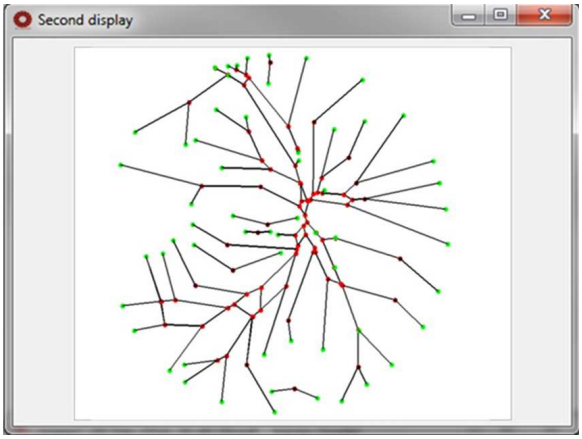

(b)

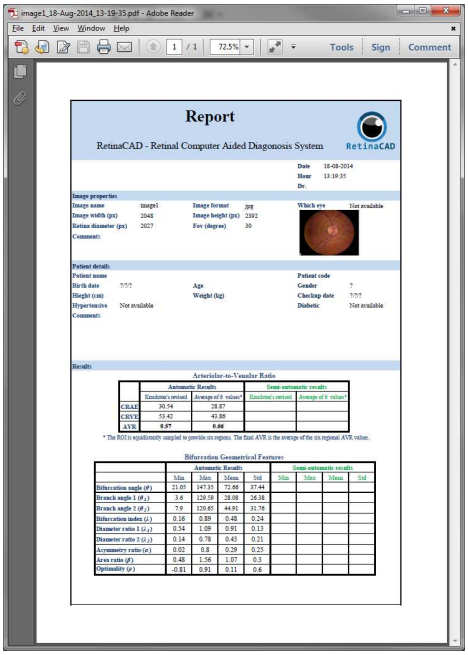

(c)

Figure 6.1: RetinaCAD graphical user interface; (a) Main screen; (b) Second display; (c) Report.

6.1.2 Measurements

In addition to the measurement of vessel calibers, this application automatically obtains some retinal image characteristics and computes several vascular features, namely the CRAE, CRVE, AVR and bifurcation geometrical features. The list of measurements provided by RetinaCAD system is the following:

1. Diameter of the retinal image (in pixels)
2. Location of the optic disc center
3. Optic disc radius
4. Central Retinal Artery Equivalent (CRAE)
5. Central Retinal Venular Equivalent (CRVE)
6. Arteriolar-to-Venular Ratio (AVR)
7. Bifurcation geometrical features, namely bifurcation index, asymmetry ratio, diameter ratio, area ratio and Optimality.

Computation of bifurcation geometrical features

Alterations in the geometry of the retinal vascular network reflect a state of vascular dysfunction. Several features representative of the retinal bifurcation geometry have been evaluated in association with various systemic conditions [132,133]. The bifurcation geometrical features are obtained from the graph representation of the vascular network. In each bifurcation, we consider a trunk vessel and two branches, the largest and the smallest, with diameters d_0, d_1, and d_2, respectively. The branching angles are the basic measurements related to a bifurcation. At each bifurcation, the branching angles and vessel segment calibers are used for deriving features which were defined before in [133], such as:

- Bifurcation angle (θ): angle between the smallest and largest branches.
- Bifurcation index (λ): quotient between the diameter of the smallest and largest branches.

$$\lambda = d_2/d_1 \tag{6.1}$$

- Asymmetry ratio (α): cross-sectional area of the smallest branch divided by that of the largest.

$$\alpha = d_2^2/d_1^2 \tag{6.2}$$

- Diameter ratios (λ_1, λ_2): branches diameters divided by trunk diameter.

$$\lambda_1 = d_1/d_0, \quad \lambda_2 = d_2/d_0 \tag{6.3}$$

- Area ratio (β): sum of the cross-sectional areas of two branches divided by that of the trunk.

$$\beta = \left(d_1^2 + d_2^2\right)/d_0^2 \tag{6.4}$$

- Optimality (ρ): deviation of the junction exponents from the optimal value of 3 based on branching physiological principles [134].

$$\rho = \left[d_0^3 - \left(d_1^3 + d_2^3\right)\right]^{1/3}/d_0 \tag{6.5}$$

6.1.3 Additional Features

In order to increase interactivity and usability, additional features and tools are added to this application:

1. Single click option for the CRAE, CRVE and AVR estimation
2. Visualization of intermediate and final results
3. Ability to process an individual task
4. Display of vessel bifurcation/intersection (graph node) local and global features using a mouse click, such as:
   - Vessel segment caliber
   - Angle between vessel segments
   - Type of nodes (crossing, bifurcation, high curvature, meeting or terminal points)
5. Display of bifurcation geometrical features for each individual node
6. Availability of a follow mouse tool using a second display window for comparison purposes (Figure 6.1(b))
7. Generation of reports in PDF or Excel file (Figure 6.1(c))
8. Tools for manual modification of several calculated results, namely for changing
   - ODC location
   - OD radius value
   - ROI delimitation
   - Vessel segments A/V classification
   - Number of nodes in the graph

6.2 Evaluation Results

In this section, the experiments performed to test the RetinaCAD system for AVR computation are described and the main results are summarized. It is worth mentioning that the system requires no parameters setting for different datasets since all the parameters are adapted to the image resolution and camera FOV. The system is now evaluated on a new dataset from a local hospital which is described in the following subsection.

6.2.1 Material

The system was evaluated using the images of a dataset from Centro Hospitalar São João (CHSJ dataset). This dataset contains 564 images from 141 subjects, where for each subject there are four images, two from the right eye and two from the left eye; the two images of each eye were acquired with two different FOV values (45° and 30°). All the images are optic disc-centered and the ones with 30° FOV have resolution of 1444×1444 pixels and the resolution of images with 45° FOV is 2196 ×1958 pixels.

The average age of the subjects in this study is 60 in the range between 19 and 81 years. 53% of subjects are female while 47% are male. The clinical information is also available for this dataset, namely blood pressure, diabetic status, grades of diabetic, hypertensive and vascular retinopathy. The clinical information and images in this dataset are anonymized and there is informed consent from the individuals.

The images were used for investigating the robustness of the system to the use of distinct images of the same subject, through the assessment of the correlation between measurements from images of the right and left eyes and from images of same eye with different FOV. Some of clinical information is also used for system validation.

6.2.2 Experimental Validation

For the 564 images from CHSJ dataset that were analysed using RetinaCAD, the results for 27 images (less than 5% of all images) were not accepted as a consequence of errors in vessel segmentation, A/V classification and OD segmentation in images with no discernible OD or in images with severe pathological conditions. Figure 6.2 shows some images from this dataset where the RetinaCAD system fails to calculate the measurements correctly.

Although some of these errors can be solved using the manual modification tool which is included in this application, all the images of the subjects where the automatic procedures have

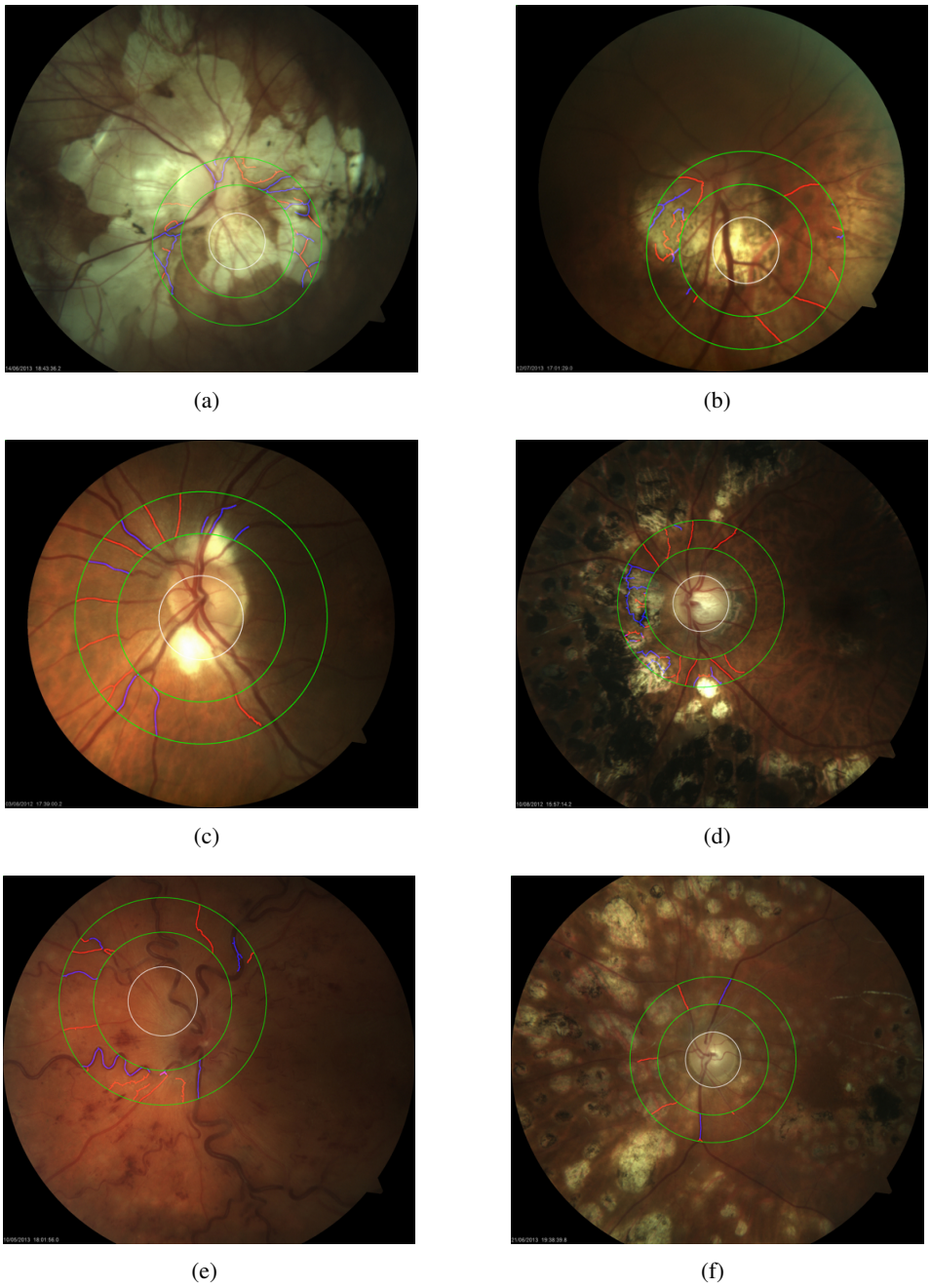

(a) (b) (c) (d) (e) (f)

Figure 6.2: Example images from CHSJ dataset where the RetinaCAD system fails.

failed (11 subjects) were manually excluded. In the following, the results are obtained for 520 images from 130 subjects.

Some results of A/V classification inside the ROI and obtained AVR values for images this dataset are shown in Figure 6.3. Although there are some differences between the results of A/V classification for the small vessels in the images of same subject, the obtained AVR values are similar.

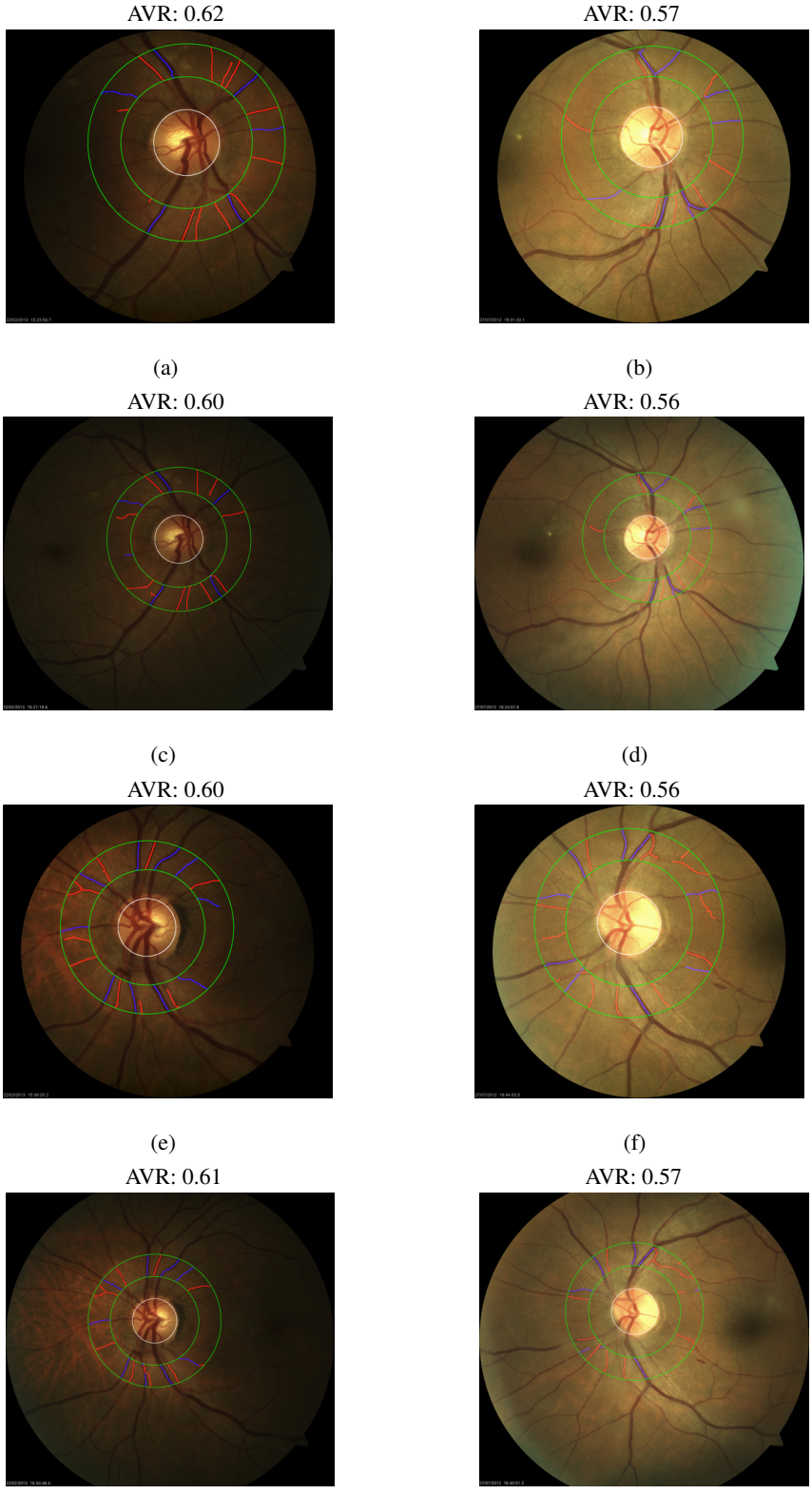

Figure 6.3: Examples of obtained AVR values and AV classification results inside the ROI for different images of 2 subjects from CHSJ dataset; each column shows the results for each subject; (a), (b) results for right eye with 30° FOV; (c), (d) results for right eye with 45° FOV; (e), (f) results for left eye with 30° FOV; (g), (h) results for left eye with 45° FOV; (Green circles: ROI delimitation, White circle: estimated OD, Red: arteries, Blue: veins).

Table 6.1 shows the mean and the standard deviation (SD) of the CRAE, CRVE and AVR values for the right and left eyes with different FOVs, separately. Table 6.2 shows the mean values for right and left eyes with both FOVs of 45° and 30°, and also the values for images of different FOVs for both right and left eyes. As illustrated in Figure 6.4, the differences between the mean AVR values for different eyes and different FOVs are small.

Table 6.1: Comparison of Mean ± SD (Min - Max) of measurements for different eyes (right and left) and different FOV (45° and 30°).

Measurements		Right eye		Left eye	
		FOV: 45°	FOV: 30°	FOV: 45°	FOV: 30°
Number of images		130	130	130	130
CRAE (*px*)	Mean ± SD	22.98 ± 2.94	23.27 ± 2.97	23.20 ± 3.24	23.21 ± 2.75
	(min - max)	(16.4 - 36.12)	(14.43 - 37.94)	(12.14 - 33.12)	(14.92 - 34.94)
CRVE (*px*)	Mean ± SD	36.96 ± 4.00	37.09 ± 4.07	37.21 ± 4.51	36.84 ± 3.54
	(min - max)	(20.06 - 45.26)	(23.97 - 48.92)	(16.41 - 59.14)	(22.27 - 48.06)
AVR	Mean ± SD	0.63 ± 0.10	0.63 ± 0.09	0.63 ± 0.08	0.63 ± 0.09
	(min - max)	(0.45 - 0.91)	(0.42 - 0.91)	(0.42 - 0.83)	(0.49 - 0.89)

Table 6.2: Comparison of Mean ± SD (Min - Max) of measurements for different eyes (right and left) with both FOVs of 45° and 30° and different FOVs (45° and 30°) for both right and left eyes.

Measurements		Both FOVs: 45° and 30°		Both left and right eyes	
		Right eye	Left eye	FOV: 45°	FOV: 30°
Number of images		260	260	260	260
CRAE (*px*)	Mean ± SD	23.12 ± 2.95	23.21 ± 3.00	23.09 ± 3.09	23.24 ± 2.86
	(min - max)	(14.43 - 37.94)	(12.14 - 34.94)	(12.14 - 36.12)	(14.43 - 37.94)
CRVE (*px*)	Mean ± SD	37.00 ± 4.11	37.02 ± 4.05	37.07 ± 4.34	36.96 ± 3.82
	(min - max)	(15.46 - 48.92)	(16.41 - 59.19)	(15.46 - 59.19)	(22.27 - 48.92)
AVR	Mean ± SD	0.63 ± 0.09	0.63 ± 0.09	0.63 ± 0.09	0.63 ± 0.09
	(min - max)	(0.42 - 0.91)	(0.38 - 0.89)	(0.42 - 0.91)	(0.42 - 0.91)

In order to evaluate the robustness of the methods in RetinaCAD, the results of the AVR values in images of the same eye that were acquired with a different FOV (45° and 30°) are compared. A mean error of 0.05 was achieved for the estimated AVR value when the 45° FOV and 30° FOV images were compared. For the same set of images, the Pearson's correlation coefficient, Pearson's test p-value and Spearman's rank correlation coefficient for AVR values are shown in Table 6.3.

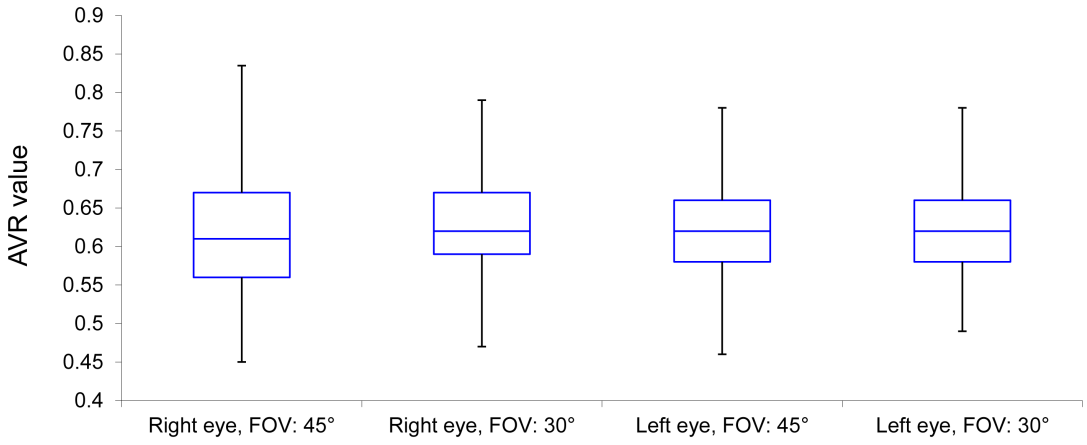

Figure 6.4: Boxplot of AVR values for different eyes (right and left) and different FOV (45° and 30°).

Spearman's correlation coefficient (ρ) measures the strength and direction of the relationship between two variables. It differs from Pearson's correlation only in that the computations are done after the numbers are converted to ranks. The ρ values for right and left eyes are equal to 0.63 and 0.66. By normal standards, the association between the two measurements would be considered statistically significant.

As can be observed, the Pearson's test p-value is smaller than 0.00001 and there is a substantial correlation between images of the same eye that were acquired in distinct conditions, thus indicating the consistency of the results obtained with RetinaCAD.

Table 6.3: Comparison of AVR values between images of the same eye with 45° and 30° FOV.

	Number of image pairs	AVR Mean error ± SD	Pearson's correlation coefficient	Pearson's test p-value	Spearman's rank correlation coefficient
Right eye - FOVs: 30° vs 45°	130	0.05 ± 0.04	0.78	< 0.00001	0.63
Left eye - FOVs: 30° vs 45°	130	0.04 ± 0.04	0.77	< 0.00001	0.66
All - FOVs: 30° vs 45°	260	0.05 ± 0.04	0.78	< 0.00001	0.64

The mean error and the correlation coefficients between measurements from the right and left eyes in the CHSJ dataset are shown in Table 6.4, where also included. These results show a moderate correlation between right and left eyes for AVR, which is similar to those reported Beaver Dam Eye Study (BDES) [135] and in the study by Leung *et al.* [136]. In these studies, the Pearson's correlation coefficients between AVR values from right and left eyes were obtained equal to 0.49 and 0.54, respectively.

Table 6.4: Comparison of AVR values between images right and left eyes.

	Number of image pairs	AVR Mean error ± SD	Pearson's correlation coefficient	Pearson's test p-value	Spearman's rank correlation coefficient
30° FOV - left vs right	130	0.06 ± 0.06	0.56	< 0.00001	0.43
45° FOV - left vs right	130	0.06 ± 0.06	0.55	< 0.00001	0.41
All - left vs right	260	0.06 ± 0.06	0.56	< 0.00001	0.42

The agreements between AVR values from images with different FOVS, and between right and left eyes can be observed in the Bland-Altman plots depicted in Figure 6.5 and Figure 6.6. Each plot shows the mean of two AVR values against the difference between them and allows a visual assessment of the distribution of errors. The scatter plots showing the correlation for all AVR values are also depicted in Figure 6.7.

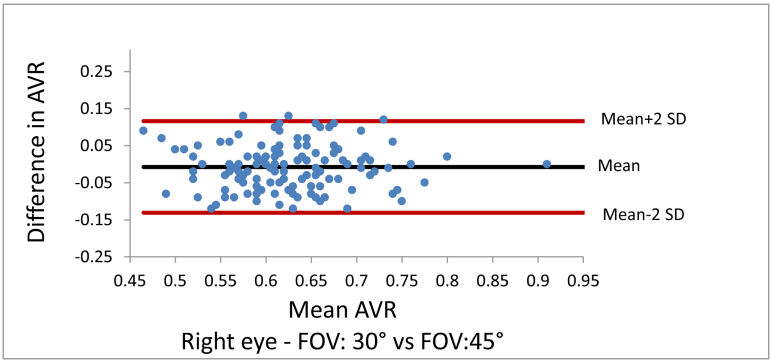

(a)

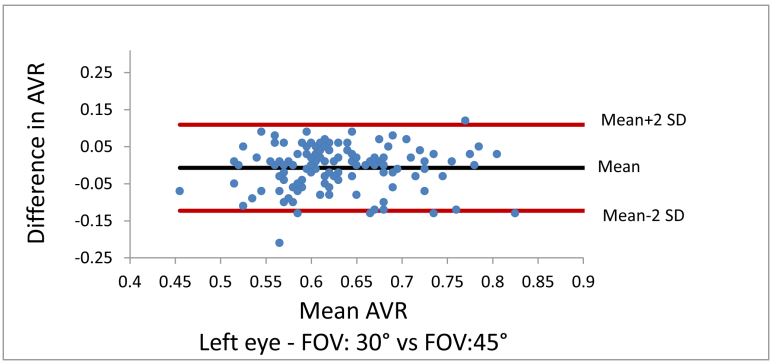

(b)

Figure 6.5: Bland-Altman plots of the agreement between AVR values from the same eye with 45° and 30° FOV for (a) right eyes; (b) left eyes.

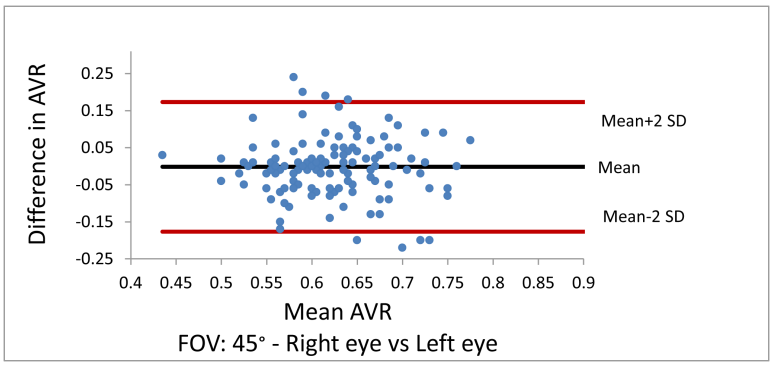

(a)

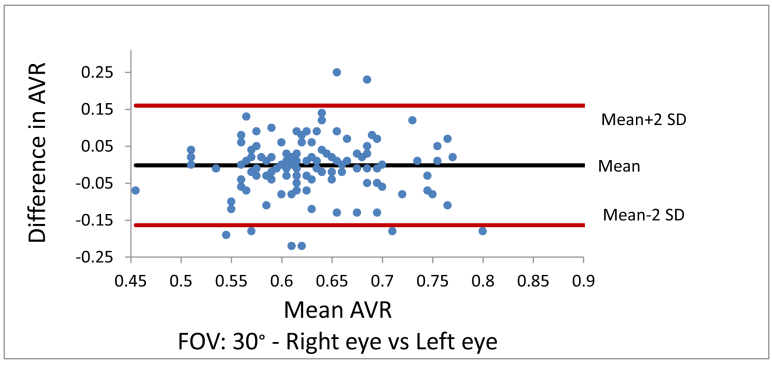

(b)

Figure 6.6: Bland-Altman plots of the agreement between AVR values from right and left eyes for (a) images with 45° FOV; (b) images with 30° FOV.

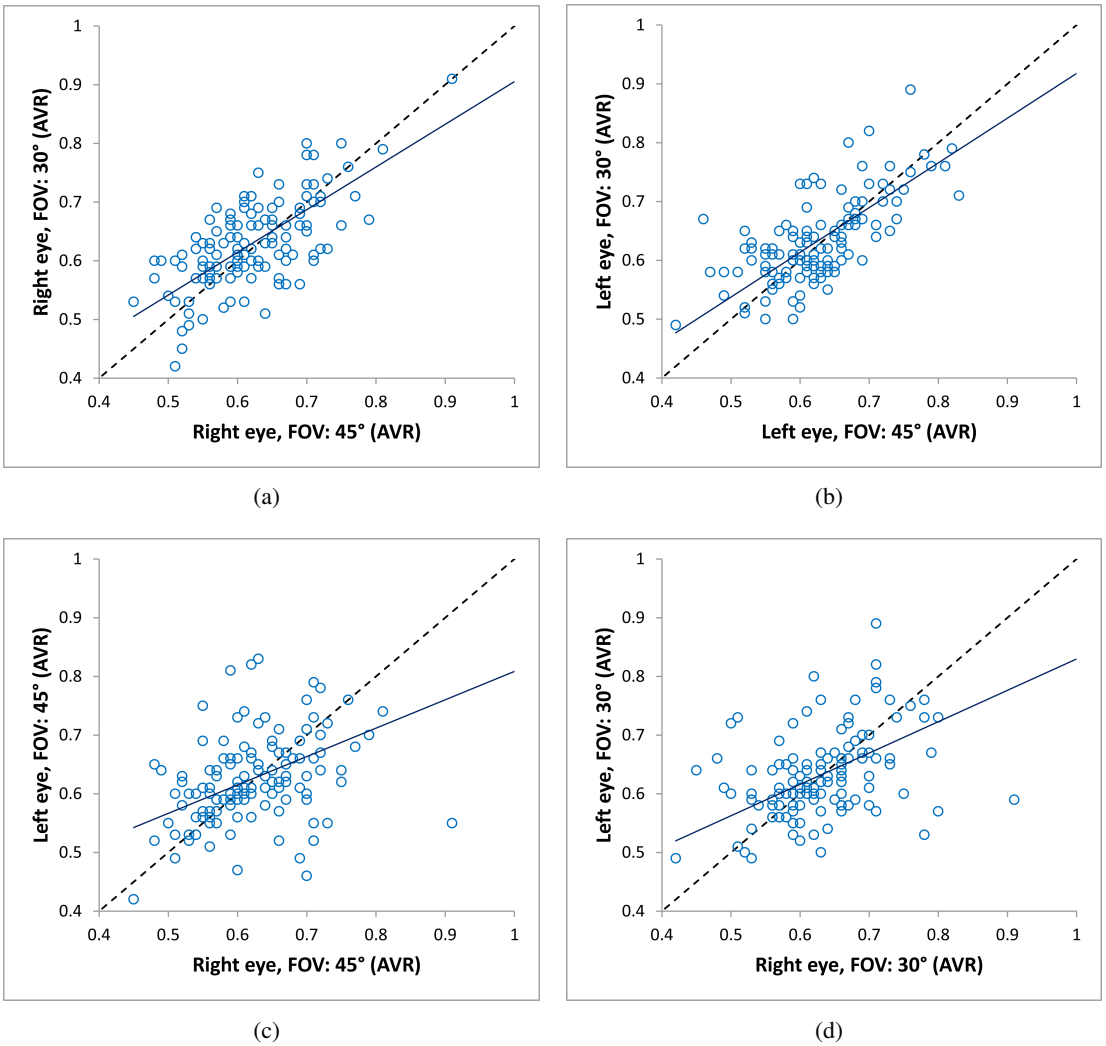

Figure 6.7: Scatter plots and regression lines for AVR values of the same eye with 45° and 30° FOV for (a) right eyes; (b) left eyes; and for AVR values from right and left eyes for (c) images with 45° FOV; (d) images with 30° FOV.

6.2.3 Clinical Validation

The proposed AVR methodology included in RetinaCAD is compared with some clinical information. Table 6.5 shows the relation between the mean and standard deviation (SD) of AVR values for 130 subjects with available medical information. The AVR values for right and left eyes and also the average value of both eyes from the images with 30° FOV are compared with the medical status of subjects such as risk of diabetes and other pathological conditions.

The subjects are categorized in different groups based on their pathological status. For each category, the mean and standard deviation of AVR values are obtained. The 95% confidence interval (CI) for the AVR values of each category are also included in table. The lower and upper limits of 95% CI of AVR values for each category are calculated using equations (6.6) and (6.7), respectively.

$$\text{Lower 95\% limit} = \bar{x} - 1.96 \times \frac{\sigma}{\sqrt{n}} \tag{6.6}$$

$$\text{Upper 95\% limit} = \bar{x} + 1.96 \times \frac{\sigma}{\sqrt{n}} \tag{6.7}$$

where $\bar{x}$ is the mean AVR value, σ represents the standard deviation and n is the number of subjects in each category.

The AVR values for the categories of subjects with diabetes, diabetic retinopathy, hypertensive retinopathy and vascular retinopathy are compared in this table. In the last two rows of Table 6.5 the subjects are categorized in two groups based on all mentioned pathological conditions and their blood pressure (BP). The subjects with systolic BP higher than 140 mm Hg or diastolic BP higher than 90 mm Hg are considered as the ones with high blood pressure. The number of subjects with high BP is 41, while the rest of subjects have normal BP.

Although there is a considerable overlap between the measurements, due to uncertainty of the measurement given by the SD, the average of AVR values for the categories of subjects with these diseases are smaller than the average of AVR values for the subject with non-pathological conditions.

As can be observed in this table, the mean AVR value of 0.66 (95% CI: 0.64 - 0.68) in the non-pathological subjects with normal BP is higher than other group with pathological and/or high BP with mean AVR value of 0.62 (95% CI: 0.61 - 0.63), which shows evidence that the measurements

obtained for AVR are consistent with the expected association of the AVR value with the risk of systemic diseases and hypertension.

Figure 6.8 shows the mean of AVR values and 95% confidence interval for each category of subjects. Red color represents the categories with pathological conditions and green color indicates the non-pathological categories. Figure 6.8(a) and Figure 6.8(b) represent the AVR values for right and left eyes, respectively, while the average of AVR values from both eyes for each category are illustrated in Figure 6.8(c).

Table 6.5: Average of AVR values and 95% confidence intervals for the subjects with different pathological conditions.

Pathological status	Number of subjects	AVR (Mean ± SD) [95% CI]		
		Right eye	Left eye	Average of both eyes
Diabetes	58	0.61 ± 0.08 [0.59 - 0.63]	0.62 ± 0.06 [0.60 - 0.63]	0.62 ± 0.06 [0.60 - 0.63]
Diabetic retinopathy	21	0.63 ± 0.10 [059 - 0.67]	0.60 ± 0.06 [0.58 - 0.63]	0.62 ± 0.07 [0.59 - 0.65]
Hypertensive retinopathy	63	0.61 ± 0.09 [0.59 - 0.63]	0.62 ± 0.07 [0.60 - 0.63]	0.61 ± 0.06 [0.60 - 0.63]
Vascular retinopathy	69	0.61 ± 0.08 [0.59 - 0.63]	0.62 ± 0.07 [0.60 - 0.63]	0.61 ± 0.06 [0.60 - 0.63]
Pathological or high BP	102	0.62 ± 0.08 [0.61 - 0.64]	0.62 ± 0.07 [0.61 - 0.64]	0.62 ± 0.06 [0.61 - 0.63]
Non-pathological and normal BP	28	0.66 ± 0.06 [0.64 - 0.69]	0.65 ± 0.08 [0.62 - 0.68]	0.66 ± 0.06 [0.64 - 0.68]

BP: Blood Pressure

CI: Confidence Interval

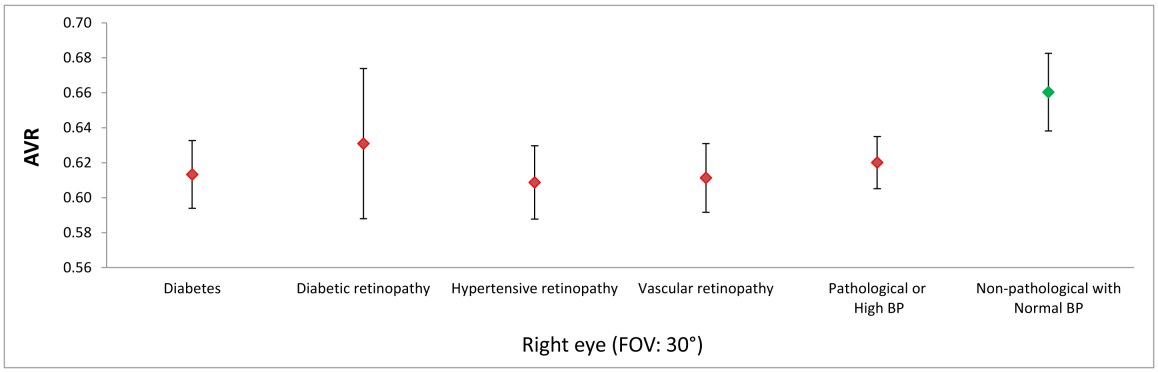

(a)

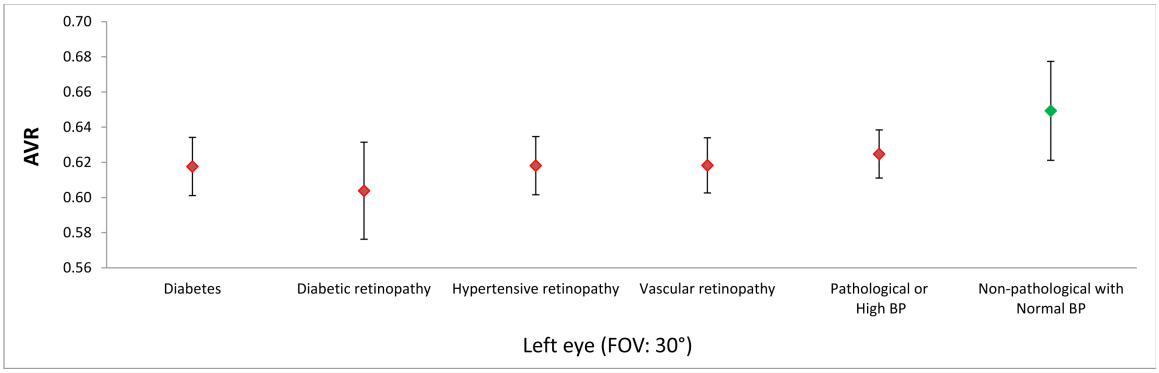

(b)

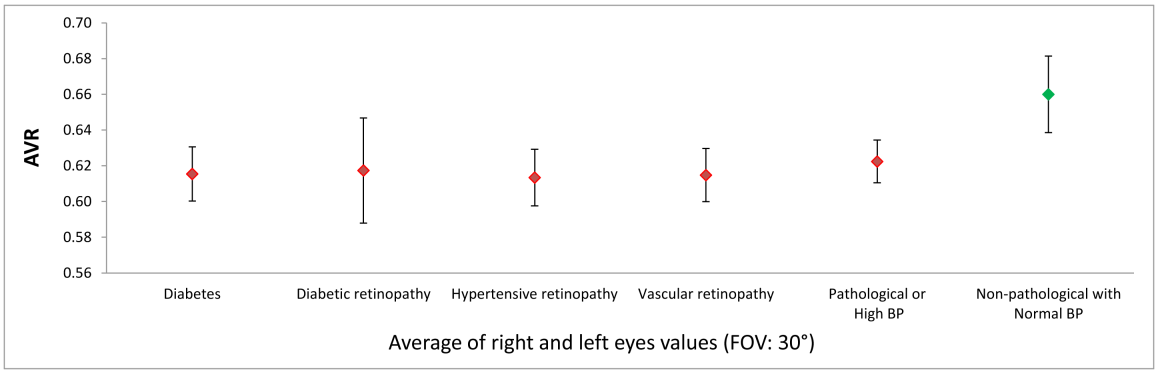

(c)

Figure 6.8: The average of AVR values with 95% confidence intervals for the subjects with different pathological status (a) Right eye; (b) Left eye; (c) Average of right and left eyes values.

6.3 Concluding Remarks

In this chapter, a user-friendly system, RetinaCAD is introduced which is capable of automatic detection, measurement and classification two main retinal landmarks, the optic disc and the vessels. RetinaCAD can measure several vascular features that are recognized as indicators for some prevalent systemic diseases.

This application was assessed in the images of the CHSJ dataset, where it showed a relation between obtained AVR values and pathological status of 130 subjects. The lower AVR values in the people with diabetic, retinopathy conditions or high blood pressure in contrast to the non-pathological ones with normal blood pressure demonstrates the potential and usefulness of this system as a CAD tool for early detection and follow-up of diabetes, hypertension or cardiovascular pathologies. After comparing the measured AVR values for images of the same eye but with different FOV, a substantial correlation and a low mean error were achieved, thus allowing the conclusion that RetinaCAD is adequate both for research and for general clinical use.

The evaluation of system on new datasets is still a challenge and there are still several issues and problems that need to be resolved.

Chapter 7

Conclusions and Future Work

7.1 Summary and Conclusions

This thesis dealt with the development of automated retinal image analysis methods for the assessment of signs related with the changes in vessels calibers caused by several pathologies such as diabetes, hypertension, cerebovascular and cardiovascular diseases. Among several retinal vascular signs, Arteriolar-to-Venular Ratio (AVR) is a well known health biomarker and there is a strong need to develop an automated system for an accurate and reproducible estimation of AVR which requires different image analysis tools, namely vessel segmentation, vessel caliber estimation, optic disc (OD) segmentation and artery/vein (A/V) classification.

This work was mostly focused on the development of methodologies for OD segmentation, A/V classification and automated calculation of the AVR value which are integrated in the RetinaCAD system with a potential for clinical applications. The starting point of this work was based on a vessel segmentation method previously developed by our research group. Some parts of this work are already published in peer-reviewed journals and presented in the different conferences. The list of related publications are included in Appendix B.

AVR is estimated from the calibers of the vessels inside a specific region of interest (ROI), defined as the standard ring area around the OD. As a consequence, both the localization of the optic disc center and its diameter are required for automating the AVR calculation. For this reason, we proposed a new automatic method for OD segmentation using a multiresolution sliding band filter. The evaluation results on the images of three datasets demonstrate the better performance of the proposed method compared to recently published OD segmentation approaches and prove the independence of this method from changes in image characteristics such as size, quality and

camera field of view. Our approach is also able to produce useful results even in the presence of severe pathological conditions which shows the robustness of the SBF-based approach in the presence of diabetic retinopathy and risk of macular edema.

We also presented a new automatic method for A/V classification based on the analysis of a graph extracted from the retinal vasculature. The proposed approach classifies the entire vascular tree through the combination of structural information with vessel intensity information, while most of the recent methods mainly use intensity features for discriminating between arteries and veins. Our method is evaluated using manual labeling for three public databases. The results demonstrate that this method outperforms recent approaches for A/V classification. On the other hand, the high accuracy achieved especially for the largest arteries and veins, confirm that this A/V classification methodology is reliable for the calculation of AVR and other indicators associated with vascular alterations.

An automatic approach for the estimation of AVR in retinal images was introduced in this work. The proposed method includes new solutions for the OD segmentation and A/V classification. This method was evaluated using the images of the INSPIRE-AVR dataset. The low mean error of the measured AVR with respect to the reference ones were identical to the one achieved by a medical expert using a semi-automated system, thus demonstrating the reliability of the proposed solution for AVR estimation.

Finally, the developed approaches are integrated in RetinaCAD, a system for the fast, reliable and automatic measurement of CRAE, CRVE, and AVR values, as well as several geometrical features of the retinal vasculature. RetinaCAD automatically identifies important landmarks in the retina, such as the blood vessels and optic disc, and performs artery/vein classification and vessel width measurement. The system is validated on a new dataset from local hospital and the results of AVR estimation shown a substantial correlation between images of same eye acquired with different camera fields of view. The clinical validation on the estimated AVR values showed a lower value in subjects with diabetes or pathological conditions in contrast with subjects with non-pathological conditions which gives some confidence on the potential of the system as a CAD tool for early detection and follow-up of diabetes, hypertension or other cardiovascular pathologies. However, we are aware that this needs extensive validation on much larger datasets in order to increase the degree of confidence and to have a good generalization of the results achieved so far.

7.2 Future Directions

The overall investigation in this thesis has shown the usefulness of the RetinaCAD system and the proposed approaches for OD segmentation and A/V classification, as well as the methodology for the assessment of vascular changes particularly the computation of AVR values. However there is still great possibilities for the improvement of medical image analysis tools based on the needs and trends of different applications. Moreover, RetinaCAD still needs a more extensive validation on much larger datasets in order to increase the degree of confidence and to have a good generalization of the results achieved so far.

As earlier described, a new graph-based method is proposed for the classification of vessels as arteries or veins. Since the extracted graph represents the vascular tree, it can be useful for identifying different vascular signs such as vascular bifurcation angles, branching patterns and fractal based features which can have significant impact on the early detection of several systemic diseases.

On the other hand, with the development of image analysis methods for assessing retinal vascular changes, there is a large demand for fast and fully-automatic algorithms to register two or more retinal images which were taken at different times and from different views. Accurate and fast registration of retinal images is still a challenging problem since the low content contrast, large intensity variance as well as various pathologies caused deterioration in retinal images. For this reason, we expect that the graph representation of the vascular structure could be also a valuable contribution for the development of an efficient registration method.

In the proposed unsupervised approach for the assignment of A/V classes to the labels of each subgraph, only one feature (red intensity) is used in the k-means clustering algorithm. It would be interesting to see the performance of this unsupervised technique using other features, such as green component, hue and intensity.

From the clinical point of view, further studies are needed with more patients in a long duration follow-up diagnosis programme. In this work only the AVR values are used for the clinical validation and it would be interesting to investigate the relationship of obtained CRAE, CRVE and bifurcation geometrical features with clinical information. Furthermore, there are other retinal vascular signs which can provide clinically useful information to aid prevention and management of systemic diseases. Some of these retinal vascular signs are tortuosity, branching patterns, fractal geometrical features, focal arteriolar narrowing and arteriolar color changes.

We believe that RetinaCAD is a remarkable step toward developing an automated retinal computer-aided diagnosis system. One main goal as future work on the RetinaCAD system, can be the implementation of more retinal image analysis tools for the measurement of other retinal vascular signs which can provide several opportunities for further research.

Appendix A

Materials

This Appendix summarizes the features of the retinal image datasets which are used for the evaluation of different retinal image analysis algorithms. These datasets were created by several research groups and are publicly available [105, 110, 111, 137–141]. The specifications of the datasets that are described in this appendix are shown in Table A.1.

Table A.1: Datasets specifications.

Dataset name	Number of images	Image size	FOV	Available ground truth
STARE	20	700 × 605 px	35°	Vessel segmentation
DRIVE	40	565 × 584 px	45°	Vessel segmentation Artery/vein classification
VICAVR	58	768 × 576 px	-	Artery/vein classification
INSPIRE-AVR	40	2392 × 2048 px	30°	AVR value Artery/vein classification Optic disc segmentation
MESSIDOR	1200	1440 × 960 px 2240 × 1488 px 2304 × 1536 px	45°	Risk of macular edema grade Diabetic retinopathy grade Optic disc segmentation
ONHSD	99	760 × 570 px	45°	Optic disc segmentation

A.1 STARE Dataset

The STARE dataset consists of 20 images for blood vessel segmentation [137]. These retinal images were captured using a TopCon TRV-50 fundus camera at 35° field of view, and afterwards digitized to 700×605 pixels, 8 bits per RGB channel. Two observers manually segmented all the images.

A.2 DRIVE Dataset

The DRIVE (Digital Retinal Images for Vessel Extraction) is a publicly available dataset for the comparison of vessel segmentation methods in retinal images [110]. It consists of 40 images which were captured with 565×584 pixels, with 8 bits per color plane using a Cannon CR5 non-mydriatic 3CCD camera with a 45° field of view. The images in this dataset are randomly selected from 400 diabetic subjects that participated in a diabetic retinopathy screening program. From the 40 selected image, 33 images do not show diabetic signs, whereas 7 images have signs of mild early diabetic retinopathy.

The images have been grouped into a training set and a test set both containing 20 images. For the training set, there is a manual segmentation available, and for the test set, two manual segmentations are available. One manual segmentation is used as the standard reference, the second one is used to compare the segmentation result of image analysis algorithms with those of the second human observer. The manual artery/vein labeling was performed by an expert on the 20 images of the DRIVE test set and is available for download from the RetinaCAD website [141].

A.3 VICAVR Dataset

The VICAVR dataset is a set of 58 retinal images for the computation of AVR values [138]. The images were acquired using a TopCon non-mydriatic camera NW-100 model with a spatial resolution of 768×584, and are optic disc-centered.

The VICAVR dataset includes the caliber of the vessels measured at different radii from the optic disc, as well as the vessel type (artery/vein) labeled by three experts. From 3816 vessel segments, three experts classified 2471, 2778, and 2943 vessels into artery and vein classes.

A.4 INSPIRE-AVR Dataset

The 40 high resolution images of the INSPIRE-AVR database have 2392×2048 pixels and are optic disc-centered [111]. All images were obtained using a 30° Zeiss fundus camera. This dataset includes two AVR measures that were computed by two ophthalmologists using a semi-automated computer program, IVAN, developed at the University of Wisconsin. The AVR estimates of Observer 1 are used as reference for calculating the errors for the results of both Observer 2 and AVR calculation methods.

The manual OD segmentation and also the manual artery/vein labeling for this dataset is available for download from the RetinaCAD website [141]. The OD boundary of each image was approximated by an ellipse fitted to 16 points marked up by an expert.

A.5 MESSIDOR Dataset

The MESSIDOR dataset is a large publicly available for evaluating the computer-assisted diagnoses of diabetic retinopathy [139]. This dataset contains 1200 eye fundus color images acquired using a Topcon TRC NW6 non-mydriatic retinograph with a 45° FOV. 800 of these images were captured with pupil dilation and 400 without dilation. The images are 1440×960, 2240×1488, or 2304×1536 pixels in size and 8 bits per color plane.

In the MESSIDOR dataset, there are several images from patients affected by diabetic retinopathy (DR) and macular edema (ME). This dataset contains information regarding DR and the risk of ME grading. The retinopathy grades (Normal, D1, D2 and D3) are obtained based on the number of microaneurysms, hemorrhages and neovascularization. The risk of macular edema is graded as Normal and two risk levels measuring the shortest distance between macula and hard exudates. The OD boundary was manually delimited by experts at the University of Huelva [105], and used as a gold standard for the evaluation of optic disc segmentation methods.

A.6 ONHSD Dataset

The ONHSD (Optic Nerve Head Segmentation Database) contains 99 images with resolution of 760×570 pixels and 8 bits per color plane. The images were captured using a Canon CR6 45MNf fundus camera, with a field view of 45°. The 99 images were taken from 50 subjects randomly sampled from a diabetic retinopathy screening program where 96 images have a recognizable optic disc. 19 subjects have type 2 diabetes, while the risk of diabetes for the remaining 31 was unavailable.

The standard reference for this dataset was provided by experts at the University of Lincoln [140]. The ODC has been marked up by a clinician and four clinicians marked the OD boundary on the radial spokes (at 15 degree angles) radiating from the nominated centre.

Appendix B

Publications

B. Dashtbozorg, A. M. Mendonça, A. Campilho, "An Automatic Graph-Based Approach for Artery/Vein Classification in Retinal Images," Image Processing, IEEE Transactions on , vol.23, no.3, pp.1073-1083, March 2014. DOI: 10.1109/TIP.2013.2263809

B. Dashtbozorg, A. M. Mendonça, A. Campilho, "Optic Disc Segmentation using the Sliding Band Filter," Computers in Biology and Medicine, vol. 56, pp. 1-12, 2015. DOI: 10.1016/j.compbiomed.2014.10.009

B. Dashtbozorg, A. M. Mendonça, A. Campilho, "Assessment of Retinal Vascular Changes through Arteriolar-to-Venular Ratio Calculation," International Conference on Image Analysis and Recognition, 2015 (accepted for publication).

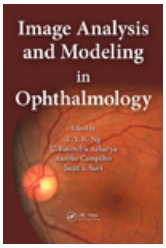

A.M. Mendonça, B. Dashtbozorg, A. Campilho, "Segmentation of the vascular network of the retina," in Image Analysis and Modeling in Ophthalmology, E. Y. K. Ng, U. R. Acharya, A. Campilho and J. S. Suri, Eds. CRC Press, pp. 85-109, 2014. DOI: 10.1201/b16510-6

B. Dashtzbozorg, A.M. Mendonça, S. Penas, A. Campilho, "Computer-aided diagnosis system for the assessment of retinal vascular changes," in Proceedings of the Ophthalmic Medical Image Analysis First International Workshop, OMIA 2014, Held in Conjunction with MICCAI 2014, Boston, pp. 9-16, September 2014.

B. Dashtbozorg, A. M. Mendonça, S. Penas, A. Campilho, "RetinaCAD, a system for the assessment of retinal vascular changes," Engineering in Medicine and Biology Society (EMBC), Annual International Conference of the IEEE, Chicago, USA, 2014. DOI:10.1109/MPUL.2014.2316040

B. Dashtbozorg, A. M. Mendonça, A. Campilho, "Assessment of vascular changes in retinal images," Medical Measurements and Applications (MeMeA), 2014 IEEE International Symposium on, pp. 1-4, 11-12 June 2014. DOI: 10.1109/MeMeA.2014.6860023

B. Dashtbozorg, A. M. Mendonça, A. Campilho, "An automatic method for the estimation of Arteriolar-to-Venular Ratio in retinal images," Computer-Based Medical Systems (CBMS), 2013 IEEE 26th International Symposium on, pp. 512-513, 20-22 June 2013. DOI: 10.1109/CBMS.2013.6627854

B. Dashtbozorg, A. M. Mendonça, A. Campilho, "Automatic Estimation of the Arteriolar-to-Venular Ratio in Retinal Images Using a Graph-based Approach for Artery/Vein Classification," Image Analysis and Recognition, LNCS, vol. 7950 , pp. 530-538, 2013. DOI: 10.1007/978-3-642-39094-4_60

B. Dashtbozorg, A. M. Mendonça, A. Campilho, "Automatic Classification of Retinal Vessels Using Structural and Intensity Information", Pattern Recognition and Image Analysis, LNCS, vol. 7887, pp. 600-607, 2013. DOI: 10.1007/978-3-642-38628-2_71

References

[1] Thanh Tan Nguyen, Jie Jin Wang, and Tien Yin Wong. Retinal vascular changes in pre-diabetes and prehypertension new findings and their research and clinical implications. *Diabetes Care*, 30(10):2708–2715, 2007.

[2] Tien Yin Wong, Aruna Kamineni, Ronald Klein, A Richey Sharrett, Barbara E Klein, David S Siscovick, Mary Cushman, and Bruce B Duncan. Quantitative retinal venular caliber and risk of cardiovascular disease in older persons: the cardiovascular health study. *Archives of internal medicine*, 166(21):2388–2394, 2006.

[3] Aljoscha S Neubauer, Matthias Luedtke, Christos Haritoglou, Siegfried Priglinger, and Anselm Kampik. Retinal vessel analysis reproducibility in assessing cardiovascular disease. *Optometry & Vision Science*, 85(4):E247–E254, 2008.

[4] International Diabetes Federation (IDF). http://www.idf.org/, 2014.

[5] Ronald Klein, Stacy M Meuer, Scot E Moss, and Barbara EK Klein. Retinal microaneurysm counts and 10-year progression of diabetic retinopathy. *Archives of Ophthalmology*, 113(11):1386–1391, 1995.

[6] Kit Guan, Chris Hudson, Tien Wong, Mila Kisilevsky, Ravi K Nrusimhadevara, Wai Ching Lam, Mark Mandelcorn, Robert G Devenyi, and John G Flanagan. Retinal hemodynamics in early diabetic macular edema. *Diabetes*, 55(3):813–818, 2006.

[7] World Health Organization (WHO). http://www.world-heart-federation.org, 2014.

[8] Ana Maria Mendonça and Aurelio Campilho. Segmentation of retinal blood vessels by combining the detection of centerlines and morphological reconstruction. *Medical Imaging, IEEE Transactions on*, 25(9):1200–1213, 2006.

[9] Behdad Dashtbozorg, Ana Maria Mendonça, and Aurélio Campilho. Optic disc segmentation using the sliding band filter. *Computers in biology and medicine*, 56(0):1 – 12, 2015.

[10] Behdad Dashtbozorg, Ana Maria Mendonça, and Aurélio Campilho. An automatic graph-based approach for artery/vein classification in retinal images. *Image Processing, IEEE Transactions on*, 23(3):1073–1083, 2014.

[11] Behdad Dashtbozorg, Ana Maria Mendonça, and Aurélio Campilho. An automatic method for the estimation of arteriolar-to-venular ratio in retinal images. In *Computer-Based Medical Systems (CBMS), 2013 IEEE 26th International Symposium on*, pages 512–513. IEEE, 2013.

[12] Behdad Dashtbozorg, Ana Maria Mendonca, and Aurelio Campilho. Assessment of vascular changes in retinal images. In *Medical Measurements and Applications (MeMeA), 2014 IEEE International Symposium on*, pages 1–4. IEEE, 2014.

[13] Behdad Dashtbozorg, Ana Maria Mendonca, Susana Penas, and Aurelio Campilho. Retinacad, a system for the assessment of retinal vascular changes. In *Engineering in Medicine and Biology Society (EMBC), 2014 36th Annual International Conference of the IEEE*, pages 6328–6331. IEEE, 2014.

[14] Herbert Jelinek. *Automated image detection of retinal pathology*. CRC Press, 2009.

[15] Cemil Kirbas and Francis Quek. A review of vessel extraction techniques and algorithms. *ACM Computing Surveys (CSUR)*, 36(2):81–121, 2004.

[16] Muhammad Moazam Fraz, P Remagnino, Andreas Hoppe, Bunyarit Uyyanonvara, Alicja R Rudnicka, Christopher G Owen, and Sarah A Barman. Blood vessel segmentation methodologies in retinal images–a survey. *Computer methods and programs in biomedicine*, 108(1):407–433, 2012.

[17] Qin Li, Jane You, Lei Zhang, David Zhang, and Prabir Bhattacharya. A new approach to automated retinal vessel segmentation using multiscale analysis. In *Pattern Recognition, 2006. ICPR 2006. 18th International Conference on*, volume 4, pages 77–80. IEEE, 2006.

[18] Gunnar Läthén, Jimmy Jonasson, and Magnus Borga. Blood vessel segmentation using multi-scale quadrature filtering. *Pattern Recognition Letters*, 31(8):762–767, 2010.

[19] Elahe Moghimirad, Seyed Hamid Rezatofighi, and Hamid Soltanian-Zadeh. Retinal vessel segmentation using a multi-scale medialness function. *Computers in biology and medicine*, 42(1):50–60, 2012.

[20] Qin Li, Jane You, and David Zhang. Vessel segmentation and width estimation in retinal images using multiscale production of matched filter responses. *Expert Systems with Applications*, 39(9):7600–7610, 2012.

[21] Vahid Mohammadi Saffarzadeh, Alireza Osareh, and Bita Shadgar. Vessel segmentation in retinal images using multi-scale line operator and k-means clustering. *Journal of medical signals and sensors*, 4(2):122, 2014.

[22] A.M. Mendonça, B. Dashtbozorg, and A. Campilho. Segmentation of the vascular network of the retina. In E. Y. K. Ng, U. Rajendra Acharya, Aurelio Campilho, and Jasjit S. Suri, editors, *Image Analysis and Modeling in Opthalmology*, pages 85–109. CRC Press, 2014.

[23] Changhua Wu, Jennifer J Kang Derwent, and Peter Stanchev. Retinal vessel radius estimation and a vessel center line segmentation method based on ridge descriptors. *Journal of Signal Processing Systems*, 55(1-3):91–102, 2009.

[24] M Elena Martinez-Perez, Alun D Hughes, Alice V Stanton, Simon A Thom, Anil A Bharath, and Kim H Parker. Segmentation of retinal blood vessels based on the second directional derivative and region growing. In *Image Processing, 1999. ICIP 99. Proceedings. 1999 International Conference on*, volume 2, pages 173–176. IEEE, 1999.

[25] Saurabh Garg, Jayanthi Sivaswamy, and Siva Chandra. Unsupervised curvature-based retinal vessel segmentation. In *Biomedical Imaging: From Nano to Macro, 2007. ISBI 2007. 4th IEEE International Symposium on*, pages 344–347. IEEE, 2007.

[26] Michal Sofka and Charles V Stewart. Retinal vessel centerline extraction using multiscale matched filters, confidence and edge measures. *Medical Imaging, IEEE Transactions on*, 25(12):1531–1546, 2006.

[27] Girish Singh Ramlugun, Vivek Krishna Nagarajan, and Chandan Chakraborty. Small retinal vessels extraction towards proliferative diabetic retinopathy screening. *Expert Systems with Applications*, 39(1):1141–1146, 2012.

[28] Abdolhossein Fathi and Ahmad Reza Naghsh-Nilchi. Automatic wavelet-based retinal blood vessels segmentation and vessel diameter estimation. *Biomedical Signal Processing and Control*, 8(1):71–80, 2013.

[29] Michael Krause, Ralph Maria Alles, Bernhard Burgeth, and Joachim Weickert. Fast retinal vessel analysis. *Journal of Real-Time Image Processing*, pages 1–10, 2013.

[30] Marios Vlachos and Evangelos Dermatas. Multi-scale retinal vessel segmentation using line tracking. *Computerized Medical Imaging and Graphics*, 34(3):213–227, 2010.

[31] Meindert Niemeijer, Bram van Ginneken, and Michael D Abràmoff. A linking framework for pixel classification based retinal vessel segmentation. In *SPIE Medical Imaging*, pages 726216–726216. International Society for Optics and Photonics, 2009.

[32] Yi Yin, Mouloud Adel, and Salah Bourennane. Retinal vessel segmentation using a probabilistic tracking method. *Pattern Recognition*, 45(4):1235–1244, 2012.

[33] Erik Bekkers, Remco Duits, Tos Berendschot, and Bart ter Haar Romeny. A multi-orientation analysis approach to retinal vessel tracking. *Journal of Mathematical Imaging and Vision*, pages 1–28, 2014.

[34] Meindert Niemeijer, Joes Staal, Bram van Ginneken, Marco Loog, and Michael D Abramoff. Comparative study of retinal vessel segmentation methods on a new publicly available database. In *Medical Imaging 2004*, pages 648–656. International Society for Optics and Photonics, 2004.

[35] Joes Staal, Michael D Abràmoff, Meindert Niemeijer, Max A Viergever, and Bram van Ginneken. Ridge-based vessel segmentation in color images of the retina. *Medical Imaging, IEEE Transactions on*, 23(4):501–509, 2004.

[36] Joao VB Soares, Jorge JG Leandro, Roberto M Cesar, Herbert F Jelinek, and Michael J Cree. Retinal vessel segmentation using the 2-d gabor wavelet and supervised classification. *Medical Imaging, IEEE Transactions on*, 25(9):1214–1222, 2006.

[37] Carmen Alina Lupascu, Domenico Tegolo, and Emanuele Trucco. Fabc: retinal vessel segmentation using adaboost. *Information Technology in Biomedicine, IEEE Transactions on*, 14(5):1267–1274, 2010.

[38] Diego Marín, Arturo Aquino, Manuel Emilio Gegúndez-Arias, and José Manuel Bravo. A new supervised method for blood vessel segmentation in retinal images by using gray-level and moment invariants-based features. *Medical Imaging, IEEE Transactions on*, 30(1):146–158, 2011.

[39] S Wilfred Franklin and S Edward Rajan. Retinal vessel segmentation employing ann technique by gabor and moment invariants-based features. *Applied Soft Computing*, 22:94–100, 2014.

[40] Renzo Perfetti, Elisa Ricci, Daniele Casali, and Giovanni Costantini. Cellular neural networks with virtual template expansion for retinal vessel segmentation. *Circuits and Systems II: Express Briefs, IEEE Transactions on*, 54(2):141–145, 2007.

[41] Shuangling Wang, Yilong Yin, Guibao Cao, Benzheng Wei, Yuanjie Zheng, and Gongping Yang. Hierarchical retinal blood vessel segmentation based on feature and ensemble learning. *Neurocomputing*, 2014.

[42] Arturo Aquino, Manuel Emilio Gegúndez-Arias, and Diego Marín. Detecting the optic disc boundary in digital fundus images using morphological, edge detection, and feature extraction techniques. *IEEE Trans. Med. Imag.*, 29(11):1860–1869, 2010.

[43] DWK Wong, J Liu, JH Lim, X Jia, F Yin, H Li, and TY Wong. Level-set based automatic cup-to-disc ratio determination using retinal fundus images in ARGALI. In *Engineering in Medicine and Biology Society, 2008. EMBS 2008. 30th Annual International Conference of the IEEE*, pages 2266–2269. IEEE, 2008.

[44] Yuanjie Zheng, Dwight Stambolian, Joan O'Brien, and James C Gee. Optic disc and cup segmentation from color fundus photograph using graph cut with priors. In *Medical Image Computing and Computer-Assisted Intervention–MICCAI 2013*, pages 75–82. Springer, 2013.

[45] Andrea Giachetti, Lucia Ballerini, and Emanuele Trucco. Accurate and reliable segmentation of the optic disc in digital fundus images. *Journal of Medical Imaging*, 1(2):024001–024001, 2014.

[46] James Lowell, Andrew Hunter, David Steel, Ansu Basu, Robert Ryder, Eric Fletcher, and Lee Kennedy. Optic nerve head segmentation. *Medical Imaging, IEEE Transactions on*, 23(2):256–264, 2004.

[47] Juan Xu, Opas Chutatape, Eric Sung, Ce Zheng, and Paul Chew Tec Kuan. Optic disk feature extraction via modified deformable model technique for glaucoma analysis. *Pattern recognition*, 40(7):2063–2076, 2007.

[48] Huiqi Li and Opas Chutatape. Automated feature extraction in color retinal images by a model based approach. *Biomedical Engineering, IEEE Transactions on*, 51(2):246–254, 2004.

[49] G Joshi, Jayanthi Sivaswamy, and SR Krishnadas. Optic disk and cup segmentation from monocular color retinal images for glaucoma assessment. *Medical Imaging, IEEE Transactions on*, 30(6):1192–1205, 2011.

[50] Honggang Yu, E Simon Barriga, Carla Agurto, Sebastian Echegaray, Marios S Pattichis, Wendall Bauman, and Peter Soliz. Fast localization and segmentation of optic disk in retinal images using directional matched filtering and level sets. *Information Technology in Biomedicine, IEEE Transactions on*, 16(4):644–657, 2012.

[51] Hung-Kuei Hsiao, Chen-Chung Liu, Chun-Yuan Yu, Shiau-Wei Kuo, and Shyr-Shen Yu. A novel optic disc detection scheme on retinal images. *Expert Systems with Applications*, 39(12):10600–10606, 2012.

[52] Ahmed Wasif Reza, Chantra Eswaran, and Subhas Hati. Automatic tracing of optic disc and exudates from color fundus images using fixed and variable thresholds. *Journal of medical systems*, 33(1):73–80, 2009.

[53] Daniel Welfer, Jacob Scharcanski, and Diane Ruschel Marinho. A morphologic two-stage approach for automated optic disk detection in color eye fundus images. *Pattern Recognition Letters*, 34(5):476–485, 2013.

[54] Sandra Morales, Valery Naranjo, Jesús Angulo, and Mariano Alcañiz Raya. Automatic detection of optic disc based on pca and mathematical morphology. *IEEE transactions on medical imaging*, 32(4):786–796, 2013.

[55] Michael D Abramoff, Wallace LM Alward, Emily C Greenlee, Lesya Shuba, Chan Y Kim, John H Fingert, and Young H Kwon. Automated segmentation of the optic disc from stereo color photographs using physiologically plausible features. *Investigative ophthalmology & visual science*, 48(4):1665–1673, 2007.

[56] Jun Cheng, Jiang Liu, Yanwu Xu, Fengshou Yin, Damon Wing Kee Wong, Ngan-Meng Tan, Dacheng Tao, Ching-Yu Cheng, Tin Aung, and Tien Yin Wong. Superpixel classification based optic disc and optic cup segmentation for glaucoma screening. *Medical Imaging, IEEE Transactions on*, 32(6):1019–1032, 2013.

[57] M Elena Martinez-Perez, Alun D Hughes, Alice V Stanton, Simon A Thom, Neil Chapman, Anil Anthony Bharath, and Kim H Parker. Retinal vascular tree morphology: a semi-automatic quantification. *IEEE transactions on bio-medical engineering*, 49(8):912–917, 2002.

[58] Kai Rothaus, Xiaoyi Jiang, and Paul Rhiem. Separation of the retinal vascular graph in arteries and veins based upon structural knowledge. *Image and Vision Computing*, 27(7):864–875, 2009.

[59] Qiangfeng Peter Lau, Mong Li Lee, Wynne Hsu, and Tien Yin Wong. Simultaneously identifying all true vessels from segmented retinal images. *IEEE transactions on bio-medical engineering*, 60(7):1851–1858, 2013.

[60] Vinayak S Joshi, Joseph M Reinhardt, Mona K Garvin, and Michael D Abramoff. Automated method for identification and artery-venous classification of vessel trees in retinal vessel networks. *PloS one*, 9(2):e88061, 2014.

[61] Enrico Grisan and Alfredo Ruggeri. A divide et impera strategy for automatic classification of retinal vessels into arteries and veins. In *Engineering in Medicine and Biology Society, 2003. Proceedings of the 25th Annual International Conference of the IEEE*, volume 1, pages 890–893. IEEE, 2003.

[62] SG Vázquez, Brais Cancela, Noelia Barreira, Manuel G Penedo, M Rodríguez-Blanco, M Pena Seijo, G Coll de Tuero, Maria Antònia Barceló, and Marc Saez. Improving retinal artery and vein classification by means of a minimal path approach. *Machine vision and applications*, 24(5):919–930, 2013.

[63] Huiqi Li, Wynne Hsu, Mong Li Lee, and Hongyu Wang. A piecewise gaussian model for profiling and differentiating retinal vessels. In *Image Processing, 2003. ICIP 2003. Proceedings. 2003 International Conference on*, volume 1, pages I–1069. IEEE, 2003.

[64] Claudia Kondermann, Daniel Kondermann, and Michelle Yan. Blood vessel classification into arteries and veins in retinal images. In *Medical Imaging*, pages 651247–651247. International Society for Optics and Photonics, 2007.

[65] Meindert Niemeijer, Bram van Ginneken, and Michael D Abràmoff. Automatic classification of retinal vessels into arteries and veins. In *SPIE medical imaging*, pages 72601F–72601F. International Society for Optics and Photonics, 2009.

[66] Meindert Niemeijer, Xiayu Xu, Alina V Dumitrescu, Priya Gupta, Bram van Ginneken, James C Folk, and Michael D Abramoff. Automated measurement of the arteriolar-to-venular width ratio in digital color fundus photographs. *Medical Imaging, IEEE Transactions on*, 30(11):1941–1950, 2011.

[67] Andrea Zamperini, Andrea Giachetti, Emanuele Trucco, and Khai Sing Chin. Effective features for artery-vein classification in digital fundus images. In *Computer-Based Medical Systems (CBMS), 2012 25th International Symposium on*, pages 1–6. IEEE, 2012.

[68] Qazaleh Mirsharif, Farshad Tajeripour, and Hamidreza Pourreza. Automated characterization of blood vessels as arteries and veins in retinal images. *Computerized Medical Imaging and Graphics*, 37(7):607–617, 2013.

[69] Chisako Muramatsu, Yuji Hatanaka, Tatsuhiko Iwase, Takeshi Hara, and Hiroshi Fujita. Automated selection of major arteries and veins for measurement of arteriolar-to-venular diameter ratio on retinal fundus images. *Computerized Medical Imaging and Graphics*, 35(6):472–480, 2011.

[70] D Relan, T MacGillivray, L Ballerini, and E Trucco. Retinal vessel classification: sorting arteries and veins. In *Engineering in Medicine and Biology Society (EMBC), 2013 35th Annual International Conference of the IEEE*, pages 7396–7399. IEEE, 2013.

[71] D Relan, T MacGillivray, L Ballerini, and E Trucco. Automatic retinal vessel classification using a least square-support vector machine in vampire. In *Engineering in Medicine and Biology Society (EMBC), 2014 36th Annual International Conference of the IEEE*, pages 142–145. IEEE, 2014.

[72] Barbara F Westmoreland, Michael A Lemp, and Richard S Snell. Clinical anatomy of the eye, 1998.

[73] Alfredo Ruggeri, Enrico Grisan, and Massimo De Luca. An automatic system for the estimation of generalized arteriolar narrowing in retinal images. In *Engineering in Medicine and Biology Society, 2007. EMBS 2007. 29th Annual International Conference of the IEEE*, pages 6463–6466. IEEE, 2007.

[74] Lara Tramontan, Enrico Grisan, and Alfredo Ruggeri. An improved system for the automatic estimation of the arteriolar-to-venular diameter ratio (avr) in retinal images. In *Engineering in Medicine and Biology Society, 2008. EMBS 2008. 30th Annual International Conference of the IEEE*, pages 3550–3553. IEEE, 2008.

[75] Michael D Knudtson, Kristine E Lee, Larry D Hubbard, Tien Yin Wong, Ronald Klein, and Barbara EK Klein. Revised formulas for summarizing retinal vessel diameters. *Current eye research*, 27(3):143–149, 2003.

[76] Marcos Ortega, Noelia Barreira, Jorge Novo, Manuel G Penedo, Antonio Pose-Reino, and Francisco Gómez-Ulla. Sirius: A web-based system for retinal image analysis. *International journal of medical informatics*, 79(10):722–732, 2010.

[77] Alexander Karl-Georg Schuster, Joachim Ernst Fischer, and Urs Vossmerbaeumer. Semi-automated retinal vessel analysis in nonmydriatic fundus photography. *Acta ophthalmologica*, 92(1):e42–e49, 2014.

[78] Alauddin Bhuiyan, Chandan Karmakar, Ryo Kawasaki, Ecosse Lamoureux, Kotagiri Ramamohanarao, Yogesan Kanagasingam, and Tien Y Wong. Retinal artery and venular caliber grading: A semi-automated evaluation tool. *Computers in biology and medicine*, 44:1–9, 2014.

[79] W. Hsu Q. P. Lau, M. L. Lee and T. Y. Wong. The singapore eye vessel assessment system. In E. Y. K. Ng, U. Rajendra Acharya, Aurelio Campilho, and Jasjit S. Suri, editors, *Image Analysis and Modeling in Opthalmology*, pages 85–109. CRC Press, 2014.

[80] Kenneth H Fritzsche. *Computer vision algorithms for retinal vessel width change detection and quantification*. PhD thesis, Rensselaer Polytechnic Institute, 2002.

[81] Meindert Niemeijer, Bram van Ginneken, and Michael D Abràmoff. Automatic determination of the artery vein ratio in retinal images. In *SPIE Medical Imaging*, pages 76240I–76240I. International Society for Optics and Photonics, 2010.

[82] Chisako Muramatsu, Yuji Hatanaka, Tatsuhiko Iwase, Takeshi Hara, and Hiroshi Fujita. Automated detection and classification of major retinal vessels for determination of diameter ratio of arteries and veins. In *SPIE Medical Imaging*, pages 76240J–76240J. International Society for Optics and Photonics, 2010.

[83] Xiayu Xu, Meindert Niemeijer, Qi Song, Mona Kathryn Garvin, Joseph M Reinhardt, and Michael D Abràmoff. Retinal vessel width measurements based on a graph-theoretic method. In *Biomedical Imaging: From Nano to Macro, 2011 IEEE International Symposium on*, pages 641–644. IEEE, 2011.

[84] Jie Ding, Carol Y Cheung, M Kamran Ikram, Ying-Feng Zheng, Ching-Yu Cheng, Ecosse L Lamoureux, E Shyong Tai, Tavintharan Subramaniam, and Tien Yin Wong. Early retinal arteriolar changes and peripheral neuropathy in diabetes. *Diabetes care*, 35(5):1098–1104, 2012.

[85] Balvinder Wasan, Alessia Cerutti, Susan Ford, and Ronald Marsh. Vascular network changes in the retina with age and hypertension. *Journal of hypertension*, 13(12):1724–1728, 1995.

[86] Niall Patton, Tariq M Aslam, Thomas MacGillivray, Ian J Deary, Baljean Dhillon, Robert H Eikelboom, Kanagasingam Yogesan, and Ian J Constable. Retinal image analysis: concepts, applications and potential. *Progress in retinal and eye research*, 25(1):99–127, 2006.

[87] William E Hart, Michael Goldbaum, Brad Côté, Paul Kube, and Mark R Nelson. Measurement and classification of retinal vascular tortuosity. *International journal of medical informatics*, 53(2):239–252, 1999.

[88] C Swanson, KD Cocker, KH Parker, MJ Moseley, and AR Fielder. Semiautomated computer analysis of vessel growth in preterm infants without and with rop. *British journal of ophthalmology*, 87(12):1474–1477, 2003.

[89] J David, Rekha Krishnan, et al. Neural network based retinal image analysis. In *Image and Signal Processing, 2008. CISP'08. Congress on*, volume 2, pages 49–53. IEEE, 2008.

[90] Harihar Narasimha-Iyer, Ali Can, Badrinath Roysam, Howard L Tanenbaum, and Anna Majerovics. Integrated analysis of vascular and nonvascular changes from color retinal fundus image sequences. *Biomedical Engineering, IEEE Transactions on*, 54(8):1436–1445, 2007.

[91] Arpenik Avakian, Robert E Kalina, E Helene Sage, Avni H Rambhia, Katherine E Elliott, Elaine L Chuang, John I Clark, Jenq-Neng Hwang, and Patricia Parsons-Wingerter. Fractal analysis of region-based vascular change in the normal and non-proliferative diabetic retina. *Current eye research*, 24(4):274–280, 2002.

[92] Tatijana Stosic and Borko D Stosic. Multifractal analysis of human retinal vessels. *Medical Imaging, IEEE Transactions on*, 25(8):1101–1107, 2006.

[93] Michael D Abràmoff, Mona K Garvin, and Milan Sonka. Retinal imaging and image analysis. *Biomedical Engineering, IEEE Reviews in*, 3:169–208, 2010.

[94] Chanjira Sinthanayothin, James F Boyce, Helen L Cook, and Thomas H Williamson. Automated localisation of the optic disc, fovea, and retinal blood vessels from digital colour fundus images. *British Journal of Ophthalmology*, 83(8):902–910, 1999.

[95] David J Couper, Ronald Klein, Larry D Hubbard, Tien Yin Wong, Paul D Sorlie, Lawton S Cooper, Rosemary J Brothers, and F Javier Nieto. Reliability of retinal photography in the assessment of retinal microvascular characteristics: the atherosclerosis risk in communities study. *American journal of ophthalmology*, 133(1):78–88, 2002.

[96] Carlos S Pereira, Hugo Fernandes, Ana Maria Mendonça, and Aurélio Campilho. Detection of lung nodule candidates in chest radiographs. In *Pattern Recognition and Image Analysis*, pages 170–177. Springer, 2007.

[97] Carlos S Pereira, Ana Maria Mendonça, and Aurélio Campilho. Evaluation of contrast enhancement filters for lung nodule detection. In *Image Analysis and Recognition*, pages 878–888. Springer, 2007.

[98] Hidefumi Kobatake. A convergence index filter for vector fields and its application to medical image processing. *Electronics and Communications in Japan (Part III: Fundamental Electronic Science)*, 89(6):34–46, 2006.

[99] Hidefumi Kobatake and Shigeru Hashimoto. Convergence index filter for vector fields. *Image Processing, IEEE Transactions on*, 8(8):1029–1038, 1999.

[100] Hidefumi Kobatake and Masayuki Murakami. Adaptive filter to detect rounded convex regions: Iris filter. In *Pattern Recognition, 1996., Proceedings of the 13th International Conference on*, volume 2, pages 340–344. IEEE, 1996.

[101] Jun Wei, Yoshihiro Hagihara, and Hidefumi Kobatake. Detection of cancerous tumors on chest x-ray images-candidate detection filter and its evaluation. In *Image Processing, 1999. ICIP 99. Proceedings. 1999 International Conference on*, volume 3, pages 397–401. IEEE, 1999.

[102] Pedro Quelhas, Monica Marcuzzo, Ana Maria Mendonça, and Aurélio Campilho. Cell nuclei and cytoplasm joint segmentation using the sliding band filter. *Medical Imaging, IEEE Transactions on*, 29(8):1463–1473, 2010.

[103] Ana Maria Mendonça, António Sousa, Luís Mendonça, and Aurélio Campilho. Automatic localization of the optic disc by combining vascular and intensity information. *Computerized Medical Imaging and Graphics*, 37(5):409–417, 2013.

[104] William S Cleveland. Robust locally weighted regression and smoothing scatterplots. *Journal of the American statistical association*, 74(368):829–836, 1979.

[105] Expert system for early automated detection of dr by analysis of digital retinal images project website. http://www.uhu.es/retinopathy/muestras2.php, 2012.

[106] Zicheng Guo and Richard W Hall. Parallel thinning with two-subiteration algorithms. *Communications of the ACM*, 32(3):359–373, 1989.

[107] Marco Foracchia, Enrico Grisan, and Alfredo Ruggeri. Luminosity and contrast normalization in retinal images. *Medical Image Analysis*, 9(3):179–190, 2005.

[108] Pavel Pudil, Jana Novovičová, and Josef Kittler. Floating search methods in feature selection. *Pattern recognition letters*, 15(11):1119–1125, 1994.

[109] Theodore Grosvenor and Theodore P Grosvenor. *Primary care optometry*. Elsevier Health Sciences, 2007.

[110] M. Niemeijer, J.J. Staal, B.v. Ginneken, M. Loog, and M.D. Abramoff. DRIVE: Digital retinal Images for Vessel Extraction. http://www.isi.uu.nl/Research/Databases/DRIVE, 2004.

[111] M. Niemeijer, X. Xu, A. Dumitrescu, P. Gupta, B. van Ginneken, J. Folk, and M. Abramoff. INSPIRE-AVR:Iowa Normative Set for Processing Images of the REtina-Artery Vein Ratio. http://webeye.ophth.uiowa.edu/component/k2/item/270, 2011.

[112] Thanh T Nguyen and Tien Yin Wong. Retinal vascular changes and diabetic retinopathy. *Current diabetes reports*, 9(4):277–283, 2009.

[113] Tien Yin Wong, FM Amirul Islam, Ronald Klein, Barbara EK Klein, Mary Frances Cotch, Cecilia Castro, A Richey Sharrett, and Eyal Shahar. Retinal vascular caliber, cardiovascular risk factors, and inflammation: the multi-ethnic study of atherosclerosis (mesa). *Investigative ophthalmology & visual science*, 47(6):2341–2350, 2006.

[114] Paul Mitchell, Ning Cheung, Kristin de Haseth, Bronwen Taylor, Elena Rochtchina, FM Amirul Islam, Jie Jin Wang, Seang Mei Saw, and Tien Y Wong. Blood pressure and retinal arteriolar narrowing in children. *Hypertension*, 49(5):1156–1162, 2007.

[115] A Richey Sharrett, Larry D Hubbard, Lawton S Cooper, Paul D Sorlie, Rosemary J Brothers, F Javier Nieto, Joan L Pinsky, and Ronald Klein. Retinal arteriolar diameters and elevated blood pressure the atherosclerosis risk in communities study. *American journal of epidemiology*, 150(3):263–270, 1999.

[116] Tien Yin Wong. Is retinal photography useful in the measurement of stroke risk? *The Lancet Neurology*, 3(3):179–183, 2004.

[117] Ning Cheung and Tien Y Wong. The retinal arteriole to venule ratio: informative or deceptive? *Graefe's Archive for Clinical and Experimental Ophthalmology*, 245(8):1245–1246, 2007.

[118] Niall Patton, Rishma Maini, Tom MacGillivary, Tariq M Aslam, Ian J Deary, and Baljean Dhillon. Effect of axial length on retinal vascular network geometry. *American journal of ophthalmology*, 140(4):648–e1, 2005.

[119] MK Ikram, FJ De Jong, MJ Bos, JR Vingerling, A Hofman, PJ Koudstaal, PTVM De Jong, and MMB Breteler. Retinal vessel diameters and risk of stroke the rotterdam study. *Neurology*, 66(9):1339–1343, 2006.

[120] Tien Yin Wong, Ronald Klein, A Richey Sharrett, Maria I Schmidt, James S Pankow, David J Couper, Barbara EK Klein, Larry D Hubbard, Bruce B Duncan, ARIC Investigators, et al. Retinal arteriolar narrowing and risk of diabetes mellitus in middle-aged persons. *Jama*, 287(19):2528–2533, 2002.

[121] Tien Yin Wong, Anoop Shankar, Ronald Klein, Barbara EK Klein, and Larry D Hubbard. Retinal arteriolar narrowing, hypertension, and subsequent risk of diabetes mellitus. *Archives of internal medicine*, 165(9):1060–1065, 2005.

[122] Tien Yin Wong, Bruce B Duncan, Sherita Hill Golden, Ronald Klein, David J Couper, Barbara EK Klein, Larry D Hubbard, A Richey Sharrett, and Maria I Schmidt. Associations between the metabolic syndrome and retinal microvascular signs: the atherosclerosis risk in communities study. *Investigative ophthalmology & visual science*, 45(9):2949–2954, 2004.

[123] Thanh T Nguyen and Tien Y Wong. Retinal vascular manifestations of metabolic disorders. *Trends in Endocrinology & Metabolism*, 17(7):262–268, 2006.

[124] Cong Sun, Jie Jin Wang, David A Mackey, and Tien Y Wong. Retinal vascular caliber: systemic, environmental, and genetic associations. *Survey of ophthalmology*, 54(1):74–95, 2009.

[125] Larry D Hubbard, Rosemary J Brothers, William N King, Limin X Clegg, Ronald Klein, Lawton S Cooper, A Richey Sharrett, Matthew D Davis, and Jianwen Cai. Methods for evaluation of retinal microvascular abnormalities associated with hypertension/sclerosis in the atherosclerosis risk in communities study. *Ophthalmology*, 106(12):2269–2280, 1999.

[126] Huiqi Li, Wynne Hsu, Mong Li Lee, and Tien Yin Wong. Automatic grading of retinal vessel caliber. *Biomedical Engineering, IEEE Transactions on*, 52(7):1352–1355, 2005.

[127] Xaro Benavent, L Martínez-Costa, Guillermo Ayala, Juan Domingo, and P Marco. Semi-automated evaluation tool for retinal vasculopathy. *Computer methods and programs in biomedicine*, 95(3):288–299, 2009.

[128] Antonio Pose-Reino, Francisco Gomez-Ulla, Bashir Hayik, Marta Rodriguez-Fernández, María J Carreira-Nouche, Antonio Mosquera-Gonzalez, Manuel Gonzalez-Penedo, and Francisco Gude. Computerized measurement of retinal blood vessel calibre: description, validation and use to determine the influence of ageing and hypertension. *Journal of hypertension*, 23(4):843–850, 2005.

[129] JC Parr and GF Spears. General caliber of the retinal arteries expressed as the equivalent width of the central retinal artery. *Am J Ophthalmol*, 77(4):472–477, 1974.

[130] JC Parr and GF Spears. Mathematic relationships between the width of a retinal artery and the widths of its branches. *American journal of ophthalmology*, 77(4):478–483, 1974.

[131] Ronald Klein, A Richey Sharrett, Bruce B Duncan, David J Couper, Larry D Hubbard, F Javier Nieto, Tien Yin Wong, and Barbara EK Klein. Retinal arteriolar diameter and risk for hypertension. *Annals of Internal Medicine*, 140(4), 2004.

[132] Ning Cheung, Kim C Donaghue, Gerald Liew, Sophie L Rogers, Jie Jin Wang, Shueh-Wen Lim, Alicia J Jenkins, Wynne Hsu, Mong Li Lee, and Tien Y Wong. Quantitative assessment of early diabetic retinopathy using fractal analysis. *Diabetes care*, 32(1):106–110, 2009.

[133] Bashir Al-Diri and Andrew Hunter. Automated measurements of retinal bifurcations. In *World Congress on Medical Physics and Biomedical Engineering, September 7-12, 2009, Munich, Germany*, pages 205–208. Springer, 2009.

[134] M Zamir. Optimality principles in arterial branching. *Journal of Theoretical Biology*, 62(1):227–251, 1976.

[135] Tien Yin Wong, Michael D Knudtson, Ronald Klein, Barbara EK Klein, Stacy M Meuer, and Larry D Hubbard. Computer-assisted measurement of retinal vessel diameters in the beaver dam eye study: methodology, correlation between eyes, and effect of refractive errors. *Ophthalmology*, 111(6):1183–1190, 2004.

[136] H Leung, M Hons, J Jin, W Mmed, ER Mapplstat, AGT Hons, TYW Frcs, LDH Mat, RK Mph, and PM Franzco. Clinical and epidemiological computer-assisted retinal vessel measurement in an older population: correlation between right and left eyes. *Clinical and Experimental Ophthalmology*, pages 326–330, 2003.

[137] M. Goldbaum A.D. Hoover, V. Kouznetsova. STARE: STructured Analysis of the Retina. http://www.ces.clemson.edu/~ahoover/stare/, 2000.

[138] VICAVR: VARPA Images for the Computation of the Arterio/Venular Ratio. http://www.varpa.es/vicavr.html, 2010.

[139] MESSIDOR: Methods for Evaluating Segmentation and Indexing techniques Dedicated to Retinal Ophthalmology. http://messidor.crihan.fr/download-en.php, 2004.

[140] ONHSD: optic nerve head segmentation dataset. http://www.aldiri.info/Image Datasets/ONHSD.aspx, 2010.

[141] RetinaCAD: Retinal Computer Diagnosis System. http://paginas.fe.up.pt/~retinacad, 2014.